Simulation, Synthesis, Sunlight

Enhancing Electronic Transport in Solid-State Dye-Sensitized Solar Cells

Varun Sivaram

University of Oxford

A thesis submitted for the degree of

Doctor of Philosophy

December 1, 2013

Declaration

This thesis is the result of my own work and includes nothing which is the outcome of work done in collaboration except where specifically indicated in the text.[1]

I declare that no part of this work has been submitted for a degree or any other qualification at this or any other university.

Varun Sivaram, July 2013

Following is a list of collaborations and acknowledgements by Figure:

- Figures 3.1-3.3: Derivations in collaboration with James Kirkpatrick.
- Figures 5.3-5.5: Device fabrication in collaboration with Golnaz Sadoughi.
- Figure 5.14: ZnO nanowire fabrication and SEM by Jonathan Downing.
- Figure 5.18: Transient perturbation measurement in collaboration with Pablo Docampo.
- Figure 6.1: Figure courtesy of Edward Crossland.
- Figure 6.4-6.5: Device fabrication in collaboration with Nakita Noel.
- Figure 6.11: TMS measurements in collaboration with Tomas Leijtens.
- Figure 6.13: Schematic adapted from Tomas Leijtens with permission.

[1] Note: Throughout this thesis, I employ the first person plural voice when describing results and protocols. I chose this convention because (a) it is aesthetically advantageous, (b) welcomes the reader to engage in discussion sections and mathematical derivation, and (c) acknowledges collaborations when relevant. However, irrespective of my pronoun usage, this thesis represents my own work except where I specifically acknowledge collaboration.

Acknowledgements

I owe speedy completion of this thesis to my advisor, Dr. Henry Snaith, who encouraged me to follow my dreams and gave me the flexibility to study a wide range of phenomena in the dye sensitized solar cell. No ordinary supervisor would put up with my limited attention span or humor my ambitions to apply myself outside of the laboratory. I am truly grateful for his guidance.

I very much appreciate the time and effort that my thesis examiners, Dr. Andrew Watt and Dr. Thomas Anthopoulos, put into my oral examination. While difficult, the *viva* was memorable because I had to think outside the box and outside of my thesis to relate my work to general physical principles and new opportunities.

I also am indebted to the Rhodes Trust for financing my graduate education and introducing me to an international network of exceptional people.

Back at Stanford, I am fortunate to have a mentor in Professor Bruce Clemens. I fell in love with Physics when I took Matsci 195 my sophomore winter quarter, and he has believed in me even more than I believe in myself. The Fourier Series in the Appendix is entirely dedicated to him, and I am thankful that he supervised my research design for Chapters 3 and 4 when I spent time in California.

Finally, I sincerely thank Mayor Antonio R. Villaraigosa of Los Angeles, who invited my counsel on implementing Los Angeles' groundbreaking renewable energy infrastructure and overall energy policy. The Mayor's trust in an untested doctoral student enabled me to situate my work in a broader context and discover a passion for progressive energy policy. It is an honor to have co-authored an article about his legacy.

The work I present includes several fruitful collaborations which I would like to acknowledge. First, Ed Crossland was an early mentor and inspired me with his novel synthesis products; I want to thank him for tirelessly providing me with his patented TiO_2 Mesoporous Single Crystals so I could perform the device fabrication and electronic characterization I present in Chapter 6. James Kirkpatrick was another mentor, taking me under his wing to introduce me to the complex world of device modelling. I am grateful for his tutelage in building the simple

and complex models I present in Chapters 3-5 and helping me perform the requisite simulations. Finally, Jon Downing at Imperial College provided a steady stream of perfectly manicured ZnO nanowires, from which I fabricated devices presented in Chapter 5.

Among my fellow DPhil students, I owe a debt to Golnaz Sadoughi for pushing us hard to the finish on the SnO_2/P3HT devices I present in Chapter 4. Pablo Docampo was the wise electronic process guru, always ready to help me operate and analyze the transients rig. Sam Stranks was a role model for me and talked me out of jumping ship, because he made it look so easy. And I reserve my fondest gratitude for Tomas Leijtens and Nakita Noel, who basically saved me from serious harm in the lab, debunked my scientific theories, and worked with me as a great team on the MSC device and electronic properties investigation in Chapter 6.

To the rest of the lab—thank you for putting up with my shoddy mopping and far-from-California moping.

Here in Oxford, nobody did more for my sanity than Harmeet Grewal, who opened her family's home and her big heart to me and kept the stress at bay. The Chutney and Chips gang got me out of the lab and onto the Bhangra floor, and the Rhodies kept me sharp on politics and football. And back home, Mom, Dad, Uttara, Saya, and all my amazing friends kept reminding me I hadn't been forgotten. Dad was always there to read my latest draft, Mom to remind me how to use a microwave, Saya to be cute, and Uttara to demand help on homework. Some things never change...

For my Father, on whose shoulders I am standing.

Abstract

The solid-state dye sensitized solar cell (SDSC) is an emerging photovoltaic technology which promises inexpensive materials, roll-to-roll processing, and a stable architecture. In this thesis, I seek to enhance electronic transport in order to enable thicker devices and yield higher power conversion efficiencies. I adopt a mulitpronged approach to advance three aims, employing analytical, computational, and experimental methodologies.

First, I generalize existing models of the dye sensitized solar cell (DSSC) to allow simple parameter fitting of real devices and to account for previously ignored electronic processes. In Chapter 3 and Chapter 4 I present a nondimensional model capable of fitting real devices and simulating transient behavior without extensive material knowledge. Subsequently in Chapter 5, I introduce a novel three-dimensional model which incorporates electronic drift.

Second, in Chapter 4 I critically assess a widespread method of measuring the charge collection efficiency, η_c, the summary metric that describes the efficacy of charge transport in the SDSC. I discover that the conventional method is inaccurate for values of η_c below 90% because of large experimental error and an intrinsic inaccuracy in applying a transient method to measure a steady-state parameter.

Third, I aim to increase the rate of charge transport by employing new materials and nanostructures in the place of conventional nanocrystalline TiO_2. In Chapter 5, I present evidence of faster transport and enhanced efficiency in flexible SnO_2 nanowire SDSCs, ZnO nanowire SDSCs, and the first viable SnO_2/P3HT SDSC, where photoanode and hole transporter have been replaced with higher mobility materials. Finally, in Chapter 6, I investigate use of TiO_2 mesoporous single crystals (MSCs) with high surface area and extended crystallinity. After demonstrating the viability of MSCs in SDSCs, I examine enhanced transport caused by the background doping effect of thermal treatment. Together, the progress achieved toward diverse and ambitious goals advances the field and delineates routes to future progress for SDSC development.

Contents

List of Figures

Nomenclature

α	Absorption Coefficient
$\bar{n_0}$	Background Free Charge Density
$\bar{n_1}$	Perturbation Marginal Free Charge Density
$\bar{n}$	Nondimensional free electron density (Bar notation denotes nondimensionalization)
β	Trap State Exponential Distribution Factor
ϵ	Electrical Permittivity
η	Power Conversion Efficiency
η_C	Collection Efficiency
η_{approx}	Collection Efficiency measured using conventional transient perturbation technique
κ_J	Transient Short Circuit Current Decay Constant
κ_V	Transient Short Circuit Voltage Decay Constant
λ	Nondimensional Effective Diffusion Length
$\langle \bar{n} \rangle$	Average Nondimensional Free Electron Density
ν	Nondimensional charge density at $x = 0$
Φ	Illumination Intensity

ψ Electric Potential

τ_0 Free Electron Lifetime

τ_n Effective Electron Lifetime

τ_{trans} Electron Transport Lifetime

b Recombination Exponent

C Capacitance

D or D_0 Free Electron Diffusion Coefficient

D_n Effective Diffusion Coefficient

E_f Fermi Level

G Electron-hole Pair Generation Rate

J_n Electron Current

J_p Hole Current

k Boltzmann's Constant

L Solar Cell Thickness

L_n Electron Diffusion Length

m Diode Ideality Constant

n Free electron Density

N_0 Dark Equilibrium Conduction Band Electron Density

n_l Trapped Electron Density

N_{l0} Dark Equilibrium Trapped Electron Density

p Hole Density

q Electronic Charge

V Voltage

x_α Absorption Length

DSSC Dye-Sensitized Solar Cell

FF Fill Factor

FTO Fluorine-doped Tin Oxide

GW Gigawatt

HOMO Highest Occupied Molecular Orbital

J_{SC} Short-Circuit Current

JV Current-Voltage (Curve/Characteristic)

Li-TFSI Lithium bis(trifluoromethylsulfonyl)imide

LUMO Lowest Unoccupied Molecular Orbital

MSC Mesoporous Single Crystal

MW Megawatt

P3HT Poly(3-hexylthiophene)

PV Photovoltaic

SDSC Solid-State Dye-Sensitized Solar Cell

SEM Scanning Electron Microscope

SPD Spray Pyrolysis Deposition

Spiro 2,2',7,7'-tetrakis(N,N-di-p-methoxyphenyl-amine)9,9'-spirobifluorene

tBP 4-tert-butyl pyridine

TMS Transient Mobility Spectroscopy

V_{OC} Open-Circuit Voltage

V_{SC} Voltage at Short Circuit (meaningful for transient perturbation)

Chapter 1

Introduction

1.1 Background

A global transition to renewable electricity generation is one of the most important and difficult goals of the 21st century. Continued reliance on fossil fuel based generation threatens catastrophic environmental change through anthropogenic global warming. While an international scientific consensus exists regarding the causes and potential repercussions of global warming, government policy responses have been collectively incommensurate with the severity of the problem. Nevertheless, technological innovation in academic and industrial settings holds promise for supplying economically viable renewable electricity alternatives.

An aerial view of global consumption statistics reveals the enormity of the challenge ahead. In 2010 (the most recent year for which the US Energy Information Administration has published global energy data), the world consumed 20.2 trillion kilowatt-hours of electricity, only 4.2 of which came from renewable sources.[1] That figure is dominated by hydropower, which contributed 80% of renewable generation but has limited prospects for replacing the bulk of generation. Climate scientists forecast that to keep CO_2 levels below 500ppm, a threshold concentration above which serious economic and environmental damage would result, renewable energy generation from sources other than biomass and hydroelectricity must increase by multiple orders of magnitude. Thus, although industries like wind and solar power are growing at a healthy clip by normal economic standards,

their respective shares of total electricity generation— $< 3\%$ and $< 1\%$ —require even faster growth rates to compete with fossil fuels.[2]

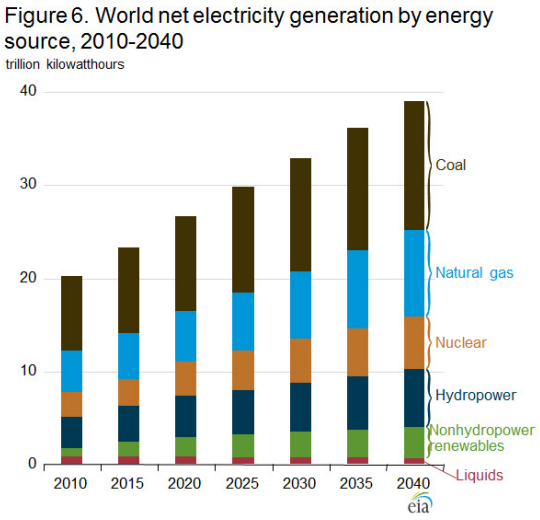

Figure 1.1: Projections of global electricity generation, reprinted from [1]. Note that under this baseline projection, renewable energy adoption does not increase substantially in relation to fossil fuels.

Unfortunately, a global treaty altering market forces to facilitate this adoption has proven elusive. The United Nations Framework Convention on Climate Change arose in 1992 at a conference in Rio de Janeiro and set up future meetings where limits on greenhouse gas emissions would be imposed.[3] The only emissions treaty resulting from Rio was the 1997 Kyoto Protocol, which the United States notably did not ratify; as a result of US nonratification, minimal restrictions on Eastern European nations, and no binding limits for developing countries, Kyoto did not effectively rein in emissions. Subsequent conferences, notably Copenhagen in 2009, disappointed environmentalists, and geopolitical disagreements over who should shoulder the economic burdens of the energy transition continue to obstruct progress.[4] Advocates of a global treaty recognize that the free market does not reflect the true environmental and economic costs of carbon emissions and therefore support some combination of emission taxes, a cap-and-trade system, wealth and technology transfer to developing countries, and increased support for technological research. While a cap-and-trade system is operational in Europe, its extension globally is uncertain; it is against this bleak backdrop that scientific

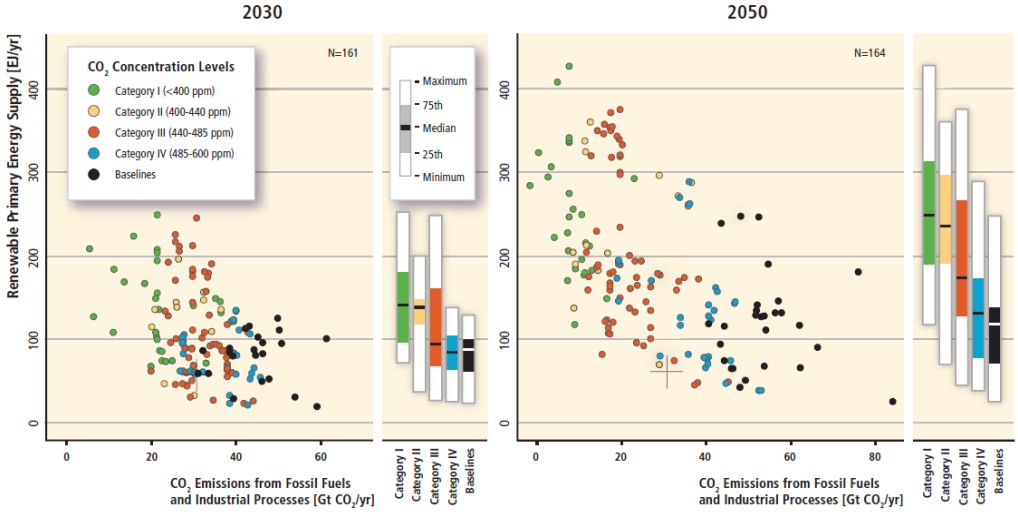

Figure 1.2: Climate change mitigation scenarios performed by the Intergovernmental Panel on Climate Change (reprinted from [2]) in 2030 and 2050 displaying the effects of renewable energy adoption and fossil fuel combustion on CO_2 levels in the atmosphere. The boxplots summarize the scatterplots, demonstrating the requisite levels of renewable energy adoption to control CO_2 emissions.

researchers aim to harness market forces by introducing innovative technologies at compelling price points.

1.2 Introduction to Solar Energy

1.2.1 History and Background

The modern era of photovoltaic (PV) solar energy began in the 1950's when Bell Labs reported 6% efficient solar cells made out of silicon. Within ten years, solar panels adorned an orbiting NASA satellite, and within twenty years governments around the world, including those in the United States and Japan, had thrown significant support and resources behind solar energy innovation. [5]

Yet after the groundswell of support for renewable energy following the energy crisis of the late 1970's, the solar industry largely stagnated for the following two decades, as the industry struggled to scale up next generation thin film technologies and government and public interest waned. Solar's second wind (no

pun intended) and its emergence as a mature commercial industry came at the turn of the 21st century, characterized by a tremendous increase in manufacturing supply, a precipitous decline in solar panel cost, and a relentless migration of manufacturing to China from the US, Europe, and Japan. Since 2000, annual solar production capacity worldwide has increased by well over two orders of magnitude to more than 60GW peak, and the price per peak watt of a solar panel has declined to below a dollar.[6] While these figures appear promising for eventual mainstream adoption of solar, the unstable cocktail of government incentives, undifferentiated products, and reckless production may presage difficulty for maintained producer growth. In early 2013, China-based Suntech, once the largest PV manufacturer in the world, went into bankruptcy, casting further uncertainty on the solar manfacturing industry.

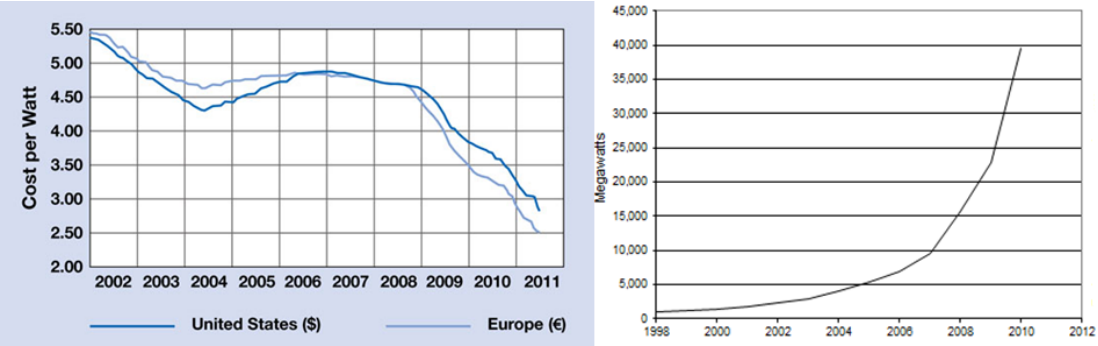

Figure 1.3: (Left): Solar Module Average Selling Price in Europe and USA from 2002-2011 (reprinted from [6]); (Right): Installed Solar PV Capacity from 1998-2010 (Source: Earth Policy Institute).

Solar power is the only renewable electricity source capable of adoption on the scale necessary to overhaul our current generation infrastructure. Although it suffers from a low specific power density (and therefore requires large areas to generate equivalent energy to conventional sources), solar panels occupying less than 1% of (otherwise uninhabited) land in the Sahara desert could power all of Europe[7]. The table below illustrates the unique potential of the solar resource, which dwarfs its renewable competitors in terms of technical potential, which takes into account capacity factor, conversion efficiency, available land, etc.

Resource	Current use	Technical potential	Theoretical potential
Hydropower	9	50	147
Biomass energy	50	>276	2900
Solar energy	0.1	>1575	3900000
Wind energy	0.12	640	6000

Units: exajoule per year

Figure 1.4: 1998 statistics for current energy use and resource potential. For reference, global primary energy demand in 2008 was 474 exajoules.[8]

1.2.2 Physics of Solar Cells

A conventional solar photovoltaic cell is a carefully designed diode which absorbs sunlight, transfers the energy to charge carriers, and preferentially conducts current in a single direction so the carriers can perform useful electrical work (more detailed treatments of solar cell physics can be found in [9; 10]). A sample schematic of a simple Silicon solar cell is shown in Figure 1.5; because silicon dominates the market, we will base our introduction to device physics on silicon solar cells, noting that only minor adjustments are necessary to explain the operation of most commercially available photovoltaic cells. The cell architecture is based on a simple pn junction comprised of a thick p-type layer, the base, where absorption primarily occurs, and a thin n-type layer, the emitter. A grid of metal (most commonly screen-printed silver) fingers acts as the top electrode, only shading a small fraction of the cell area from the sun.

Solar cells are designed to harness a high percentage of photons in the solar spectrum with energies above the bandgap of the absorbing semiconductor. The solar spectrum is depicted in Figure 1.6, and the different Air Mass (AM) curves denote levels of incident radiation at different levels of the atmosphere. The AM0 spectrum refers to the spectral distribution of solar radiation, and the AM1.5 spectrum characterizes the radiation reaching the surface of the Earth after passing through the atmosphere. Silicon, with a bandgap of 1.1eV, can

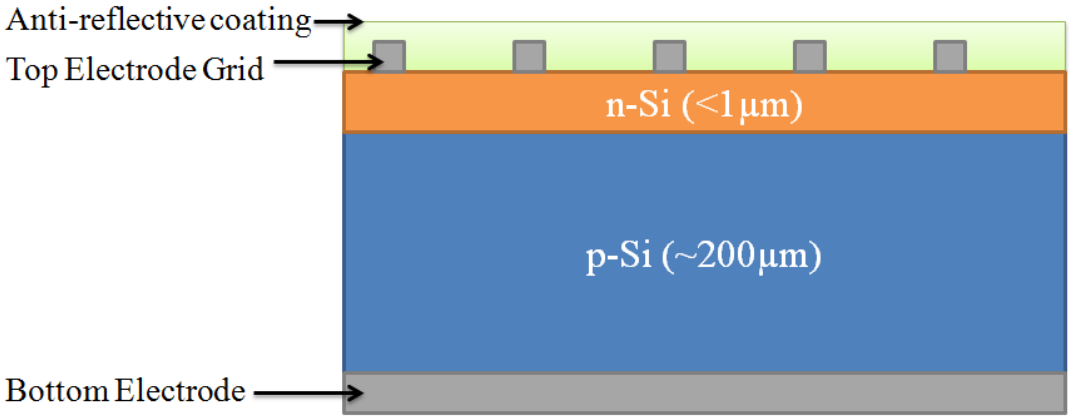

Figure 1.5: Schematic of a simple Silicon solar cell based on a pn junction.

absorb the section of the spectrum shaded in blue in Figure 1.6.[11]

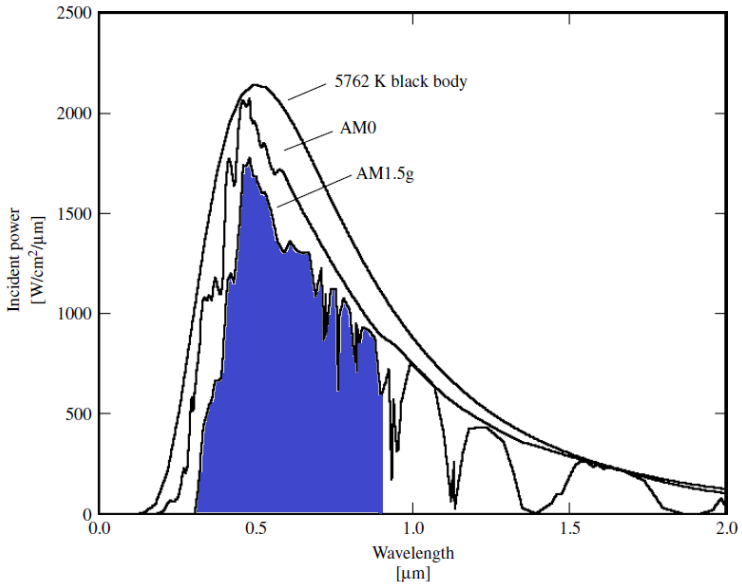

Figure 1.6: Solar spectrum in space (AM0) and at the Earth's surface (AM1.5g, comprising direct and diffuse radiation). Idealized blackbody spectrum included for comparison. AM1.5g spectrum shaded to illustrate Silicon absorption onset.

Solar energy conversion starts with the creation of electron-hole pairs through absorption of photons and electronic transitions from the valence to the conduction band. Conservation of momentum and negligible photon momentum jointly

stipulate that a purely optical transition (for most photon energies) will only occur if the band extrema coincide in momentum; materials for which this is possible, e.g., Gallium Arsenide, possess direct band gaps. Comparatively, materials with offset band extrema, indirect band gap materials (e.g., Silicon), exhibit lower absorption coefficients. Figure 1.7 displays simplified diagrams of photon absorption processes in both kinds of materials.

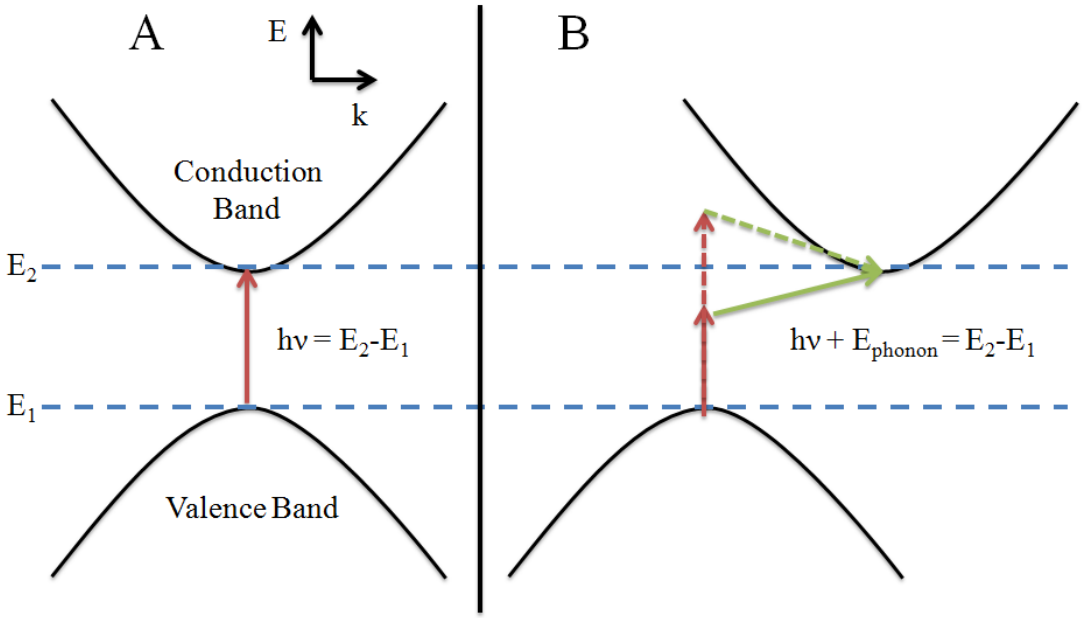

Figure 1.7: (a)Optically induced electronic transition in direct band gap material (e.g., GaAs); (b) Two possible transitions in indirect band gap material (e.g., Si) requiring either emission or absorption of a phonon for momentum conservation. Rationale for lower absorption coefficient of indirect band gap materials.

Upon generation of an electron-hole pair, a conventional solar cell relies upon minority carrier diffusion in a pn junction architecture to achieve preferential current flow. The pn junction energy and carrier flows are diagrammed in Figure 1.8. Briefly, the junction between differently doped layers results in a depletion, or space-charge, region around the junction where an electric field points from the n to the p side. A solar cell operates as a diode in reverse, whereby generated minority carriers diffuse to the junction and are swept through to the other side by the junction built-in electric field. The Fermi-level offset between p and n

sides corresponds to the voltage of extracted carriers (assuming ohmic contacts).

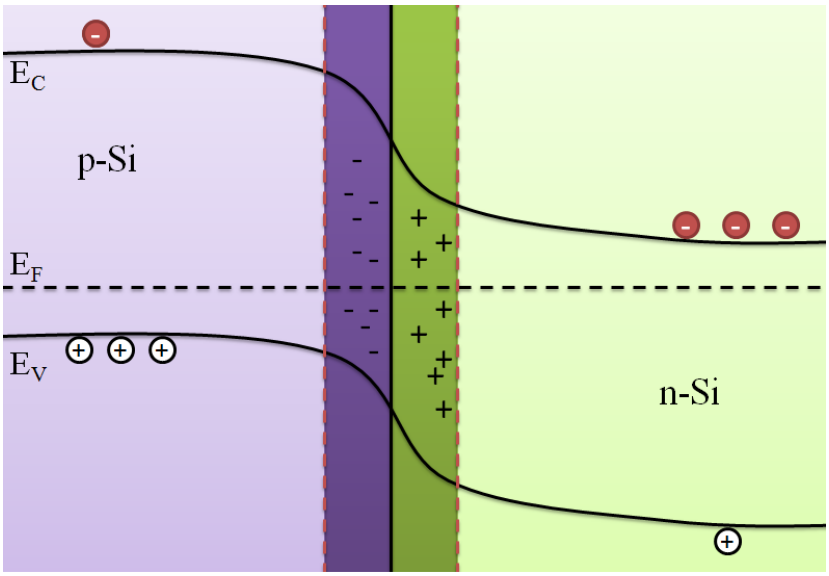

Figure 1.8: Energy diagram for a pn junction illustrating depletion/space-charge region (dark colors) and quasi-neutral regions (light colors). Minority carrier diffusion in the quasi-neutral regions causes the photocurrent

Charge transport proceeds largely by diffusion in the quasi-neutral regions flanking the depletion region. However, for completeness we include the full drift-diffusion version of the semiconductor device equations. First, Poisson's equation relates the Laplacian of electric potential to charge density:

$$-\nabla \cdot (\epsilon \nabla \psi) = q(p - n + N) \tag{1.1}$$

where N denotes the net charge from doping, n and p are electron and hole densities, ϵ is the permittivity, and ψ is the electric potential. The electron and hole continuity equations are:

$$-\nabla \cdot \mathbf{J_n} = \left(G - R_n - \frac{\partial n}{\partial t}\right) \tag{1.2}$$

$$-\nabla \cdot \mathbf{J_p} = \left(G - R_p - \frac{\partial p}{\partial t}\right) \tag{1.3}$$

where G is the generation rate of electron-hole pairs, and R_n and R_p are recombination rates for electrons and holes, respectively.

Minority carrier transport competes with recombination processes, which involve an electron or hole recombining with its counterpart in one of three ways: radiative, Auger, or trap-mediated recombination. All three processes contribute to so-called dark current, or current in the conventionally permitted direction of the diode. Moreover, recombination can occur either in the bulk or at a surface or interface, and the volume to surface area ratio of the semiconductor determines which process dominates.

Figure 1.9 outlines a basic circuit diagram for a solar cell. The key elements are a current source in parallel with a diode, corresponding to the light and dark currents, and a series and shunt resistance corresponding to parasitic cell losses. The series resistance should be minimized and arises, e.g., from contact resistance with the electrodes or from lateral transport in the semiconductor to reach one of the top electrode fingers. The shunt resistance, conversely, refers to shorting pathways like pinholes in the cell and should be maximized.

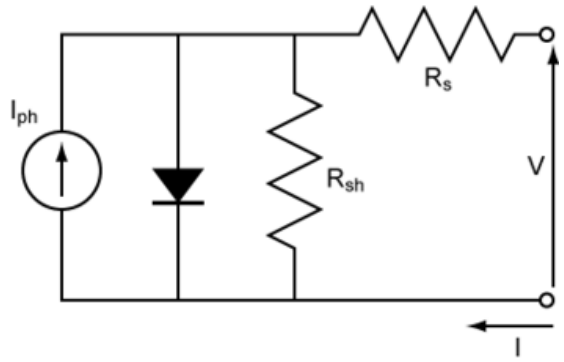

Figure 1.9: Equivalent circuit for a solar cell. I_{PH} refers to photocurrent, R_s signifies series resistance, R_{SH} means shunt resistance, and V corresponds to cell potential.

Circuit analysis is useful in conjunction with certain summary performance metrics to determine the power conversion efficiency of the solar cell and diagnose areas of improvement. There are three ubiquitous summary metrics in the photovoltaic literature: short-circuit current (J_{SC}), open-circuit voltage (V_{OC}), and fill factor (FF). These three can be deduced from a current-voltage (JV) characteristic curve, much like the one in Figure 3.3.

The J_{SC}, the maximum attainable photocurrent density, is achieved when

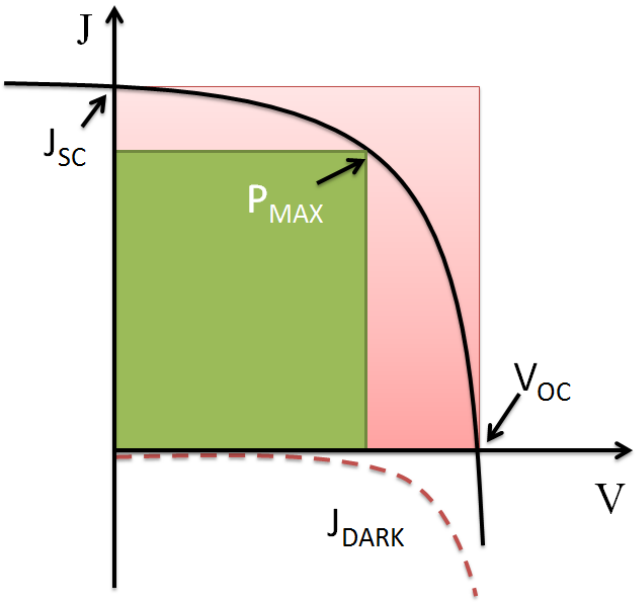

Figure 1.10: Shape of JV Characteristic for a Solar Cell. J_{SC} and V_{OC} are the intercepts of the curve, and the FF is the ratio of the areas of the green and red rectangles, respectively.

the Fermi levels of the p and n layers align and carrier voltage is zero. This metric basically reflects how well the semiconductor absorbs light and how long the minority carrier diffusion length is compared to the device thickness. The V_{OC}, the voltage attained when the dark current cancels out the photocurrent, is influenced by recombination, which we saw earlier contributes to the dark current. Quantitatively, the V_{OC} can be expressed as:

$$V_{OC} \approx \frac{kT}{q} ln \left(\frac{J_{sc}}{J_0} \right) \tag{1.4}$$

where J_0 refers to the diode saturation current density. This reflects the inverse dependence of the V_{OC} on the dark current, a function of the recombination rate of generated minority carriers.

The maximum power generated by a solar cell is the maximum product of current and voltage on the JV curve. The power conversion efficiency is deduced by dividing the photovoltaic power by the incident light intensity, commonly quoted as $1000 W/m^2$. Finally, the FF is merely:

$$FF = \frac{I_{max}V_{max}}{I_{SC}V_{OC}} \tag{1.5}$$

The higher the FF, the closer the JV curve is to a rectangle which intercepts the axes at right angles. The series and shunt resistances are reflected in the fill factor; a high series resistance causes the JV curve to slope away from vertical near open circuit, and a low shunt resistance causes a slope away from horizontal near short circuit.

1.2.3 Comparison of Current Technologies

Currently, polycrystalline silicon solar cells are far and away the technology with the most market share. Postulated reasons for this are diverse, but many believe that (a) familiarity with silicon processing and existing supply chains in the semiconductor industry advanced silicon for photovoltaic applications, (b) the price of polysilicon feedstock dropped nearly two orders of magnitude, and (c) the well-known process flow coupled with government incentives have spurred Chinese factories to increase capacity rapidly. Figure 1.11 displays the market share of each major technology, and we now briefly introduce them.

- Crystalline silicon: this dominant market segment is divided between devices based on pure monocrystalline silicon and (more commonly) polycrystalline silicon, with solar panel, or module, efficiencies of 15-20%. The process flow includes high temperature (900 °C) and vacuum steps for layer deposition.

- Amorphous silicon: this less pure phase of silicon can be grown by chemical vapor deposition instead of the costly ingot/wafer processing of crystalline silicon. Module efficiencies are correspondingly lower at 8-10%.

- CIGS (Copper Indium Gallium Selenium): This semiconductor has a high extinction coefficient and is therefore deposited as a thin film. Module efficiencies are around 10-13% and several start-ups in Silicon Valley once promised to manufacture CIGS with roll-to-roll processing. Many of these firms (e.g., Nanosolar and MiaSole) have been recently bought by Chinese firms at discount prices.

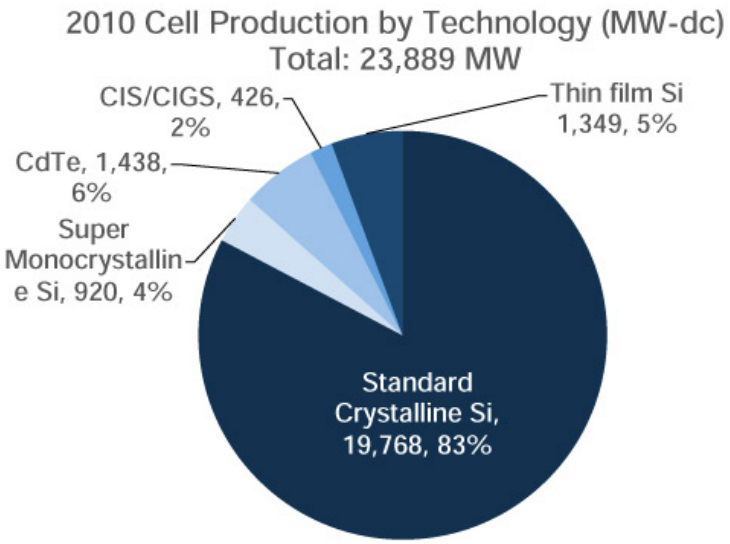

Figure 1.11: 2010 relative market share and absolute production quantities for various solar cell technologies.[12]

- CdTe (Cadmium Telluride): These panels dominate thin film production and one company basically monopolizes its manufacture: First Solar, whose panels currently rate about 13% efficient. Until 2010, First Solar enjoyed significant cost advantages over its silicon competitors but silicon wafer prices have now dropped dramatically.[13]

While silicon enjoys a dominant perch in the solar market and is unlikely to be dislodged by thin film challengers as long as the price of incoming raw materials stays low, it is not inherently the best material for manufacturing solar cells. Its indirect band gap, noted above, coupled with the intensive processing that adds cost, modularizes its fabrication, and limits its form factor, encourage researchers to devise an alternative. Figure 1.12 plots the progress of record lab cell efficiencies for various technologies, and the striking trend is the rapid rise of Emerging PV efficiencies. One of those technologies, the dye sensitized solar cell, holds promise as a silicon alternative because of the prospect of eliminating all intensive processing steps and expensive materials.

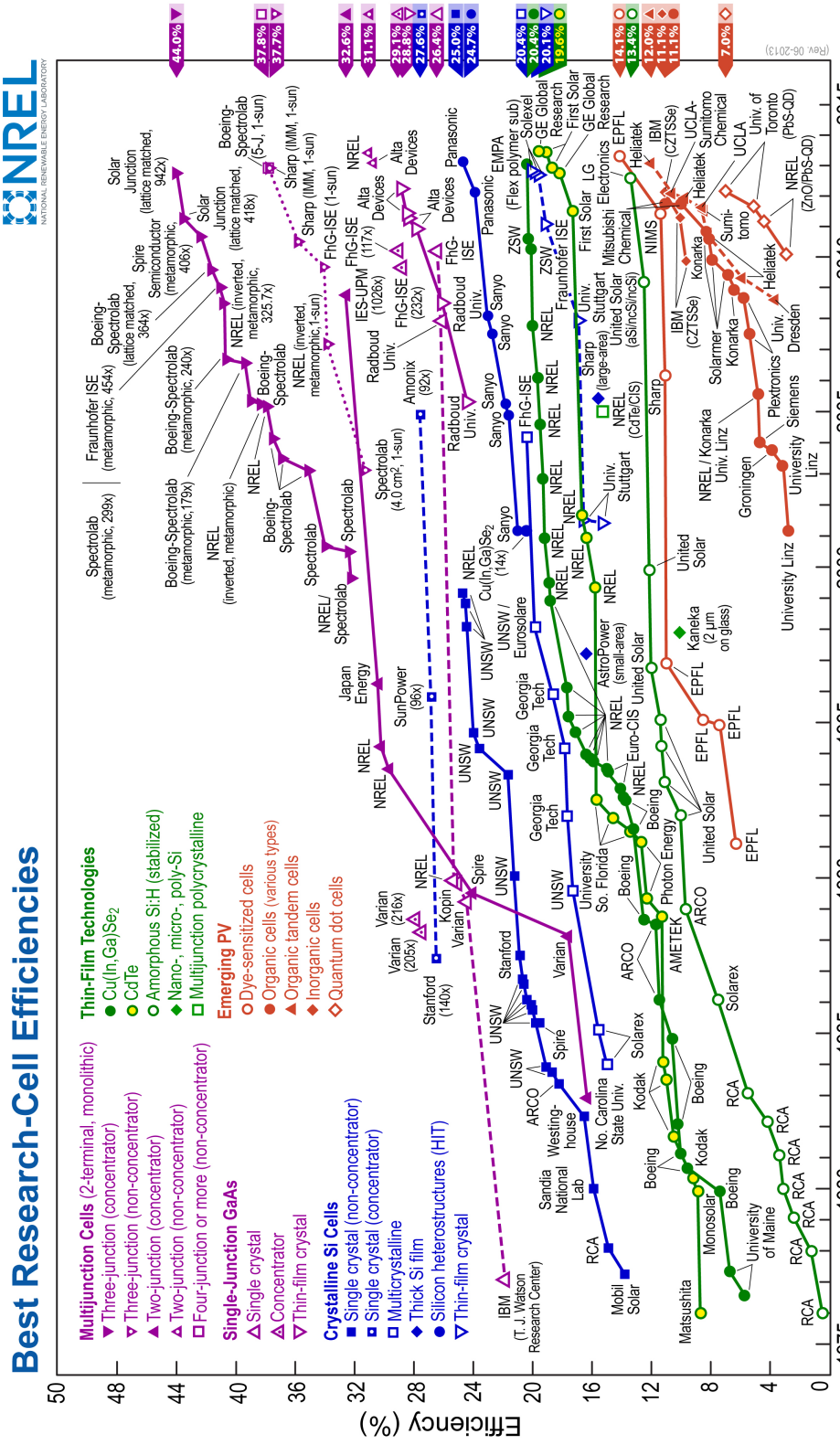

Figure 1.12: Record Efficiencies for various solar technologies as of June, 2013, certified by the US National Renewable Energy Laboratory.[14]

1.3 Solid State Dye Sensitized Solar Cells

1.3.1 Background

The Dye Sensitized Solar Cell (DSSC) was invented by O'Regan and Gratzel in 1991 and holds the potential for achieving high efficiencies at low material and fabrication cost.[15] The device architecture decouples light absorption and charge transport, thereby allowing independent optimization of each process, in contrast to conventional inorganic semiconductor devices.

The DSSC architecture hardly resembles that of the conventional silicon solar cell described above. However, the JV characteristic in Figure 3.3 applies equally well to the output profile of a DSSC. There is considerable debate over whether, functionally, the DSSC operates like a conventional diode cell despite the structural dissimilarities; we will present arguments for equivalence as well as unique elements of DSSC operation which require novel research methods for optimization.

A schematic of the DSSC is provided in Figure 1.13. The device is comprised of a mesoporous network of semiconducting nanoparticles sensitized with a high extinction coefficient dye and infiltrated with an electrolytic or organic hole transporter. Most DSSCs employ a metal oxide, most commonly titania, as the semiconductor responsible for electron transport, but there has been a bifurcation in the infiltrating medium used for hole transport between the use of liquid and solid state materials. The original incarnation of the DSSC employed a liquid electrolyte redox couple composed of iodine and triiodide, and recent systems using a cobalt complex have achieved record efficiencies in excess of 12%.[16] However, any liquid phase component presents reliability concerns, and indeed corrosion and leakage have plagued efforts to fabricate stable, durable liquid DSSCs.

In 1998, Bach et al. employed an organic molecular solid-state hole transporter, 2,2',7,7'-tetrakis(N,N-di-p-methoxyphenyl-amine)9,9'-spirobifluorene (Spiro-OMeTAD or Spiro), the use of which has persisted in the most successful solid state devices.[17] The efficiencies of solid-state dye sensitized solar cells (SDSCs) have recently surpassed 10%, eroding the rationale for pursuing liquid electrolyte

devices.[18] An area of research crucial to improving SDSCs further is reëngineering the devices to permit a greater thickness of nanostructured semiconductor; currently, limitations on the device thickness because of hole transporter infiltration and fast charge recombination hamper the adsorbed dye's ability to effectively harvest incoming solar radiation.

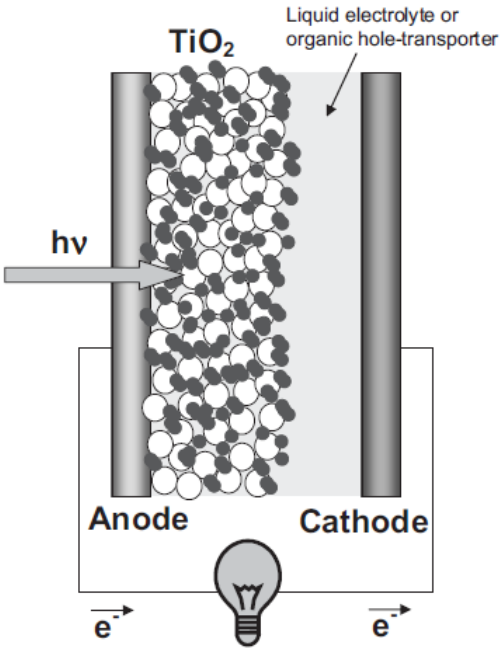

Figure 1.13: DSSC Schematic, where white circles are TiO_2 nanoparticles and dark grey dots are adsorbed dye molecules. Reprinted with permission. [19]

1.3.2 General SDSC Operation

An energy diagram is presented in Figure 1.14 which outlines the main electronic processes in the SDSC. First, photons are absorbed by the dye molecules adsorbed at the surface of the TiO_2, resulting in electronic transitions from the dye's highest occupied molecular orbital (HOMO) to its lowest unoccupied molecular orbital (LUMO).

Process 1 refers to photoinduced charge transfer from dye molecules to the adsorbate, the TiO_2. This involves absorption of a photon by a dye molecule which is excited from its ground (D) state to an excited state (D*) and injects

an electron into the conduction band of the semiconductor. The oxidized dye (D+) is subsequently reduced by the Spiro in Process 2. To encourage charge injection, sensitizers are generally designed with a donor-acceptor π-conjugated system which "pulls" holes from the TiO_2 interface and "pushes" electrons toward anchoring groups.[20] Furthermore, optimizing the energetic favorability of charge injection requires overpotentials of around 0.2-0.3eV both between the TiO_2 conduction band and the dye LUMO and between the dye HOMO and the Spiro oxidation potential. These driving overpotentials achieve more efficient charge injection at the expense of reducing the achievable voltage from the solar cell. The maximum achievable open circuit voltage of the SDSC is defined by the difference in energy between the conduction band of the titania and the oxidation potential of the Spiro. Reducing the necessary overpotentials (which can be as high as 0.75eV) to ensure photoinduced charge transfer and therefore allow the cell to attain a higher voltage remains an active area of research.[21]

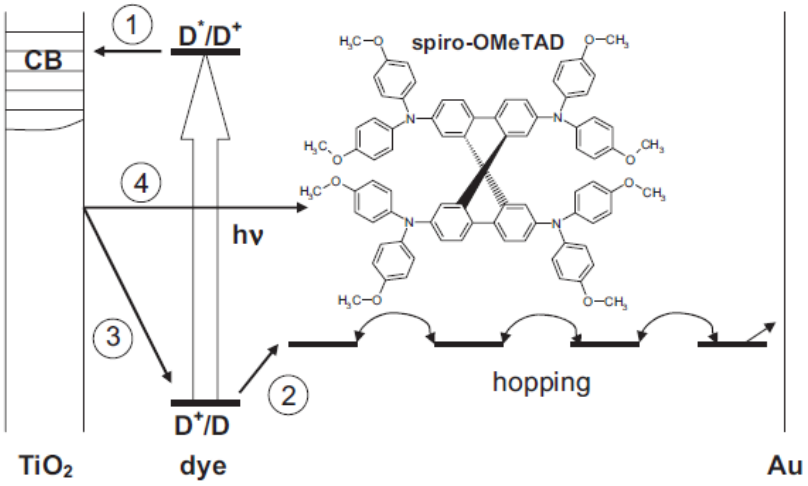

Figure 1.14: Schematic energy diagram for an SDSC illustrating the electronic processes and recombination/loss mechanisms. Process 1: optical excitation of dye molecule and electron injection to semiconductor. Process 2: Hole transfer from oxidized dye molecule to Spiro. Process 3: Electron recombination via back transfer to oxidized dye. Process 4: Electron recombination with hole in Spiro. Reprinted with permission.[19]

It is conjectured that the hole acquired by the oxidized Spiro molecule proceeds to the counterelectrode via diffusive hopping between Spiro molecules. Due

to its low mobility (10^{-4}cm^{2}V^{-1}s^{-1}), Spiro is typically doped with ionic and chemical additives.[19] Although they do improve the mobility of the hole conducting medium, these additives also interact with the surface of the metal oxide semiconductor, affecting charge transfer and recombination in complex ways.[22; 23]

Electrons and holes contribute to photocurrent by diffusing to the anode and cathode, respectively. Loss mechanisms include Processes 3 and 4, where electrons in the semiconductor recombine with holes either on the oxidized dye or Spiro molecules, respectively. In the SDSC, dye regeneration, the process whereby Spiro reduces an oxidized dye molecule, proceeds orders of magnitude faster than in a liquid electrolyte DSSC, thus rendering losses from Process 3 negligible.[24] However, recombination between electrons in TiO_2 and holes in the Spiro occurs much faster in an SDSC because it is a single electron process, compared to the multi-step redox reaction that takes place in a DSSC electrolyte.[25] When the rate of recombination (typically on the order of hundreds of microseconds) approaches the timescale of the rate of carrier extraction, device performance suffers severely.

Most of these processes are amenable to correlation with analogues in the conventional silicon solar cell. In practice, many researchers implicitly adopt the assumptions of the equivalent circuit model introduced earlier in Figure 1.9. The direction of photocurrent arises from asymmetry in the DSSC, in which electrons are preferentially injected toward the anode and holes toward the cathode from the sensitizer. The diode element is harder to identify in the DSSC, but roughly corresponds to the interface between dye and TiO_2—as the applied potential increases, the semiconductor Fermi level rises, favoring reverse current flow from the photocurrent. Series and shunt resistances also play an important role in the SDSC; a high layer thickness of the hole transporter, a high resistivity medium, or incomplete surface coverage of the TiO_2 by Spiro-OMeTAD, leaving exposed shorting pathways, can adversely affect series and shunt resistances, respectively.

However, there is a growing chorus advocating new modeling principles to account for unique elements of the DSSC. A prominent alternative circuit model is presented by Bisquert [26] in Figure 1.15. Dubbed the "transmission line" model, it represents dye excitation as a capacitative process, storing energy in conduction band electrons. Selective contacts from the dye conduction band and

valence band to the anode and cathode, respectively, allow diffusive processes to generate a preferential direction for photocurrent. Back transfer of electrons from the semiconductor to the dye is represented as a charge transfer resistance (though in reality, Bisquert admits this recombination pathway is a composite of parallel non-radiative pathways including direct recombination with the hole transporter). Thus, the transmission line consists of parallel RC circuits connected by selective contacts to each electrode. The advantage of this formulation is to emphasize the capacitative nature of the DSSC; while steady state measurements dominate the characterization arsenal of conventional silicon solar cells, transient measurements are required to probe a DSSC. The present thesis will make extensive use of transient optical perturbation measurements to probe electron transport in the SDSC.

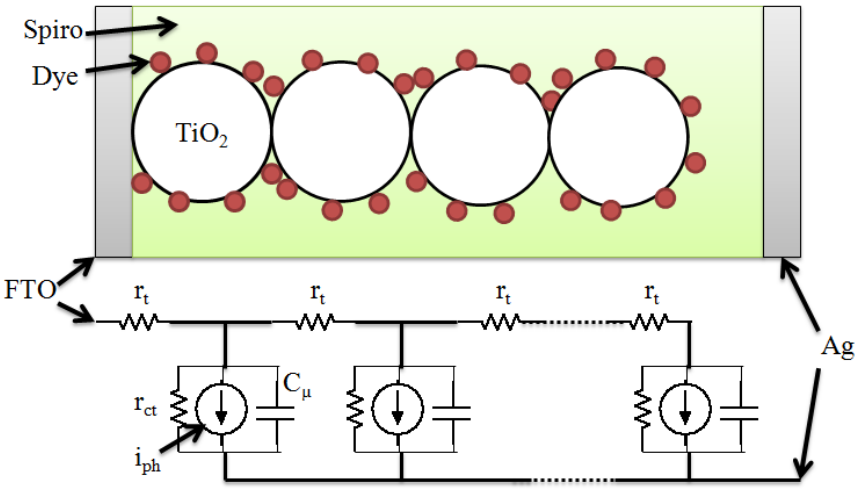

Figure 1.15: Schematic of the transmission line circuit model of the DSSC. Each dye molecule is represented by a current source (i_{ph}) in parallel with a charge transfer resistance (r_{ct}) and a capacitor (C_μ). The current source represents electronic transitions from the dye HOMO to LUMO, each of which is connected selectively to the anode (Fluorine-doped Tin Oxide or FTO) and cathode (Ag), respectively. Series resistance in the TiO_2 is represented by r_t. Adapted from [26].

The power conversion efficiency of a solar cell can be expressed, as above, by the product of J_{SC}, V_{OC}, and FF. In the case of the SDSC, we can also write this efficiency as the product of the efficiencies of the component processes, namely

absorption, injection, and collection (with a final term accounting for energy losses in a non-ideal device, like overpotentials or series resistance):

$$\eta = \eta_{abs} * \eta_{inj} * \eta_{col} * \eta_{energy} \tag{1.6}$$

The third term is that of most interest to us in the present work, so the following section presents a more detailed introduction to the processes by which charges are collected at the electrodes.

1.3.3 Electron Transport

The focus of the present work is improving our understanding of electron transport in the SDSC. The rationale for choosing to focus on improving electron transport instead of hole transport arises from the nature of ambipolar transport in the SDSC. The requirement that charges are extracted at the same rate from the cell implies that transport of the slower charge carrier will have a rate limiting influence on overall charge transport rates. In SDSCs, electronic transport sets the ambipolar diffusion rate, the evidence of which is apparent from constant hole transport rates with changing light intensity.[27]

A prevalently held view in the literature is that, like in a conventional silicon solar cell, charge carriers in the SDSC move primarily by diffusion. Ignoring drift is a very reasonable approximation in the liquid electrolyte based cells because of the high concentration of ions in the electrolyte whose instantaneous reorganization screens any charge imbalance or electric field. Whether this assumption is valid in the SDSC is more controversial, and we will address the question later. However, an extensive modeling literature has been developed around the assumption of drift-only transport, and that is the literature we now introduce.

Diffusive transport in the SDSC can be (and often is) treated very similarly to transport in the conventional silicon solar cell. Neglecting the particulars of the medium, including mobility and defect density, we can generalize an effective diffusion constant, D_n. Similarly, we can remain agnostic to the recombination pathways (recall—radiative, Auger, and trap-mediated in conventional silicon; back transfer to dye and recombination with Spiro for the SDSC) and simply define a characteristic recombination lifetime for electrons, τ_n. This leads to the

classic definition of diffusion length, L_n:

$$L_n = \sqrt{D_n \tau_n} \tag{1.7}$$

Assuming that electron transport and recombination are two processes that compete in parallel, we can write for the collection efficiency, η_c:

$$\eta_c = \frac{\tau_n}{\tau_n + \tau_{trans}} \tag{1.8}$$

where τ_{trans} is a characteristic transport time. Finally, the following empirical result has been observed for the diffusion constant:[28]

$$D_n = \frac{L^2}{2.47 \tau_{trans}} \tag{1.9}$$

where L is the film thickness.

These generic semiconductor equations are useful as a first pass for quantifying the goals of improving SDSCs. By achieving a diffusion length that is over twice the film thickness, we are likely to fabricate a device with over 90% collection efficiency.[29] However, this simplistic formulation ignores much of the complexity in the SDSC which is unique among semiconductor solar cells. For example, the diffusion constant in mesoporous titania, unlike in crystalline silicon, is not constant, but rather dependent on charge density. In fact, some authors do away with the concept of a steady state diffusion length for SDSCs because the charge density dependence makes L_n a local property, not a material property. Instead, they argue, only under controlled conditions of low, uniform charge generation can a "small-perturbation diffusion length" sensibly exist.[30] Here again we observe the necessity of adopting small perturbation, time resolved methods to probe the SDSC because steady-state measurements do not provide the right information. In later chapters we will adopt a more rigorous modeling approach to derive more useful parameters and also observe the source of approximations like Equation 1.9 and when they might lead us astray.

Nanocrystalline TiO_2 is known to be electronically defective, with a population of available electronic states located below the conduction band in the traditionally forbidden band gap. The defects can be located either in the bulk

or at the surface of TiO_2 nanoparticles, though several authors assert that surface traps are predominant.[31] Most authors therefore consider electron transport in the SDSC to proceed via multiple trapping diffusion, where the diffusion of conduction band electrons is punctuated by stationary periods of confinement in localized trap sites. If an electron reaches the collecting electrode prior to a recombination event, it contributes to the photocurrent.

This intuitive microscopic interpretation has been modeled by a continuous time random walk (CTRW) subject to a distribution of waiting times. The waiting time length corresponds to the energetic depth of a trap site.[32] More recently, researchers have tended to approach the problem from a macroscopic point of view, solving current continuity equations for the macroscopic time-dependent density of electrons and stipulating a distribution of trap energy sites. The equivalence of the two approaches has been questioned, since the microscopic CTRW model fails to distinguish between free and trapped electrons; hence, we will adopt the macroscopic approach to model charge density instead of generalizing microscopic constituent processes.[33]

The full macroscopic model was best encapsulated by Bisquert and Vikhrenko, who employed a quasi-equilibrium approximation to account for multiple trapping while retaining the general form of a continuity equation for conduction band electrons.[34] Their efforts successfully related the effective diffusion constant, which characterizes the composite diffusion and trapping of electrons, to the free electron diffusion coefficient, an intrinsic bulk material property. By stipulating an exponential tail of trap states below the conduction band, they could derive the governing equation (slightly modified here) for charge density in a DSSC as:

$$\frac{\partial n}{\partial t}\frac{dn_l}{dn} = G\exp\left(-\frac{x}{x_\alpha}\right) - \frac{1}{\tau_0}\frac{n^b}{N_0^{b-1}} + D\frac{\partial^2 n}{\partial x^2} \tag{1.10}$$

with boundary conditions:

$$n|_{x=0} = N_0 exp\left(\frac{V}{mkT}\right) \quad \text{and} \quad \frac{\partial n}{\partial x}|_{x=L} = 0 \tag{1.11}$$

n is the free charge density, n_l is the trapped charge density, G is the generation rate, x_α is the decay length for the generation profile, τ_0 is the free carrier

recombination lifetime, b is the power for the recombination law, N_0 is the dark equilibrium free charge density, and D is the diffusion coefficient for free electrons. The three terms on the right hand side of Equation 1.10 simply describe generation, recombination and diffusion, respectively.

Using the governing equation above to simulate SDSC operation yields curves like those displayed in Figure 4.1. At short circuit, the electron density at the anode is held to the (very low) background density, and there is a steep diffusive gradient in density. At open circuit, the profile is homogeneous in the device, and indeed the current is zero because the gradient of charge density is also zero at the collecting electrode. Note that the voltage can be deduced from the charge density at the anode because it is proportional to $\log(\frac{n|_{x=0}}{N_0})$.

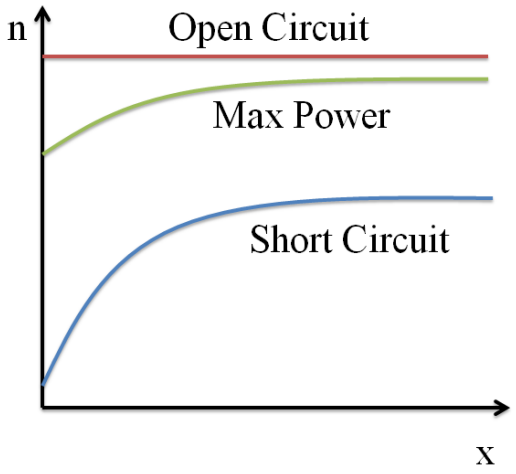

Figure 1.16: Electron density plotted against device position, with the anode at x=0, for various operating conditions of the SDSC. This corresponds to a simple case of linear recombination (b = 1). Units are arbitrary.

The figure of merit when considering electron transport in the SDSC is the collection efficiency, η_c, of electrons that are successfully injected from the dye into the semiconductor. While many researchers aim to achieve enhanced transport, it is ambiguous whether they intend to target a higher free electron diffusion coefficient, a higher effective diffusion coefficient, or a longer diffusion length, but the bottom line, a higher charge collection efficiency, is clearly the objective.

1.4 Aims of this Thesis

Methodologically, we attack the problem in three ways: characterizing, predicting, and synthesizing; the diversity of approaches should be mutually informative, enabling comprehensive conclusions.

1. Generalize existing computational models of charge transport to allow straightforward correlation of empirical data with simulation and account for non-diffusive processes.

2. Critically assess and improve the accuracy of measurements of the collection efficiency, the bottom line metric for investigations of charge transport.

3. Synthesize and characterize novel mesostructures for enhanced charge transport in the SDSC.

The thesis is generally organized around these aims, although interdisciplinarity necessarily means that there is some overlap when correlating projects with aims. Following is a brief organizational overview of the thesis, which was compiled to balance logical presentation of the material with convenient grouping of the aims above. In Chapter 2, we introduce all experimental methods (excluding simulation procedures, which we believe are adequately specified in the relevant chapters) to which subsequent chapters will refer as needed. Chapter 3 will introduce us to the conventionally accepted DSSC modelling literature, along with our novel nondimensionalization, to make simulation results more intuitive. In Chapter 4, we critique conventional charge collection efficiency measurements, taking advantage of nondimensionalization to quickly move between the experimental and simulated domains of data.

Chapters 5 and 6 aim squarely at the last objective above. But for a brief digression into a novel three-dimensional modelling methodology that includes drift as well as diffusion, these chapters introduce different metal oxides and one dimensional nanostructures for electronic transport (Chapter 5) and a novel TiO_2 nanostructure along with its tunable electronic properties (Chapter 6). Finally, in the Conclusion, Chapter 7, we take stock of our progress toward the stated objectives and offer a future outlook for the field.

1.5 References

[1] US Energy Information Administration. International Energy Outlook 2013. Technical report, 2013. 1, 2

[2] Intergovernmental Panel on Climate Change. Renewable Energy Sources and Climate Change Mitigation. Technical report, 2011. 2, 3

[3] United Nations Framework Convention on Climate Change. 2005. 2

[4] S Gupta. Chapter 13: Policies, instruments, and co-operative arrangements. *IPCC*, AR4 WG3, 2007. 2

[5] A. Luque and S. Hegedus. *Handbook of Photovoltaic Science and Engineering*. John Wiley & Sons, 2003. 3

[6] Solarbuzz Research. Solar Module Pricing. Technical report, 2012. http://www.solarbuzz.com/facts-and-figures/retail-price-environment/module-prices. 4

[7] Aidan Lewis. Harnessing Desert Sun to Power Europe. *British Broadcasting Corporation*, December 2011. 4

[8] Fabio Orecchini and Vincenzo Naso. *Energy Resources*. Green Energy and Technology. Springer London, 2012. 5

[9] R.F. Pierret. *Advanced Semiconductor Fundamentals*. Modular series on solid state devices. Addison-Wesley Pub. Co., 1987. 5

[10] S.M. Sze and K.K. Ng. *Physics of Semiconductor Devices*. John Wiley & Sons, 2006. 5

[11] M.A. Green. *Solar cells: operating principles, technology, and system applications*. Prentice-Hall series in solid state physical electronics. Prentice-Hall, 1982. 6

[12] Shyam Mehta. PV News Annual Data Collection Results: 2010 Cell, Module Production Explodes Past 20 GW. *Greentech Media*, May 2011. 12

[13] US National Renewable Energy Laboratory. 2010 Solar Technologies Market Report. Technical report, November 2011. 12

[14] Best Research Cell Efficiencies. National Renewable Energy Laboratory. 2013. http://www.nrel.gov/ncpv/images/efficiency_chart.jpg. 13

[15] Brian O'Regan and Michael Gratzel. A low-cost, high-efficiency solar cell based on dye-sensitized colloidal TiO2 films. *Nature*, 353(6346):737–740, October 1991. 14

[16] Aswani Yella, Hsuan-Wei Lee, Hoi Nok Tsao, Chenyi Yi, Aravind Kumar Chandiran, Md.Khaja Nazeeruddin, Eric Wei-Guang Diau, Chen-Yu Yeh, Shaik M Zakeeruddin, and Michael Gratzel. Porphyrin-sensitized solar cells with Cobalt (ii/iii) based redox electrolyte exceed 12 percent efficiency. *Science*, 334(6056):629–634, 2011. 14

[17] U. Bach, D. Lupo, P. Comte, J. E. Moser, F. Weissortel, J. Salbeck, H. Spreitzer, and M. Gratzel. Solid-state dye-sensitized mesoporous TiO2 solar cells with high photon-to-electron conversion efficiencies. *Nature*, 395(6702):583–585, October 1998. 14

[18] I. Chung, B. Lee, J. He, R.P.H. Chang, and M.G. Kanatzidis. All-solid-state dye-sensitized solar cells with high efficiency. *Nature*, 485(7399):486–489, 2012. 15

[19] H.J. Snaith and L. Schmidt-Mende. Advances in liquid-electrolyte and solid-state dye-sensitized solar cells. *Advanced Materials*, 19(20):3187–3200, 2007. 15, 16, 17

[20] Yousuke Ooyama and Yutaka Harima. Molecular designs and syntheses of organic dyes for dye-sensitized solar cells. *European Journal of Organic Chemistry*, 2009(18):2903–2934, 2009. 16

[21] Henry J. Snaith. Estimating the maximum attainable efficiency in dye-sensitized solar cells. *Advanced Functional Materials*, 20(1):13–19, 2010. 16

[22] H. J. Snaith and M. Grätzel. Enhanced charge mobility in a molecular hole transporter via addition of redox inactive ionic dopant: Implication to dye-sensitized solar cells. *Applied Physics Letters*, 89(26):262114, December 2006. 17

[23] Qingjiang Yu, Yinghui Wang, Zhihui Yi, Ningning Zu, Jing Zhang, Min Zhang, and Peng Wang. High-efficiency dye-sensitized solar cells: The influence of lithium ions on exciton dissociation, charge recombination, and surface states. *ACS Nano*, 4(10):6032–6038, 2010. 17

[24] J.E. Kroeze, N. Hirata, L. Schmidt-Mende, C. Orizu, S.D. Ogier, K. Carr, M. Gratzel, and J.R. Durrant. Parameters influencing charge separation in solid-state dye-sensitized solar cells using novel hole conductors. *Advanced Functional Materials*, 16(14):1832–1838, 2006. 17

[25] Francisco Fabregat-Santiago, Juan Bisquert, Le Cevey, Peter Chen, Mingkui Wang, Shaik M. Zakeeruddin, and Michael Gratzel. Electron transport and recombination in solid-state dye solar cell with Spiro-OMeTAD as hole conductor. *Journal of the American Chemical Society*, 131(2):558–562, 2009. PMID: 19140794. 17

[26] Juan Bisquert. Chemical capacitance of nanostructured semiconductors: its origin and significance for nanocomposite solar cells. *Phys. Chem. Chem. Phys.*, 5:5360–5364, 2003. 17, 18

[27] Annamaria Petrozza, Chris Groves, and Henry J. Snaith. Electron transport and recombination in dye-sensitized mesoporous TiO2 probed by photoinduced charge-conductivity modulation spectroscopy with monte carlo modeling. *Journal of the American Chemical Society*, 130(39):12912–12920, 2008. 19

[28] Jrg Ferber, Rolf Stangl, and Joachim Luther. An electrical model of the dye-sensitized solar cell. *Solar Energy Materials and Solar Cells*, 53(1/2):29 – 54, 1998. 20

[29] Jarl Nissfolk, Kristofer Fredin, Anders Hagfeldt, and Gerrit Boschloo. Recombination and transport processes in dye-sensitized solar cells investigated under working conditions. *The Journal of Physical Chemistry B*, 110(36):17715–17718, 2006. 20

[30] Juan Bisquert and Ivan Mora-Sero. Simulation of steady-state characteristics of dye-sensitized solar cells and the interpretation of the diffusion length. *The Journal of Physical Chemistry Letters*, 1(1):450–456, 2010. 20

[31] Kai Zhu, Nikos Kopidakis, Nathan R. Neale, Jao van de Lagemaat, and Arthur J. Frank. Influence of surface area on charge transport and recombination in dye-sensitized TiO2 solar cells. *The Journal of Physical Chemistry B*, 110(50):25174–25180, 2006. PMID: 17165961. 21

[32] Jenny Nelson, Saif A. Haque, David R. Klug, and James R. Durrant. Trap-limited recombination in dye-sensitized nanocrystalline metal oxide electrodes. *Phys. Rev. B*, 63:205321, May 2001. 21

[33] Juan Bisquert. Fractional diffusion in the multiple-trapping regime and revision of the equivalence with the continuous-time random walk. *Phys. Rev. Lett.*, 91:010602, Jul 2003. 21

[34] Juan Bisquert and Vyacheslav S. Vikhrenko. Interpretation of the time constants measured by kinetic techniques in nanostructured semiconductor electrodes and dye-sensitized solar cells. *The Journal of Physical Chemistry B*, 108(7):2313–2322, 2004. 21

Chapter 2

Experimental Methods and Setup

Figure 2.1 displays chemical structures for materials referenced subsequently in the descriptions of experimental methods.

2.1 Materials Synthesis

2.1.1 Nanowire Synthesis (Chapter 5)

2.1.1.1 SnO_2 Nanowire Synthesis

SnO_2 nanowires were synthesized via a hydrothermal route on titanium foil substrates. The foil was first covered with a compact layer of SnO_2 deposited by spray pyrolysis deposition (butyltin chloride in a 1:10v/v solution of ethanol) and heated to 500°C for 15 minutes. Subsequently, the substrate was mounted vertically in a PTFE-lined autoclave containing 60 mL of the precursor solution; in a typical synthesis this consisted of 0.03M $SnCl_4 \cdot 5H_2O$ added to 0.3M NaOH in the presence of 6M NaCl, stirred for 20 minutes. The autoclave was left at 200°C for 24 hours and the substrate was removed, washed in water and ethanol, and dried at 40°C.[1]

2.1.1.2 ZnO Nanowire Synthesis [2]

ZnO nanowires were created via a two-step solution-based process. First, a seed layer of ZnO was deposited by spin-coating a 0.75 M solution of zinc acetate dihy-

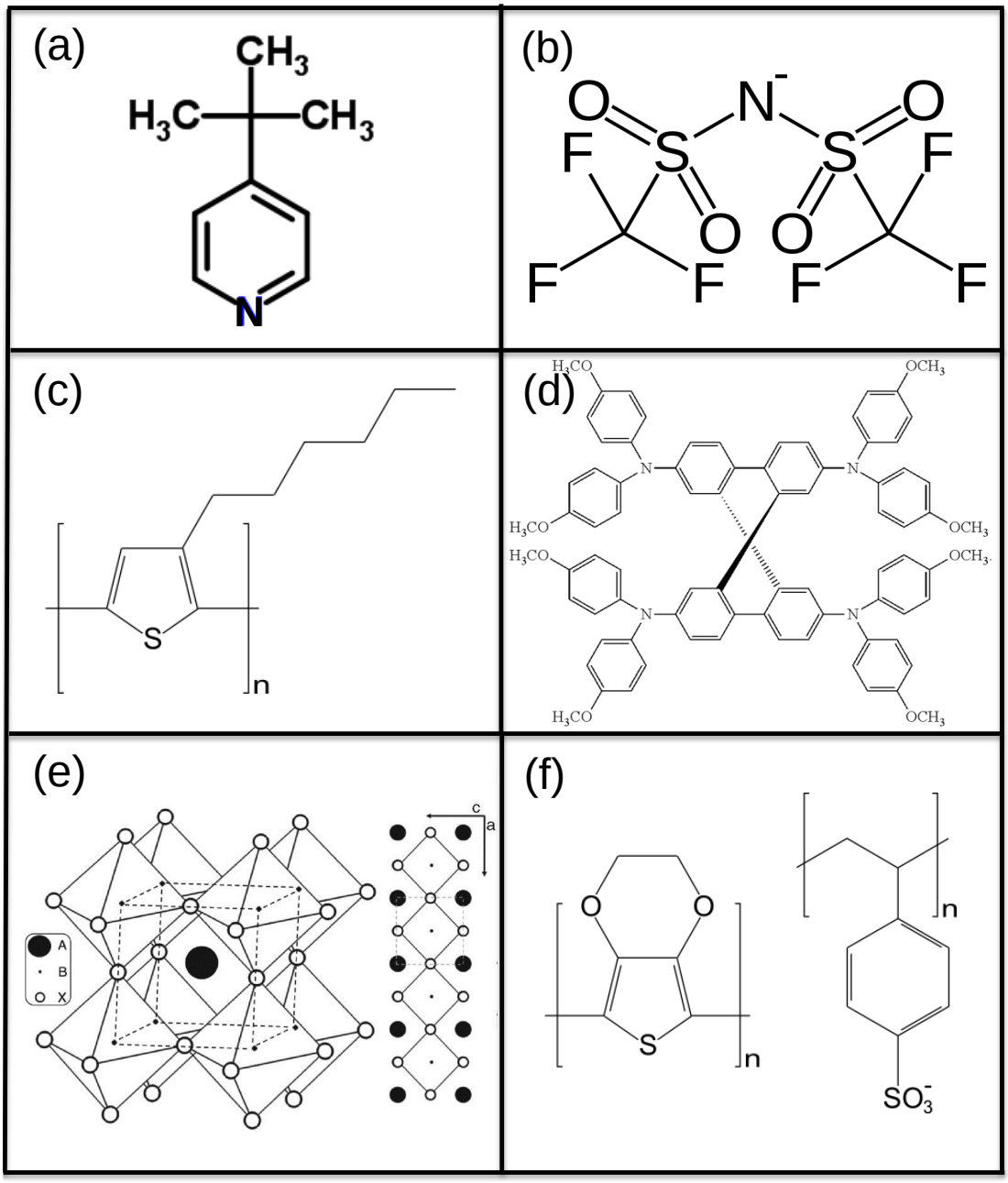

Figure 2.1: (a) 4-tert-butylpyridine (tBP). (b) bis(trifluoromethylsulfonyl)imide (TFSI). (c) Poly(3-hexylthiophene) (P3HT). (d) 2,2',7,7'-tetrakis(N,N-di-p-methoxyphenyl-amine)9,9'-spirobifluorene (Spiro-OMeTAD). (e) Three-dimensional schematic representation of K330 perovskite structure ABX_3 (A = CH3NH3, B = Pb, and X = Cl, I). (f) poly(3,4-ethylenedioxythiophene) poly(styrenesulfonate) (PEDOT:PSS).

drate [$Zn(O_2CCH_3)\cdot 2(H_2O)$, Sigma-Aldrich] and 2-Aminoethanol [$H_2N(CH_2)2OH$, Sigma-Aldrich] in 2-methoxyethanol [$HO(CH_2)2OCH_3$), Sigma-Aldrich] onto indium tin oxide (ITO)-coated glass substrates (PsiOteC UK Ltd; 12 to 16 O/sq).[3] A dense uniform layer was prepared by loading at 500 rpm and increasing the spin speed to 2000 rpm for 30 s. The process was repeated three times with the substrates briefly heated to 300°C between coats. A final 60 min anneal at 450°C was carried out after the layers had been deposited.

In the second step, the as-prepared substrates with ZnO seed layers were suspended upside down in an equimolar (25 mM) solution of HMT [$NH_2(CH_2)6NH(CH_2)6NH_2$, Sigma-Aldrich] and zinc nitrate [$(Zn(NO_2)_2$, Sigma-Aldrich] at 95°C in a similar method described by Vayssieres.[4] The additives 10 mM polyethylenimine [$H(NHCH_2CH_2)_nNH_2$, Sigma-Aldrich] and/or 0.1 M potassium chloride (KCl, Sigma-Aldrich) were added directly to the solution. Following rod deposition the films were rinsed thoroughly with deionized water and allowed to dry at 95°C.

2.1.2 Mesoporous Single Crystals (Chapter 6) [5]

2.1.2.1 Preparation of Mesoporous Silica Templates.

50nm diameter silica spheres were synthesized according to Bogush et al. [6] 32 ml H_2O (Millipore 18M Omega), 18 ml ammonium hydroxide (30 %, Sigma Aldrich) and 99ml tetraethyl orthosilicate (TEOS, Sigma Aldrich) were added to 750ml ethanol and stirred at 700rpm for 24 hours. A quasi close-packed bead template was prepared by centrifugation of the reaction solution (7000 rpm, 5 h) leaving a translucent solid. The (unwashed) solid was sintered at 500 °C for 30 min (ramping time 150 min).

2.1.2.2 Pre-seeding of Silica templates.

A $TiCl_{4(aq)}$ solution (15 μM to 15 mM) was prepared by aqueous dilution of a 2 M $TiCl_{4(aq)}$ stock solution (stock preparation: 100 ml of $TiCl_4$ (Sigma Aldrich) was added to 350 ml H_2O containing 1 mL of 35 % HCl in an ice bath). 5 g of the sintered template was immersed in 33 ml of $TiCl_{4(aq)}$ and held at 70 °C for 60 min

followed by thorough rinsing with 1 l H_2O. The dried template was resintered at 500 °C for 30 min (ramping time 150 min). The ratio of titanium to silicon (wt/wt) present in the treated template was determined by inductively coupled plasma optical emission spectrometry after microwave digestion in hydrofluoric acid (ICPOES, Exeter Analytical).

2.1.2.3 Synthesis of TiO_2.

Mesoporous TiO_2 crystals were synthesized hydrothermally using a modified version of the procedure reported by Zhang et al.[7]. Titanium tetrafluoride (TiF_4, Alfa Aesar) was dissolved in 18 MΩ H_2O (at concentrations from 20 mM to 400 mM) after first adjusting the pH to 2.1 by addition of 37% HCl (200 μl in 250 ml). 1.67 ml of the ionic liquid 1-methylimidazolium tetrafluoroborate, and 650 mg of the pre-treated silica template were added to 50 ml of TiF_4 solution in a 125 ml volume PTFE-lined autoclave (Parr Instruments). The sealed vessel was brought to the target reaction temperature (100-210 °C) in a fan-assisted oven for the period of the reaction before cooling in air over approximately 1 hr. The template product was collected as a solid white powder settled at the base of the vessel and rinsed with H_2O by vacuum filtration on 1.2 μm paper (Whatman). In some cases, the dry podwer product was sintered at temperatures between 500-850°C for 45 minutes. The silica template was selectively etched in 2 M $NaOH_{(aq)}$ at 80 °C for 60 min in a polypropylene beaker. The remaining TiO_2 was collected by centrifugation (3000 rpm, 60 min) and washed twice with 50 ml H_2O, and twice with 50 ml ethanol.

2.2 Solid State Dye Sensitized Solar Cell Assembly

(Although many different device architectures are presented in this thesis, most are variants of a general process flow employed in standard solid-state dye sensitized solar cell (SDSC) fabrication; therefore, we present the standard process first and architecture specific deviations subsequently.)

2.2.1 Standard Cell Assembly

A schematic and SEM cross-sectional image of the standard SDSC is displayed in Figure 2.2.

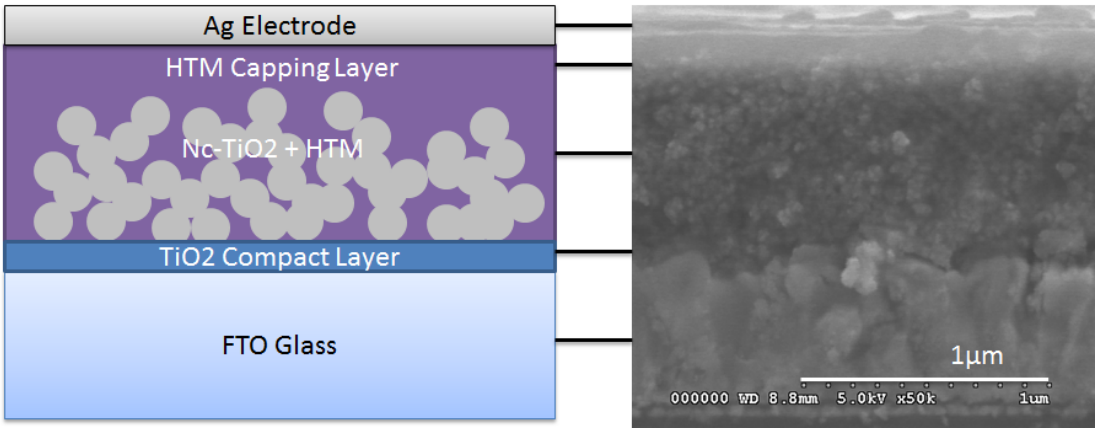

Figure 2.2: Left Panel: schematic of the SDSC; Right Panel: cross-sectional SEM image illustrating correspondence to schematic components.

2.2.1.1 FTO Electrode Preparation

FTO-coated glass sheets ($15\Omega cm^{-1}$ Pilkington) were etched with zinc powder and HCl (2M) to obtain the required electrode pattern. This consisted of protecting part of the substrate with scotch tape, applying the Zn and HCl concurrently, and vigorously brushing with a toothbrush to remove the FTO from the required areas. Finally, the substrates were extensively rinsed with water. The sheets were then washed with soap (2% Hellmanex in water), deionized water, acetone, and methanol, and finally treated under oxygen plasma for 10min to remove the last traces of organic residues. The desired electrode pattern and etching method are demonstrated in Figure 2.3.

2.2.1.2 Metal Oxide Compact Layer Deposition

We subsequently deposited a compact layer of the particular metal oxide to be used as the photoanode. In this thesis, we present devices based on three different metal oxides—TiO_2, ZnO, and SnO_2—so we present below compact layer

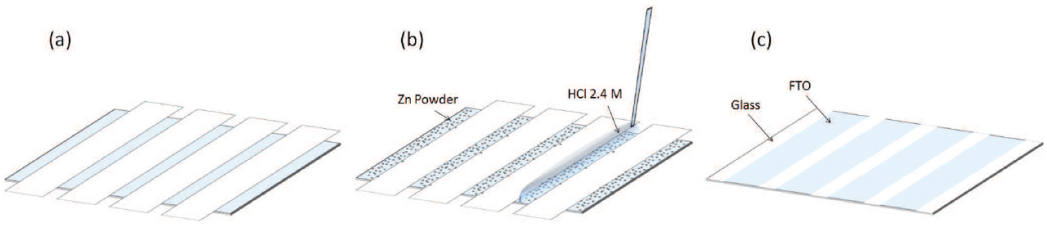

Figure 2.3: FTO etching procedure schematic. (a) FTO sheet with scotch tape applied to protect device active areas. (b) Application of Zn powder and HCl for etching. (c) Electrode pattern following etching. Reprinted with permission from [8].

deposition techniques for each metal oxide.

TiO_2: Titanium diisopropoxide bis(acetylacetonate) (Ti-Acac) 75% by weight in isopropanol was added to ethanol in a 1:10 Ti-Acac:Ethanol volumetric ratio to comprise a total solution volume of 6.6mL.[9; 10] The solution was subsequently sprayed through spray pyrolysis deposition, with air as the carrier gas, on substrates heated to 300°C. A schematic of the spraying process is displayed in Figure 2.4; the sprayer was held at arm's length from the substrate. Subsequently, the substrates were left at temperature for 20 minutes and then left to cool to room temperature.

ZnO: The spraying protocol was identical to that of TiO_2. The spraying solution consisted of 6mL of 100mM Zinc acetate dihydrate in anhydrous methanol.[11]

SnO_2: The spraying protocol was identical to that of TiO_2 except for the spraying temperature, which was held at 500°C. To prepare the spraying solution, two 6.6mL solutions of butyltin trichloride in ethanol were prepared in a 1:10 precursor:ethanol volumetric ratio.

2.2.1.3 Mesoporous Paste Deposition

A mesoporous metal oxide layer in the vicinity of 2μm was deposited through screen printing. Again we present the paste preparation methods for each metal oxide used. Upon film deposition, the substrates were sintered at a temperature of 500°C for 45 minutes (TiO_2 and SnO_2) or 400°C for 45 minutes (ZnO).

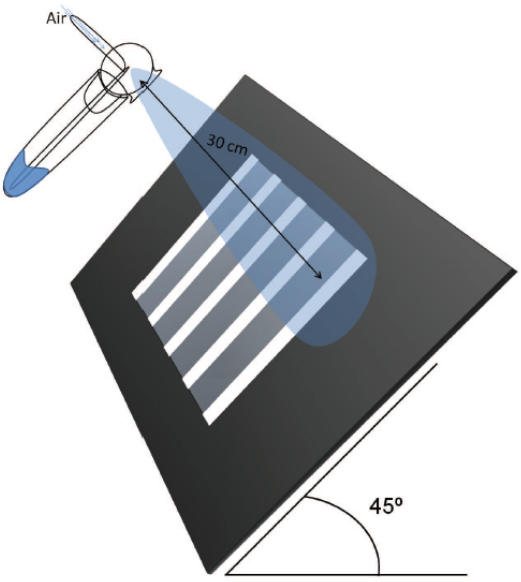

Figure 2.4: Spray pyrolysis deposition schematic illustrating position of the sprayer and substrate tilt angle. Reprinted with permission from [8]

TiO_2: Dyesol paste 18NR-T is composed of ∼20nm anatase TiO_2 nanoparticles in a mixture of ethyl cellulose. The paste was diluted with terpineol at a ratio of 0.3:1 terpineol:paste by weight. The paste was finally stirred and shaken for 24 hours.

ZnO: A colloidal dispersion of ZnO nanparticles 40% by weight in ethanol (721085 Sigma-Aldrich) was mixed with terpineol, butylamine, and a mixture of ethyl cellulose 10 % by weight in ethanol. First, a 1:1 by weight mixture of ethyl cellulose with different viscosities (5-15 mPa.s, 46070 Sigma and 30-70 mPa.s, 46080 Sigma) was added slowly into ethanol while under vigorous stirring to achieve a final concentration of 10 wt%. Then, for every gram of the ZnO dispersion, 0.83mL of bultyamine and 2.5g of terpineol were mixed, stirred and sonicated for 30s with an ultrasonic horn. After this step, 3.75g of the ethyl cellulose mixture in ethanol were added, stirred and sonicated for 30s. After sonication, ethanol was completely removed from the paste via rotary evaporation.

SnO_2: SnO_2 paste was prepared using SnO_2 nanoparticles less than 100nm in

diameter, following the method proposed by Ito et al.[12] 1.6g of the nanoparticle powder was ground with mortar and pestle under the addition of 167μL acetic acid, 833μL of deionized water, and sufficient ethanol for mixture consistency. After the elimination of all macro-aggregates, the mixtre was sonicated, and 3.33g terpineol and 4g of the cellulose solution described above were added. Finally, ethanol was removed from the paste by rotary evaporation.

2.2.1.4 Surface Treatment

We applied different surface treatments depending on which metal oxide comprised the mesoporous layer: TiO_2 was applied to SnO_2 and TiO_2 while MgO was applied to ZnO and Sn_2 devices. Upon surface treatment, the substrates were re-sintered at a temperature of 500°C for 45 minutes (TiO_2 and SnO_2) or 400°C for 45 minutes (ZnO). In one experiment we present (in Chapter 3), we replace the TiO_2 shell on the TiO_2 mesostructure with a variable thickness alumina shell and therefore describe that process below as well.

TiO_2 treatment: Substrates were immersed in a solution of 15mM $TiCl_4$ in water, and left for one hour at 70°C. The substrates were subsequently removed, rinsed in the same solvent, and left to dry while standing.[13; 14]

MgO treatment: Substrates were immersed in a 20mM solution of magnesium acetate tetrahydrate in ethanol, and left for one minute at 100°C in a closed container. The substrates were subsequently removed, rinsed in the same solvent, and left to dry while standing.[15]

Al_2O_3 treatment: Substrates were immersed for 1-20 minutes in a solution of 10mM aluminum isopropoxide in a 1:1 solution of tert-butanol:acetonitrile. The substrates were subsequently removed, rinsed in the same solvent, and left to dry while standing.

SiO_2 Treatment: Substrates were immersed in a basic solution of tera-ethyl orthosilicate in ethanol for five minutes at room temperature. The substrates were subsequently removed, rinsed in the same solvent, and left to dry while standing.

2.2.1.5 Final Processing Steps

After the resintering procedure, the substrates were cooled down to 70° C and finally submersed in a dye solution for 1h. The indolene dye used was D102, 0.2mm in a 1:1 volume ratio of tert-butanol and acetonitrile. Spiro-OMeTAD was dissolved in chlorobenzene at 10% by volume and then heated up to 100°C.[16] After fully dissolving the hole transporter, 4-tert-butyl pyridine (tBP) was added with a volume-to-mass ratio of 1:26μL mg^{-1} tBP:Spiro-OMeTAD.[17] Lithium bis(trifluoromethylsulfonyl)imide salt (Li-TFSI) was predissolved in acetonitrile at 170mgmL^{-1}, then added to the hole transporter solution at 1:12μL/mg of Li-TFSI solution:Spiro-OMeTAD, corresponding to a concentration of 10mM Li-TFSI in the solution.

The dyed films were rinsed briefly in acetonitrile and dried in air for one minute. Then a small quantity of the hole transporter solution, 18-25μL, was dispensed onto each substrate and left to wet the films for 20s before spin-coating at 2000rpm for 25s in air. The films were left for a minimum period of 4h in air before placing them in a thermal evaporator where 150 to 300nm thick silver electrodes were deposited through a shadow mask under high vacuum (10−6mbar). The active area of the devices was defined by a metal optical mask with 0.1256cm^2 aperture.

2.2.2 SnO_2/P3HT SDSC (Chapter 5)

We now indicate deviations from the standard process flow described above for special architectures introduced in this thesis. In the case of SnO_2/P3HT devices, the compact layer and hole transporter deposition were different.

2.2.2.1 Compact Layer Deposition

Compact layer deposition of SnO_2 was accomplished either by spincoating or through spray pyrolysis deposition. The spin coating solution was prepared by adding anhydrous acetic acid to a solution of tetra isopropoxy tin isopropanol (Gelest) in anhydrous ethanol (8% by weight). The solution was filtered using a 0.45 μm syringe filter and spin coated on patterned FTO at 2000 rpm. A compact

SnO_2 layer was formed by heating the resulting film at 500°C for 30 min. Spray pyrolysis deposition was performed as described above. During the deposition of the compact layer, the etched parts of electrodes were masked so that the SnO_2 only covered the FTO. The substrate was then annealed at 500°C for 30 minutes to form a 100 nm SnO_2 compact layer.

2.2.2.2 P3HT Deposition

Over the dye coated electrode (note: we used ID504 sensitizer instead of D102, but the dyeing protocol remains the same), 25 μL of additive solution was dispensed onto each cell and left about 20 s to wet the films before spin-coating at 1200 rpm for 45 s. The additive solution consisted of Li-TFSI and TBP in anhydrous acetonitrile. Poly(3-hexylthiophene) (P3HT, Rieke) was dissolved in anhydrous chlorobenzene at different concentrations, ranging from 20 mg/ml to 90 mg/ml. The samples were spin-coated with two layers of P3HT. The first layer of P3HT (20 mg/ml) was left to infiltrate the mesoporous SnO_2 for 20 seconds prior to spin-coating at 1200 rpm for 40 seconds. A second layer, to ensure an adequate capping layer, was spun immediately after dispensing the first P3HT layer. Finally a 200 nm-thick silver layer was thermally evaporated on the polymer surface as a counter electrode in a chamber with pressure of $\sim 10^{-6}$ Torr.

2.2.3 SnO_2 Nanowire Flexible SDSCs

SnO_2 nanowires were grown on Titanium foil substrates coated with a SnO_2 compact layer as described earlier. A TiO_2 surface treatment was applied pursuant to the protocol described in the standard cell procedures. Next, the substrates were either immersed in D102 solution, as described earlier, or spin coated with K330 perovskite solution (preparation and deposition of the 10% mixed halide organometalic perovskite sensitizer was as outlined by Lee et al.[18]). Then a solution of PEDOT:PSS, filtered through 1μm glass microfibers and diluted 3:1 with methanol, was spincoated at 2000 rpm to produce a conductive top layer for lateral transport. Upon drying at 100°C for ten minutes, 15nm of gold and 200nm of silver were evaporated on top to produce the requisite electrode pattern.

A schematic of the SnO_2 flexible nanowire SDSC is displayed in Figure 2.5.

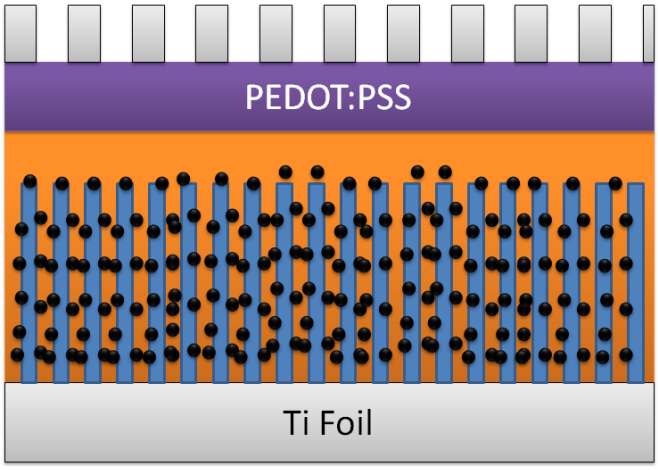

Figure 2.5: Schematic illustration of the constituent components of the SnO_2 nanowire SDSC. The blue wires and black dots correspond to SnO_2 nanowires and perovskite sensitizer, respectively.

2.2.4 ZnO Nanowire SDSCs

ZnO nanowires were synthesized on FTO coated glass substrates with TiO_2 compact layers already deposited. Subsequent to the ZnO nanowire hydrothermal synthesis and sintering at 400° for 45 minutes, one of three surface treatments was applied. MgO bath deposition is described earlier. ZnS treatment entailed immersion in 0.16M Na_2S solution for two hours at 60° and then immersion of the rinsed substrate in 0.16M zinc nitrate aqueous solution at the same temperature for 2 hours.[19] The last alternative was TiO_2 chemical bath deposition, which entailed immersion of pre-cooled substrates in a 40mM $TiCl_4$ solution for seven minutes at 4°C. Finally, the substrates were resintered at 400° for 45 minutes.

The rest of the process flow proceeded according to the standard cell protocol described above. For P3HT cells, P3HT was dissolved at 40mg/mL in chlorobenzene and spin-coated over the dye sensitized film.

2.2.5 Mesoporous Single Crystal (MSC) SDSCs

The synthesis of MSCs is described above. A TiO_2 compact layer was deposited by spin-coating on cleaned fluorine-doped tin oxide (FTO) coated glass substrates. The compact layer spin-coating solution was prepared by adding 0.71g Titanium

Isopropoxide and 0.07g HCl to 8mL of ethanol. After drying the compact layer at 150°C for thirty minutes, the TiO_2 MSC mesostructure was deposited by spin-coating a solution of MSCs dispersed in ethanol at 10% concentration by weight. The substrates were again dried at 150°C and subsequently immersed in the sensitizing solution containing D102 organic dye. After one hour of immersion, the substrates were removed and rinsed in acetonitrile, and the Spiro-OMeTAD hole transporter layer was deposited by spin-coating on top of the dye-sensitized mesostructure. The hole-transporter spin-coating solution consisted of Spiro-OMeTAD dissolved in chlorobenzene at a concentration of 180mg/mL, along with additives tert-butylpyridine and Lithium-TFSI. Finally, 200nm thick silver electrodes were evaporated over the hole transporter layer to form the counter-electrode.

2.3 Characterization Methods

2.3.1 Solar Cell Characterization

2.3.1.1 Solar Simulator Measurements

To characterize the JV characteristics of the solar cells, AM1.5 light at 100 mW/cm^2 was generated using an ABET solar simulator calibrated using an NREL calibrated silicon reference cell with a KG5 filter to minimize spectral mismatch. JV curves were measured with a Keithley 2400 unit. The solar cells were masked with a metal aperture to define the active area and to eliminate any edge effects.[20]

2.3.1.2 Small Perturbation Transient Decay Measurements

Transient current and voltage decay measurements were performed in the following manner: a white light bias was generated from an array of diodes (Lumiled Model LXHL-NWE8 whitestar) with red-light pulsed diodes (LXHLND98 red-star, 200μs square pulse width, 100ns rise and fall time) as the perturbation source, controlled by a fast solid-state switch. The signal for transient current decay at short circuit was recorded through a low impedance port (50Ω) on a

1GHz Agilent oscilloscope. The voltage decay measurements in the short circuit regime were accomplished by connecting a Keithley 2400 sourcemeter in series with the solar cell and in parallel with the oscilloscope set to the high (1MΩ) impedance port. The Keithley sourced the current through the solar cell, which was under bias illumination, in such a way to maintain the current at its short circuit value under bias illumination and no pulse.

Figure 2.6 illustrates the fitting protocol for a sample current or voltage decay—the latter portion of the decay exhibiting monoexponential decay was fit, ignoring the initial, rapid decay.

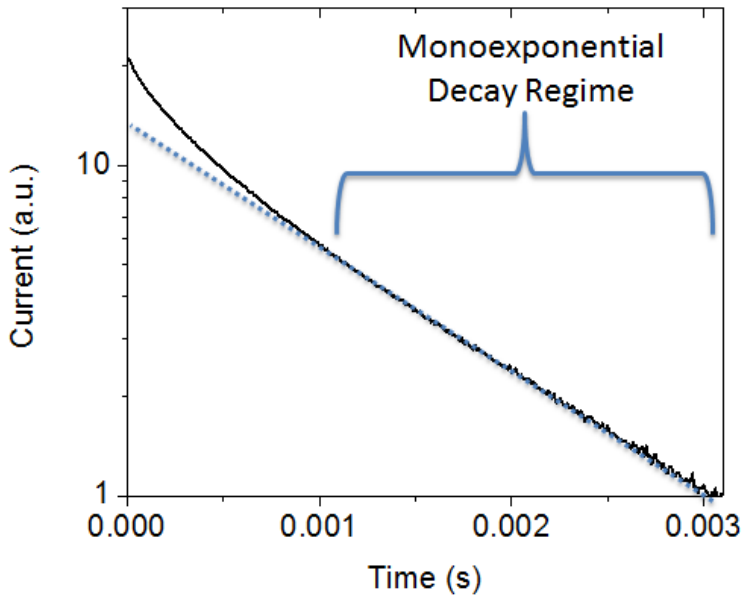

Figure 2.6: Sample transient photocurrent decay demonstrating the division of the observed decay into an initial, rapid decay, and a subsequent monoexponential decay. Experimental protocol involved ignoring the first portion and only fitting the latter, monoexponential portion.

The charge density at short circuit was obtained by integrating the current flow after switching off the background light bias. To calculate the density of states, a voltage decay was measured at open circuit and correlated with the charge density at short circuit for the given background light intensity, obtained

by integrating the area under the short circuit current decay. Thus one can extract a plot of chemical capacitance vs. V_{OC}, a measure of the electronic density of states.[21]

2.3.1.3 SEM Characterization

Scanning electron microscopy: cross sectional and top-view SEM imaging of devices and films were performed on a Hitachi S 4300 SEM with a 5 kV acceleration voltage.

2.3.2 MSC Conductivity Characterization

2.3.2.1 Conductivity Device Fabrication

A TiO_2 compact layer was deposited, as described above, on a glass substrate, and 10nm gold electrodes were evaporated, defining a continuous channel 33mm in length and 6.529cm in width. MSC films were subsequently deposited and processed as described above, either with dye and additive-laden Spiro or as neat films. Finally, to expose the electrode contacts, cotton swabs with ethanol were used to gently scratch off the MSC film; subsequently, silver dag was applied to improve electronic contact at the electrodes.

2.3.2.2 Transient Mobility Spectroscopy

This method is described in detail elsewhere by Leijtens et al.[22] Briefly, pump probe spectroscopy is used to monitor the absorption signature of the photoinjected charge in the device. Conductivity devices are fabricated as described above with C106 sensitizing dye and no hole transporter. The pump wavelength is 550nm to excite the dye molecules and induce charge photoinjection, and the probe wavelength of 900nm measures the population of dye cations; simultaneously, the conductivity is measured. This allows extraction of conductivity and photoinduced charge density as a function of time, enabling calculation of the charge mobility as a function of charge density.

2.3.2.3 Single Crystal Conductivity Measurements

Film conductivities were measured using the same experimental setup as solar cell efficiency characterization, measuring the current voltage characteristic under a solar simulator. Vacuum conductivity measurements entailed sealing devices in a portable box, purging it with argon, and evacuating below 10^{-2} torr.

MSC single crystal conductivity measurements were taken using two probe contact to gold electrodes with a single MSC crystal bridging the gap between. To accomplish this, several pairs of gold electrodes were fabricated on silicon substrates using electron beam lithography, such that the electrodes could be contacted macroscopically, but narrowed to a width of 2.5μm with a gap between them of 500nm (see Figure 2.7). Subsequently, MSCs dissolved 1:10 w/w in ethanol were dropcasted on the silicon substrate, dried, and examined under a scanning electron microscope to determine the exact MSC geometric parameters and which electrodes were actually connected by a single MSC.

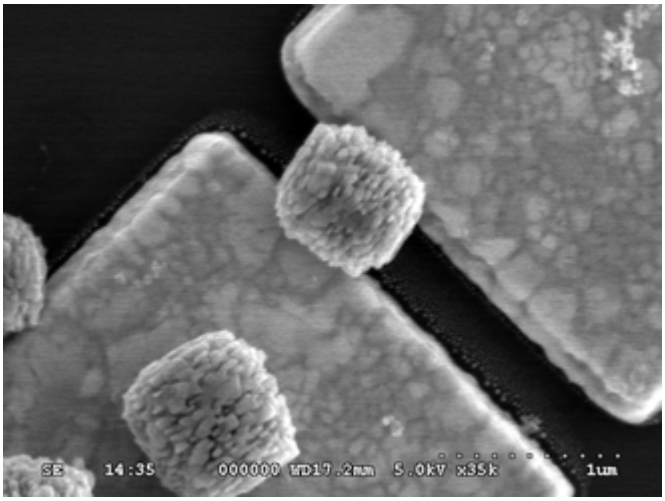

Figure 2.7: SEM image of the experimental setup used to measure the conductivity of a single MSC, which in this image bridges the gap between two gold electrodes fabricated using electron beam lithography

2.4 References

[1] Ya-Li Wang, Min Guo, Mei Zhang, and Xi-Dong Wang. Hydrothermal preparation and photoelectrochemical performance of size-controlled SnO2 nanorod arrays. *CrystEngComm*, 12(12):4024–4027, 2010. 28

[2] Jonathan Downing, Mary P. Ryan, Natalie Stingelin, and Martyn A. McLachlan. Solution processed hybrid photovoltaics: preparation of a standard ZnO template. *Journal of Photonics for Energy*, 1(1):011117–011117–9, 2011. vi, 28

[3] M. Ohyama, H. Kouzuka, and T. Yoko. Sol-gel preparation of ZnO films with extremely preferred orientation along (002) plane from zinc acetate solution. *Thin Solid Films*, 306(1):78–85, 1997. 30

[4] L. Vayssieres. Growth of arrayed nanorods and nanowires of ZnO from aqueous solutions. *Advanced Materials*, 15(5):464–466, 2003. 30

[5] Edward Crossland and Henry J Snaith. Seeded nucleation and growth of mesoporous single-crystals of anatase TiO2. 2012. vi, 30

[6] G.H. Bogush, M.A. Tracy, and C.F. Zukoski IV. Preparation of monodisperse silica particles: Control of size and mass fraction. *Journal of Non-Crystalline Solids*, 104(1):95, 1988. 30

[7] Dieqing Zhang, Guisheng Li, Xianfeng Yang, and Jimmy C. Yu. A micrometer-size TiO2 single-crystal photocatalyst with remarkable 80 *Chem. Commun.*, (29):4381, 2009. 31

[8] Pablo Docampo. *Electronic Properties of Mesostructured Metal Oxides in Dye-Sensitized Solar Cells*. PhD thesis, Oxford University, 2012. 33, 34

[9] L. Kavan and M. Gratzel. Highly efficient semiconducting TiO2 photoelectrodes prepared by aerosol pyrolysis. *Electrochimica Acta*, 40(5):643–652, 1995. 33

[10] Petra J. Cameron and Laurence M. Peter. Characterization of titanium dioxide blocking layers in dye-sensitized nanocrystalline solar cells. *The Journal of Physical Chemistry B*, 107(51):14394–14400, 2003. 33

[11] F. Paraguay D, W. Estrada L, DR Acosta N, E. Andrade, and M. Miki-Yoshida. Growth, structure and optical characterization of high quality ZnO thin films obtained by spray pyrolysis. *Thin Solid Films*, 350(1):192–202, 1999. 33

[12] S. Ito, P. Chen, P. Comte, M.K. Nazeeruddin, P. Liska, P. Péchy, and M. Grätzel. Fabrication of screen-printing pastes from TiO2 powders for dye-sensitised solar cells. *Progress in photovoltaics: research and applications*, 15(7):603–612, 2007. 35

[13] PM Sommeling, BC O'Regan, RR Haswell, HJP Smit, NJ Bakker, JJT Smits, JM Kroon, and JAM Van Roosmalen. Influence of a TiCl4 post-treatment on nanocrystalline TiO2 films in dye-sensitized solar cells. *The Journal of Physical Chemistry B*, 110(39):19191–19197, 2006. 35

[14] Brian C. O'Regan, James R. Durrant, Paul M. Sommeling, and Nicolaas J. Bakker. Influence of the TiCl4 treatment on nanocrystalline TiO2 films in dye-sensitized solar cells; charge density, band edge shifts, and quantification of recombination losses at short circuit. *The Journal of Physical Chemistry C*, 111(37):14001–14010, 2007. 35

[15] Priti Tiwana, Pablo Docampo, Michael B. Johnston, Henry J. Snaith, and Laura M. Herz. Electron mobility and injection dynamics in mesoporous ZnO, SnO2, and TiO2 films used in dye-sensitized solar cells. *ACS Nano*, 5(6):5158–5166, May 2011. 35

[16] U. Bach, D. Lupo, P. Comte, J. E. Moser, F. Weissortel, J. Salbeck, H. Spreitzer, and M. Gratzel. Solid-state dye-sensitized mesoporous TiO2 solar cells with high photon-to-electron conversion efficiencies. *Nature*, 395(6702):583–585, October 1998. 36

[17] J. Kruger, R. Plass, L. Cevey, M. Piccirelli, M. Gratzel, and U. Bach. High efficiency solid-state photovoltaic device due to inhibition of interface charge recombination. *Applied Physics Letters*, 79(13):2085–2087, 2001. 36

[18] Michael Lee and Henry Snaith. 10 percent efficient solar cells consisting of perovskite-sensitized mesoporous alumina infiltrated with a solid state hole transporter. 37

[19] Jinhua Li, Dongxu Zhao, Xiuqing Meng, Zhenzhong Zhang, Jiying Zhang, Dezhen Shen, Youming Lu, and Xiwu Fan. Enhanced ultraviolet emission from zns-coated ZnO nanowires fabricated by self-assembling method. *The Journal of Physical Chemistry B*, 110(30):14685–14687, 2006. 38

[20] Henry J Snaith. How should you measure your excitonic solar cells? *Energy & Environmental Science*, 5(4):6513–6520, 2012. 39

[21] B. C. O'Regan, S. Scully, A. C. Mayer, E. Palomares, and J. Durrant. The effect of Al2O3 barrier layers in TiO2/dye/CuSCN photovoltaic cells explored by recombination and dos characterization using transient photovoltage measurements. *J. Phys. Chem. B*, 109(10):4616–4623, February 2005. 41

[22] Tomas Leijtens, Jongchul Lim, Joel Teuscher, Taiho Park, and Henry J. Snaith. Charge density dependent mobility of organic hole-transporters and mesoporous TiO2 determined by transient mobility spectroscopy: Implications to dye-sensitized and organic solar cells. *Advanced Materials*, 25(23):3227–3233, 2013. 41

Chapter 3

Overview of DSSC Modelling

3.1 The Continuity Equation

In order to present a novel modelling approach, we will in this section first review the existing literature. We begin by examining in greater detail the governing continuity equation for the DSSC observed earlier in Equations 1.10 and 1.11 (repeated below):

$$\frac{\partial n}{\partial t}\frac{dn_l}{dn} = G\exp\left(-\frac{x}{x_\alpha}\right) - \frac{1}{\tau_0}\frac{n^b}{N_0^{b-1}} + D\frac{\partial^2 n}{\partial x^2} \tag{1.10}$$

with boundary conditions:

$$n|_{x=0} = N_0 exp\left(\frac{V}{mkT}\right) \quad \text{and} \quad \frac{\partial n}{\partial x}|_{x=L} = 0 \tag{1.11}$$

Recall that n is the free charge density, n_l is the trapped (or localized) charge density, G is the generation rate, x_α is the decay length for the generation profile, τ_0 is the free carrier recombination lifetime, b is the power for the recombination law, N_0 is the dark equilibrium free charge density, and D is the diffusion coefficient for free electrons. The three terms on the right hand side of Equation 1.10 simply describe generation, recombination and diffusion, respectively. The first boundary condition expresses the relationship between conduction band charge density at the working electrode and the applied voltage; this is known as the ideality of the device, where m is the diode ideality factor and k is Boltzmann's

Constant. The second condition stipulates that no electron injection can occur at the counterelectrode.

To arrive at Equation 1.10, we have to modify the conventional equations for electron transport in a bulk semiconductor in several ways. First, we discard drift, a common assumption made in the DSSC literature that we will revisit later.[1] Then we must account for "sticky" electron transport, or the trapping phenomenon where energetic states below the conduction band, arising from the nanocrystalline nature of the semiconductor, prevent electrons from diffusing according to Fick's Law. [2] To do so, Bisquert and Vikhrenko made the "quasistatic" approximation, whereby they assume that trapping and detrapping events take place on a much faster time scale than all other electronic processes.[3] As a result, they can express the density of trapped charge as a univariate function of the free charge density. The quasistatic approximation is equivalent to:

$$\frac{\partial n_l}{\partial t} = \frac{\partial n_l}{\partial n}\frac{\partial n}{\partial t} \tag{3.1}$$

Without this approximation, the electron continuity equation would have had to take into account all electrons, irrespective of whether they were trapped or free. With Equation 3.1, we can rewrite the total electron current, or the time derivative of the total charge, as:

$$\frac{\partial n + \partial n_l}{\partial t} = \frac{\partial n}{\partial t}\left(1 + \frac{\partial n_l}{\partial n}\right) \approx \frac{\partial n}{\partial t}\frac{\partial n_l}{\partial n} \tag{3.2}$$

The final step is based on the approximation that there are far more trapped than free electrons, allowing us to retain only the second term in parentheses. The beauty of the quasistatic approximation is that the continuity equation can now be written in terms of the free electron density, using familiar terms like the free electron diffusion coefficient. In order to write this, we need one final piece of information: the relationship between free and trap state occupancy changes. An exponential density of trap states appears to fit observed experimental data and also gives us the analytical expression we seek.[4] Explicitly, we can fit the trap density of states by:

$$n_l = N_{l0} exp\left(\frac{\beta E_f}{kT}\right) \tag{3.3}$$

where β is the parameter that specifies the exponential distribution of trap states. Then, recalling

$$n = N_0 exp\left(\frac{E_f}{mkT}\right) \tag{3.4}$$

we can deduce that

$$\frac{\partial n_l}{\partial n} = m\beta \frac{N_{l0}}{N_0^{m\beta}} n^{m\beta-1} \tag{3.5}$$

This removes all reference to the trapped charge density from the governing equation, once we substitute Equation 3.5 into Equation 1.10. We now proceed to investigate the various terms in the governing equation and how they relate to device operation more closely.

3.1.1 Origin of the Photovoltage

The photovoltage in the DSSC is determined by the difference between the electron Fermi level, E_F, between the two contacts.[5] In the dark, equilibrium stipulates a constant Fermi level across the device, and in dye cells, this corresponds to the redox potential of the electrolyte; in the SDSC, the analogue is the oxidation potential of the hole conductor.[6]

The electron density in a semiconductor is given by:

$$n = N_C exp - \left(\frac{E_C - E_F}{kT}\right) \tag{3.6}$$

In the dark, the Fermi level in the TiO_2 is pinned to that of the hole transporter. Under illumination, the density of free electrons of the TiO_2 increases as electrons are injected into the conduction band from excited dye molecules, causing a corresponding increase in the photovoltage. This steady-state distribution of electrons under constant illumination, the summation of competing generation, extraction, and recombination terms, defines a quasi-Fermi level ${}_nE_F$, which under open circuit conditions is roughly constant over the device thickness since no

charge is extracted.[7]

The dependence of the photovoltage on light intensity has been carefully studied, because it is a measure of the ideality of the diode behavior. If the DSSC behaved as an ideal diode, we would expect Equation 3.6 to imply the following relation between the open circuit photovoltage and electron concentrations in the light and dark:

$$V_{OC} = \frac{1}{q}({}_nE_F - E_{F,Spiro}) = \frac{k_BT}{T} ln \frac{n_{light}}{n_{dark}} \tag{3.7}$$

Equation 3.7 predicts that the open circuit voltage should increase by 59mV per decade of light intensity increase, assuming that charge generation is proportional to light intensity.[8] However, actual values rarely come close to this theoretical prediction; measured values of the photovoltage increase approach 120 mV per decade of light intensity increase.[9]

The governing equation we have postulated accounts for this nonideality in both a theoretical and practical sense. We might explain the deviation from the Shockley diode equation behavior by appealing to two nonideal processes occurring in the TiO_2: transport and recombination. Diffusive electron transport, as noted earlier, is not governed by the product of free electron diffusion coefficient and charge density gradient; rather, the effective diffusion coefficient increases with increasing light intensity (and hence charge density).[10] Recombination is similarly nonlinear, and there are several studies demonstrating sublinear recombination rates as a function of charge density.[11; 12]

Equation 1.10 includes a parameter, b, for the nonlinearity of recombination and a nonideality parameter, m, for the transport related nonideality. Thus we theoretically partition the sources of nonideality but the factors m and b are practically fudge factors to match empirical observation. Now we can deduce the relationship between open circuit voltage and light intensity for our nonideal diode by assuming the open circuit condition of constant charge density in time and space. This is not strictly valid for an exponential charge generation profile, but it is close to accurate. Substituting the left boundary condition 1.11 into Equation 1.10 at steady state allows us to write:

$$\frac{V_{OC}}{kT} \propto \frac{m}{b} log(\Phi) \tag{3.8}$$

where Φ is the illumination intensity; this suggests that $\frac{m}{b}$ is the appropriate ideality factor for our solar cell. Values between 1 and 2 for this ratio fit well with empirical observations.

3.1.2 Diffusion Length

The diffusion length is an intensively studied parameter because of its value as a summary statistic; as described in the Introduction, a device with a diffusion length over twice the device thickness will have a high charge collection efficiency. In order to understand the diffusion length, we must first investigate its two components: the diffusion constant and the electron lifetime.

Early in the research history of the DSSC, prior to application of the multiple trapping framework to describe charge transport, authors failed to distinguish between the free electron diffusion coefficient, D_0 (which we have abbreviated to D for convenience in our exposition of the governing equations), and the effective diffusion coefficient, D_n.[13] The latter term abstracts away the particulars of trapping such that Fickean diffusion is obeyed.[14] The analogue for the electron lifetime is an effective electron lifetime term, τ_n, which characterizes the net recombination time for a composite of trapped and free electrons.[15]

Others have found that these effective constants can be related to their free electron counterparts in the following manner (in the case of linear recombination):[16]

$$\tau_n = \left(1 + \frac{\partial n_l}{\partial n}\right) \tau_0 \tag{3.9}$$

and

$$D_n = \left(1 + \frac{\partial n_l}{\partial n}\right)^{-1} D_0 \tag{3.10}$$

Inherent in the expressions above is the quasistatic approximation, which postulates that trapping processes are much faster than τ_0. The effective electron lifetime corresponds to the device response time after a small charge injection

event; the time constant for the decay is much slower than that expected from the free carrier lifetime. Thus the effective diffusion constant and electron lifetime incorporate the effect of trapping through the term $\frac{\partial n_l}{\partial n}$, for which an exponential distribution is commonly substituted.

Because the effective constants incorporate the trap distribution, they are not really constant after all. Since $\frac{\partial n_l}{\partial n}$ is dependent on n, there are power law dependences for D_n and τ_n on charge density. However, when we multiply together Equations 3.9 and 3.10, the dependence on trap density cancels, leaving a constant.[17] Thus, we can define a single diffusion length:

$$L_n = \sqrt{D_n \tau_n} = \sqrt{D_0 \tau_0} \tag{3.11}$$

This neatly explains an empirical fact frequently observed with some surprise: that the light intensity dependences of the effective electron lifetimes and diffusion coefficients compensate each other reasonably well.[18] The diffusion length does not require a prefatory "effective" qualifier because it is a steady-state property of the DSSC which does not depend on any trapping terms. In steady-state, trapped and free electrons achieve an equilibrium such that the product of lifetime and diffusion coefficient remains approximately constant. This insight will prove instrumental to our subsequent criticism of transient methods of estimating charge collection efficiency, which do in fact reflect trapping behavior.

However, this compensation effect is not perfect when recombination is nonlinear, and as a result it restricts the usefulness of a diffusion length concept to the open circuit condition, where the charge density is roughly constant throughout the film thickness. Elsewhere along the JV curve, and especially at short circuit, the charge density in the film differs by orders of magnitude due to a density gradient from which diffusive current arises.[11] If the effective diffusion coefficient and electron lifetime were to possess the exact same dependence on charge density, then we would in fact observe perfect compensation and an absolute diffusion length definable over the length of the device irrespective of any charge density gradient.

This is in fact an assumption in a model created by Anta and co-workers, a model which is more versatile than ours because it explicitly designates a sub-

stitutable density-dependence function, but more restrictive in that the same function must be used for recombination and transport behavior (indeed, the function they choose for their simulations corresponds exactly to the density dependence of our exponential density of states). [19] Later, they adjusted their model to include a nonlinear recombination term, corresponding to the b parameter in Equation 1.10. [11].

Barnes and O'Regan note that in practice, the deviations in diffusion length caused by nonlinear recombination are minor, contributing a 14% error in the case of $b = 0.6$. [12] They conclude that calculations of the diffusion length obtained by illuminating the solar cell from opposite sides (a method described in Chapter 4) and assuming linear recombination are reasonably accurate because while the diffusion length is defined on a point-by-point basis when the charge density is not constant, the average over the device thickness tends to approximate the prediction from linear recombination. While this may be the case, it is still conceptually misleading to define a diffusion length for the case of nonlinear recombination.

Although the diffusion length and its closely related cousin, the collection efficiency, are steady-state parameters of the DSSC, that does not mean that steady state measurements will suffice to characterize these devices.[20] On the contrary, as noted earlier, the trapping phenomena of DSSCs are integrally important to understanding device operation and are obscured by steady state measurements. The following discussion will present a novel method of rewriting the governing equations to more insightfully handle transient processes.

3.2 Nondimensionalizing the governing equation

Building on the conceptual framework introduced above, this thesis seeks to bridge the gap between DSSC modelling and experiment. The dimensional governing equation, Equation 1.10, is difficult to use as an experimental tool to, for example, iteratively improve some parameter like the free electron diffusion coefficient, D_0. It requires extensive knowledge of material parameters of the TiO_2, such as the dark population of trapped electrons, N_{l0}, the dark population of conduction band electrons, N_0, and the free electron lifetime, τ_0. These numbers

are very difficult to ascertain with accuracy and precision and are often estimated with significant uncertainty.[21]

Nondimensionalization allows us, through appropriate substitutions, to eliminate material parameters and simplify the form of the equation. For example, the trap density of states expression, Equation 3.5, was unwieldy enough to obscure any insight derivable from the form of Equation 1.10. Lastly, nondimensionalization allows us to rewrite the equation with parameters that correspond to important, meaningful quantities that we have discussed earlier.

Therefore, we make the following substitutions:

$$\bar{n}N_0(\frac{G\tau_0}{N_0})^{1/b} = n \tag{3.12a}$$

$$\bar{x}L = x \tag{3.12b}$$

$$\bar{V} = \frac{V}{mkT} \tag{3.12c}$$

$$\bar{t} = t\tau_0\frac{N_{l0}}{N_0}m\beta(\frac{G\tau_0}{N_0})^{m\beta/b-1} \tag{3.12d}$$

Using these substitutions, Equation 1.10 becomes

$$\frac{\partial\bar{n}}{\partial\bar{t}}\bar{n}^{m\beta-1} = \exp(-\bar{x}\alpha) - \bar{n}^b + \lambda^2\frac{\partial^2\bar{n}}{\partial\bar{x}^2} \tag{3.13}$$

with boundary conditions:

$$\bar{n}|_{\bar{x}=0} = \nu \tag{3.14a}$$

$$\frac{\partial\bar{n}}{\partial\bar{x}}|_{\bar{x}=1} = 0 \tag{3.14b}$$

The non-dimensional problem now depends on just five numbers. $m\beta$ and b have the same meaning as in the dimensional equations. The other non-dimensional parameters are the absorption coefficient α, effective recombination/diffusion length λ, and charge density on the boundary ν. These parameters are related to the dimensional parameters by the following relations:

$$\alpha = \frac{L}{x_\alpha} \tag{3.15a}$$

$$\lambda = \frac{1}{L}\sqrt{(D\tau_0(\frac{G\tau_0}{N_0})^{1/b-1})} \tag{3.15b}$$

$$\nu = (\frac{G\tau_0}{N_0})^{-1/b}\exp(V/mkT) \tag{3.15c}$$

The new governing equation is far simpler and has also lost its dependence on inaccessible material parameters. Moreover, the (nondimensional) diffusion length makes an appearance in the governing equation itself, highlighting its important role in device performance. There is no obvious term corresponding to the incident light intensity, but its influence is in fact ensconced in the definitions of the newly defined λ and ν terms. Indeed, the nature of nonlinearity in recombination has an interesting effect on the nondimensional diffusion length, λ, which is constant under linear recombination, as discussed earlier, but is positively related to light intensity under superlinear recombination and is negatively related under sublinear recombination. This makes intuitive sense—b, the recombination exponent, basically expresses whether recombination lags, keeps up with, or outpaces increases in the effective diffusion coefficient as the charge density increases. The other two parameters carry meaning as well: α is the nondimensional absorption length, and ν is related to the open circuit voltage. Later, by studying a simplified case, we will see an explicit form of this relationship.

An important point here is that, excluding gains in simplicity, we have not gotten something for nothing. If we fit the five nondimensional parameters above to a real device, we cannot hope for our simulation to output any value with units; thus, we cannot plot a JV characteristic with real values. This seems to defeat the purpose of a modeling methodology from a conventional solar cell research perspective which prizes steady state JV measurements for effective characterization. But recall that the differentiating trait of the DSSC is its transient behavior, and understanding that is mostly accomplished by appeal to decay rates, the unitless ratios and power law dependences of which we can in fact expect to extract from a nondimensional simulation.

3.3 Steady-state Behavior[1]

To build intuition about the behavior of Equation 3.13 in the steady state, we first make some simplifying assumptions that allow us to explicitly write analytical expressions for various quantities of interest. We will then remove the simplications to reveal that the analytical starting point is in fact reasonably reflective of the general device behavior.

3.3.1 Simplified case: $\alpha = 0$, $b = 1$

This case corresponds to a device which absorbs light uniformly throughout the film thickness and exhibits ideal, linear recombination. The steady-state solution to Equation 3.13 can here be explicitly expressed as:

$$\bar{n} = 1 - (1 - \nu)\left(\cosh\left(\frac{x}{\lambda}\right) - \sinh\left(\frac{x}{\lambda}\right)\tanh\left(\frac{1}{\lambda}\right)\right) \tag{3.16}$$

This allows us to explicitly express the charge density at the boundary, ν, necessary to achieve open circuit. At steady state and at open circuit, the charge density throughout the film is constant (because we have set α to zero), so we just solve $\frac{d\bar{n}}{d\bar{x}}|_{x=0} = 0$. This occurs when $\bar{n} = \nu = 1$, and the open circuit voltage obeys:

$$\bar{V}_{OC} = \frac{1}{b} log\left(\frac{G\tau_0}{N_0}\right) \tag{3.17}$$

Recalling the definition of the nondimensional open circuit voltage, the expression above is consistent with an ideality factor of $\frac{m}{b}$, provided that the generation rate and light intensity are proportional.

We can now observe the relationship between the open circuit voltage and the parameter ν by calculating its value at short circuit. In this condition, $\bar{V} = 0$, and the charge density on the left hand boundary is very small: $\nu = exp(-\bar{V}_{OC})$. We can average the charge density over the device thickness to determine its average value at short circuit:

[1]The figures and expressions related to modeling of the DSSC presented here arose from collaboration with James Kirkpatrick, who mentored V.S. in mathematical derivation

$$\langle \bar{n} \rangle = \int_0^1 \bar{n} \, \mathrm{d}\bar{x} = 1 - \lambda \tanh\left(\frac{1}{\lambda}\right) \tag{3.18}$$

This means that for recombination lengths greater than 1, the average charge density at short circuit goes as $\frac{1}{2\lambda^2}$. When the recombination length is very short, the average charge density is closer to that at open circuit. The intuitive explanation here is that the shorter the recombination length, the closer to the working electrode charges must be generated to be collected. Thus, much of the length of the device operates as if it were at open circuit, since the electrons generated closer to the counterelectrode recombine very quickly and thus do not contribute to the diffusive gradient that characterizes the entire length of an efficiently collecting device.[22] Note that the values of the nondimensional charge density are normalized for the electron lifetime; thus, it is not particularly instructive to compare them between devices with different recombination lengths. Figure 3.1 illustrates the difference in charge density profile for devices with low and high values of λ.

3.3.2 Comparison with general case

When we relax the assumption that $b = 1$, the average value of charge density at short circuit derived above retains approximate usefulness because it reasonably approximates nonlinear recombination. From Figure 3.1, we can see that only extreme values of b cause the charge density profile to deviate considerably from the profile at $b = 1$. Upon averaging the short circuit charge density, we recognize that the deviation is relatively minor for devices exhibiting nonlinear recombination, evident from Figure 3.2.

This is an important fact because the $b = 1$ approximation allowed us to write down analytical expressions building intuition for the nondimensional quantities introuced in this thesis, and this intuition should hopefully carry over to the general case. The relaxation of the $\alpha = 0$ assumption similarly does not change affairs much; strictly speaking, the charge density at open circuit is no longer constant, but it is very close to invariant, and the short circuit average charge density is reasonably independent of the value of b for any controlled value of α.

Later, when we analyze transient decays, the applicability of analytical expres-

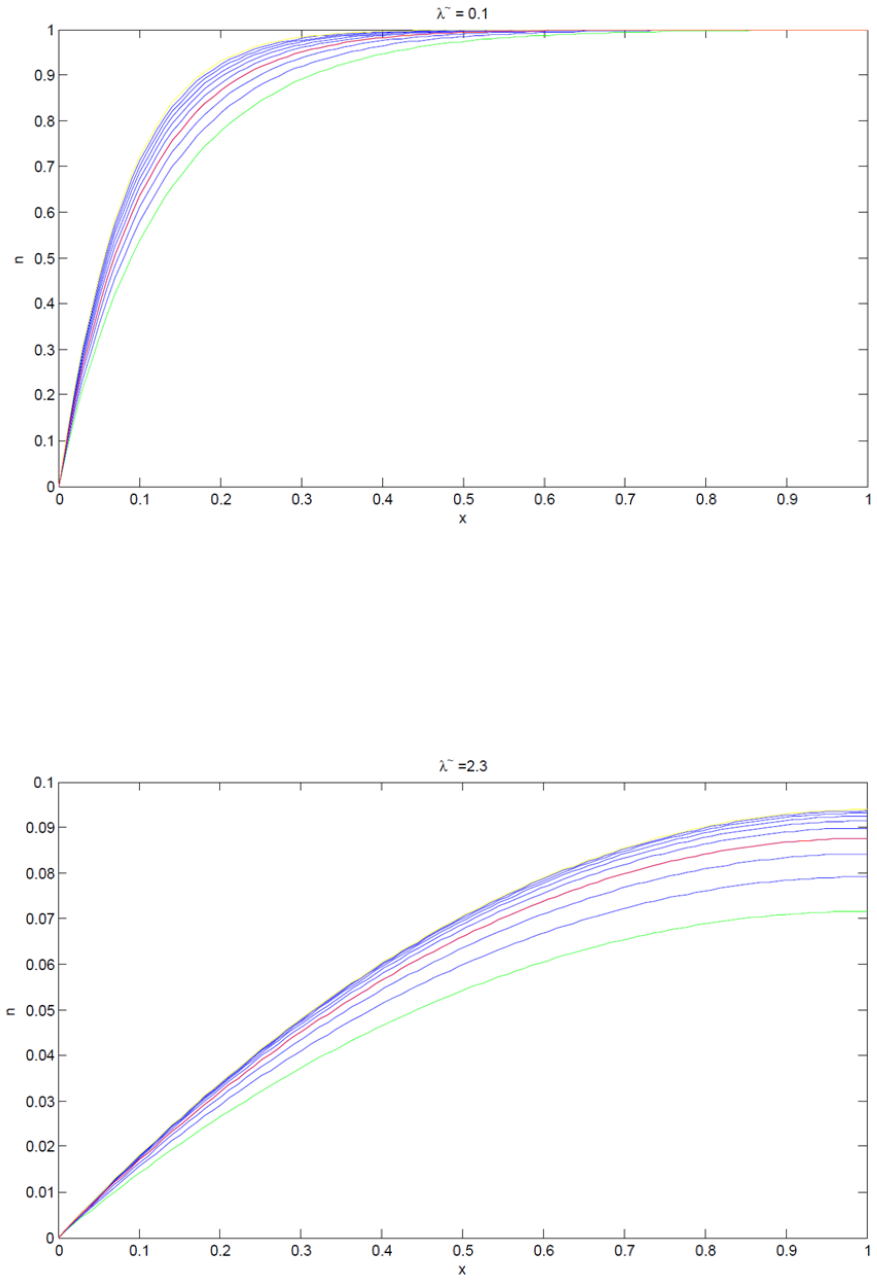

Figure 3.1: Plots of the nondimensional charge densities for [top panel] $\lambda = 0.1$ and [bottom panel] $\lambda = 2.3$. For each plot, the value of b was varied from 0.5 (green curve) to 2 (yellow curve), and the curve when $b = 1$ is shown in red.

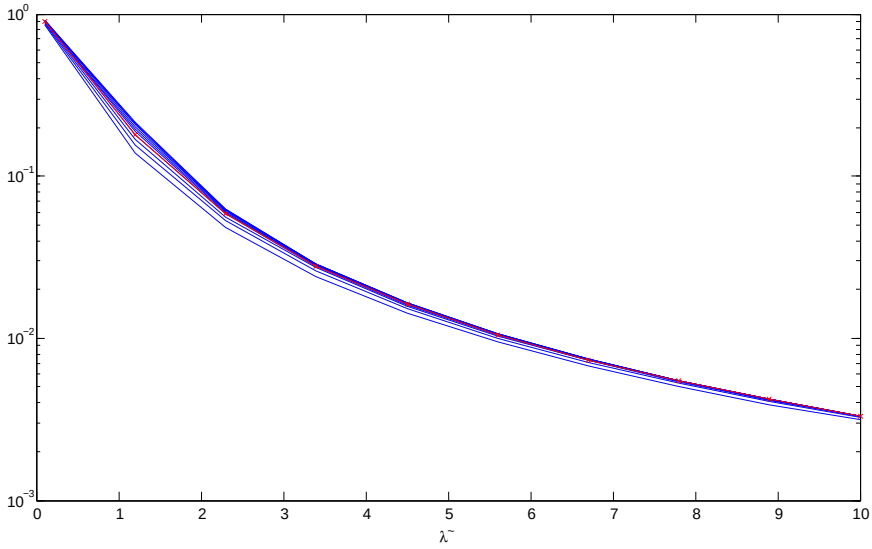

Figure 3.2: Plot of the average charge density at short circuit vs the nondimensional recombination length, λ. The value of b has been varied from 0.5 to 1 to generate the various curves, and the red curve corresponds to the case where $b = 1$.

sions based on the average short circuit current density despite the relaxation of certain assumptions will prove crucial in adapting this abstract, nondimensional modeling framework into a useful experimental tool for evaluating real devices.

3.3.3 Extracting Steady State Properties

Recall that by nondimensionalizing the governing equations, we did lose real information and cannot reproduce the actual values in a currect-voltage characteristic. While this may be true, we can still produce a nondimensional JV curve, and indeed simulations of nondimensional currents and voltages will prove key to extracting nondimensional parameters like decay rates in transient analysis.

Figure 3.3 illustrates the correspondence between charge density profiles and points on the JV curve. The two most salient insights are (a) that the charge density increases overall as we approach open circuit, because fewer charges are being extracted, and (b) the gradient at the working electrode increases as the current increases, reflective of the fact that the current is proportional to the derivative of charge density on the left hand boundary.[23]

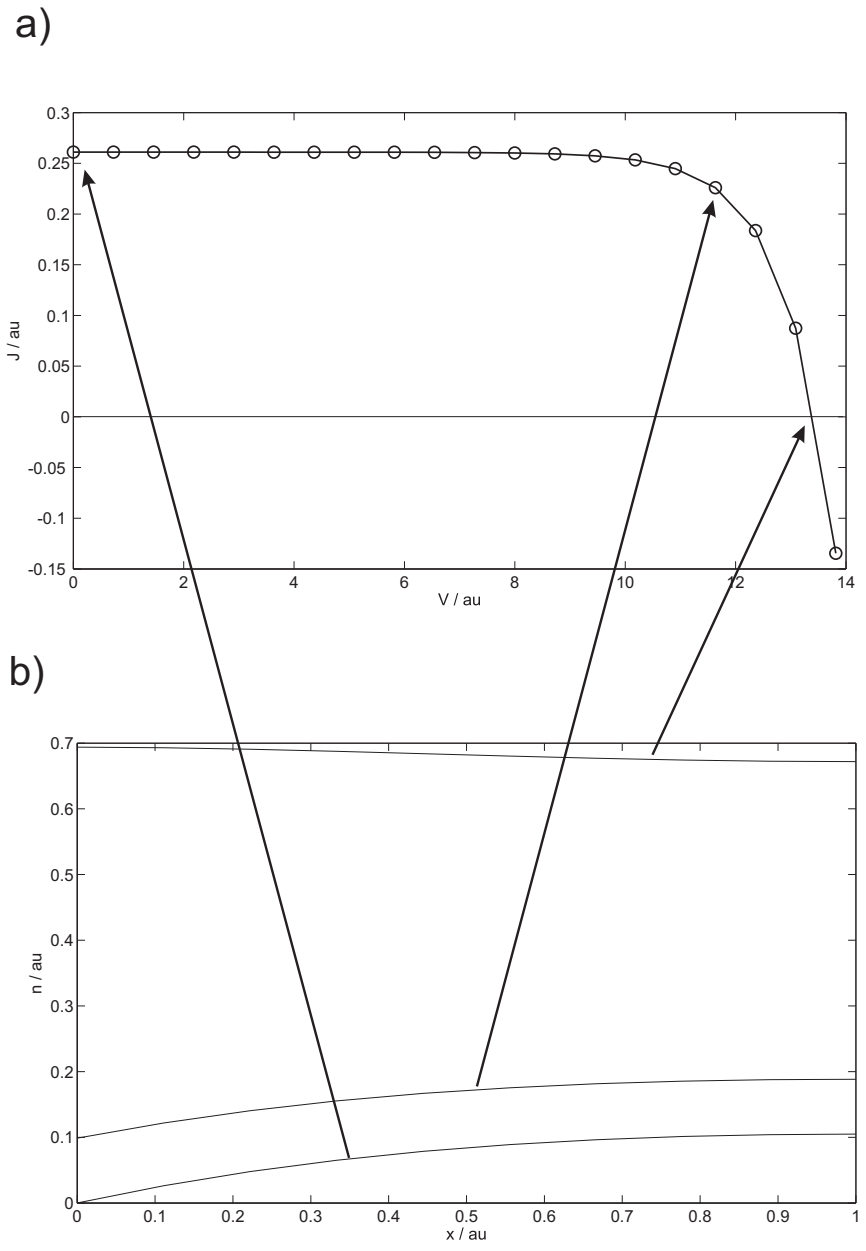

Figure 3.3: Plots of (a) the JV curve in nondimensional units and (b) the associated charge density profiles. Note that the nondimensional current is merely proportional to $\frac{d\bar{n}}{d\bar{x}}|_{x=0}$ and the voltage to $log(\bar{n})$.

While the nondimensional Equation 3.13 does not contain enough information to generate a dimensional JV curve, it can obtain the collection efficiency of a device, a nondimensional parameter. The collection efficiency of a DSSC is simply the ratio of electrons collected at the working electrode to those injected into the semiconductor.[24] We can easily express it as:

$$\eta_c = \frac{D\frac{\partial n}{\partial x}|_{x=0}}{\int_0^L G\exp(-x'/x_\alpha)dx'} = \frac{\alpha\lambda^2}{1-\exp(-\alpha)}\frac{\partial \bar{n}}{\partial \bar{x}}|_{\bar{x}=0} \tag{3.19}$$

We will use Equation 3.19 to extract the collection efficiency from MATLAB simulations performed in Chapter 4.

3.4 Conclusion

In this Chapter, we introduced the generally accepted modeling framework used in the DSSC research community and advanced it by presenting a nondimensionalized version of the governing equation, Equation 3.13. After analysis of the existing literature on the origin of the photovoltage and the nature of the diffusion length, we chose to incorporate nonlinear recombination, exponential trap state distribution, and a framework that deals with free electrons pursuant to the quasistatic approximation. This will allow use of the model, for example in Chapter 4, to account for phenomena observed in DSSCs that are not explainable with simpler modeling constructs, like a diffusion length that actually is not constant under changing light intensity.

However, we do shed unnecessary elements of existing models which make iterative experimentation and simulation very difficult. The nondimensional model introduced here has only five parameters, compared to nine in a similarly versatile dimensional model. In Chapter 4, we will introduce a protocol for fitting those five parameters from experimental measurements of real solar cells and apply the model to treat transient behavior.

3.5 References

[1] Jrg Ferber and Joachim Luther. Modeling of photovoltage and photocurrent in dye-sensitized titanium dioxide solar cells. *The Journal of Physical Chemistry B*, 105(21):4895–4903, 2001. 47

[2] Laurence Peter. Sticky transport and interfacial transfer of electrons in the dye-sensitized solar cell. *Acc. Chem. Res.*, 42(11):1839–1847, July 2009. 47

[3] Juan Bisquert and Vyacheslav S. Vikhrenko. Interpretation of the time constants measured by kinetic techniques in nanostructured semiconductor electrodes and dye-sensitized solar cells. *The Journal of Physical Chemistry B*, 108(7):2313–2322, 2004. 47

[4] M. Bailes, P. J. Cameron, K. Lobato, and L. M. Peter. Determination of the density and energetic distribution of electron traps in dye-sensitized nanocrystalline solar cells. *The Journal of Physical Chemistry B*, 109(32):15429–15435, 2005. 47

[5] Klaus Schwarzburg and Frank Willig. Origin of photovoltage and photocurrent in the nanoporous dye-sensitized electrochemical solar cell. *The Journal of Physical Chemistry B*, 103(28):5743–5746, 1999. 48

[6] Henry J. Snaith. Estimating the maximum attainable efficiency in dye-sensitized solar cells. *Advanced Functional Materials*, 20(1):13–19, 2010. 48

[7] R.F. Pierret. *Advanced semiconductor fundamentals*. Modular series on solid state devices. Addison-Wesley Pub. Co., 1987. 49

[8] Petra J. Cameron, Laurence M. Peter, and Sarmimala Hore. How important is the back reaction of electrons via the substrate in dye-sensitized nanocrystalline solar cells? *The Journal of Physical Chemistry B*, 109(2):930–936, 2005. 49

[9] L. M. Peter. Characterization and modeling of dye-sensitized solar cells. *The Journal of Physical Chemistry C*, 111(18):6601–6612, 2007. 49

[10] N.-G. Park, J. van de Lagemaat, and A. J. Frank. Comparison of dye-sensitized rutile- and anatase-based TiO2 solar cells. *The Journal of Physical Chemistry B*, 104(38):8989–8994, 2000. 49

[11] J. Villanueva-Cab, G. Oskam, and J.A. Anta. A simple numerical model for the charge transport and recombination properties of dye-sensitized solar cells: A comparison of transport-limited and transfer-limited recombination. *Solar Energy Materials and Solar Cells*, 94(1):45 – 50, 2010. 17th International Materials Research Congress 2008. 49, 51, 52

[12] Piers R. F. Barnes and Brian C. O'Regan. Electron recombination kinetics and the analysis of collection efficiency and diffusion length measurements in dye sensitized solar cells. *The Journal of Physical Chemistry C*, 114(44):19134–19140, 2010. 49, 52

[13] Sven Soedergren, Anders Hagfeldt, Joergen Olsson, and Sten-Eric Lindquist. Theoretical models for the action spectrum and the current-voltage characteristics of microporous semiconductor films in photoelectrochemical cells. *The Journal of Physical Chemistry*, 98(21):5552–5556, 1994. 50

[14] Jenny Nelson and Rosemary E. Chandler. Random walk models of charge transfer and transport in dye sensitized systems. *Coordination Chemistry Reviews*, 248(13/14):1181 – 1194, 2004. 50

[15] P. J. Cameron and L. M. Peter. How does back-reaction at the conducting glass substrate influence the dynamic photovoltage response of nanocrystalline dye-sensitized solar cells? *The Journal of Physical Chemistry B*, 109(15):7392–7398, 2005. 50

[16] Arie Zaban, Miri Greenshtein, and Juan Bisquert. Determination of the electron lifetime in nanocrystalline dye solar cells by open-circuit voltage decay measurements. *ChemPhysChem*, 4(8):859–864, 2003. 50

[17] Juan Bisquert, David Cahen, Gary Hodes, Sven Rahle, and Arie Zaban. Physical chemical principles of photovoltaic conversion with nanoparticulate, mesoporous dye-sensitized solar cells. *The Journal of Physical Chemistry B*, 108(24):8106–8118, 2004. 51

[18] S. Nakade, Y. Saito, W. Kubo, T. Kitamura, Y. Wada, and S. Yanagida. Influence of TiO2 nanoparticle size on electron diffusion and recombination in dye-sensitized TiO2 solar cells. *J. Phys. Chem. B*, 107(33):8607–8611, July 2003. 51

[19] Juan A. Anta, Fabiola Casanueva, and Gerko Oskam. A numerical model for charge transport and recombination in dye-sensitized solar cells. *J. Phys. Chem. B*, 110(11):5372–5378, March 2006. 52

[20] Juan Bisquert. Chemical capacitance of nanostructured semiconductors: its origin and significance for nanocomposite solar cells. *Phys. Chem. Chem. Phys.*, 5:5360–5364, 2003. 52

[21] Mara Quintana, Tomas Edvinsson, Anders Hagfeldt, and Gerrit Boschloo. Comparison of dye-sensitized ZnO and TiO2 solar cells: Studies of charge transport and carrier lifetime. *The Journal of Physical Chemistry C*, 111(2):1035–1041, 2007. 53

[22] Brian C. O'Regan and Frank Lenzmann. Charge transport and recombination in a nanoscale interpenetrating network of n-type and p-type semiconductors: Transient photocurrent and photovoltage studies of TiO2/Dye/CuSCN photovoltaic cells. *J. Phys. Chem. B*, 108(14):4342–4350, March 2004. 56

[23] Jrg Ferber, Rolf Stangl, and Joachim Luther. An electrical model of the dye-sensitized solar cell. *Solar Energy Materials and Solar Cells*, 53(1/2):29 – 54, 1998. 58

[24] Michael Gratzel. Solar energy conversion by dye-sensitized photovoltaic cells. *Inorganic Chemistry*, 44(20):6841–6851, 2005. PMID: 16180840. 60

Chapter 4

Assessing the Accuracy of Charge Collection Efficiency Obtained from Transient Perturbation Methods

4.1 Introduction

When optimizing the DSSC, a complex electronic system as we have seen in earlier chapters, it is easy to lose the forest in the trees.[1] Our investigation of the multiple trapping diffusion that appears to characterize DSSCs revealed many intertwined electronic processes and parameters, and focusing on any one of these threatens to obscure the ultimate goal of improving cell performance through an ideal balance of transport and recombination.[2] For example, as we will see later, a focus on improving the speed of electron transport has spawned a broad set of novel nanostructures; many of these materials, like the nanowires discussed in the next chapter, hold great promise for improving cell performance, but increasing the rate of electron transport is not a useful end in itself.[3] Iteratively modifying the trap state distribution, the electron lifetime, or the electronic mobility can only succeed if a simple, fast measurement is available that summarizes the aggregate effect of the component subprocesses.

Such a summary metric, the collection efficiency of photoinjected electrons, can be conveniently estimated using transient optical perturbation methods (equivalently: small perturbation or transient perturbation methods) at short circuit.[4] Use of the technique is prevalent in the field of DSSCs, even though a thorough investigation of its accuracy has not been performed. In this chapter, we will critique the accuracy of small perturbation methods at short circuit for exhibiting high volatility as well as inherently misapprehending the nature of the collection efficiency, a steady state parameter. However, pleasingly, it will turn out that we can unify the measurement methodology by suggesting the use of steady state techniques to determine the collection efficiency in most cases and turning to small perturbation, transient measurements for the others. We proceed by applying the nondimensional modelling framework developed in Chapter 3 and then applying simulation and experimental techniques to empirically assess small perturbation transient techniques.

4.2 Description of Conventional Measurement Techniques

The small perturbation measurement of collection efficiency monitors current and voltage decays, following a small perturbation light pulse, to measure the rates at which photogenerated electrons leave the conduction band either through recombination or collection at the anode. Normally, the cell is held at short circuit, irradiated by a background intensity of white light, and a small red pulse is administered to generate an additional amount of charge uniformly in the cell.[5] To extract the charge collection efficiency, two decay rates are measured after the light pulse:

(a) Current (J_{SC}) Decay: the cell is held at zero voltage, the transient current decay, $\propto exp(-\kappa_J t)$, is monitored, and κ_J is extracted.

(b) Voltage (V_{SC}) Decay: the cell is held at constant current at short circuit, the transient voltage decay, $\propto exp(-\kappa_V t)$, is monitored, and κ_V is extracted.

Since at constant current, the additional photogenerated electrons can only leave the solar cell via recombination, the recombination lifetime is usually equated

to the voltage decay constant: $\kappa_{Rec} = \kappa_V$.[6] At constant voltage, extra electrons can leave the cell either through recombination or collection; the extraction decay constant (κ_{Trans}) for electrons leaving the cell via collection is thus calculated as: $\kappa_{Trans} = \kappa_J - \kappa_{Rec}$. Finally, the collection efficiency is approximated as:

$$\eta_c \approx \eta_{approx} = \frac{\kappa_{Trans}}{\kappa_J} \tag{4.1}$$

O'Regan et al. pioneered the use of voltage decays at short circuit to extract recombination rates at the same charge density profile as current decays. The experimental setup was carefully calibrated to keep peak voltage transients low (below 10mV), and the decay rate was compared to a simultaneous transient absorbtion measurement to determine if the voltage decay accurately reflected the recombination rate at short circuit.[4] They discovered that indeed the transient photovoltage decay matched the trace of the transient absorption at 980nm, indexed to conduction band electrons in the TiO_2. [7] However, there was no further investigation of whether this decay rate, inserted into Equation 4.1, yields an accurate charge collection efficiency. Indeed, as we will contend in this chapter, the decay of conduction band electrons following a small perturbation includes equilibration between free and trapped electron populations; conversely at steady state, the collection efficiency is not affected by such processes because the system is already at equilibrium. Moreover, while O'Regan et al. were careful to limit the size of their voltage perturbation, the effect of relaxing this precaution has not been studied and in fact an acceptable threshold perturbation has not been established for a technique with such wide use.

Recently, transient perturbation methods have been increasingly criticized, though the magnitude of errors remains unresolved.[8] Some report that the related technique of monitoring the transient open circuit voltage decay constant overestimates the electron diffusion length [9; 10] The inaccuracy was subsequently shown to arise from nonlinearity in recombination rate with increasing charge density, which we treated in Chapter 3.[11; 12] While DSSCs infiltrated with liquid electrolyte may exhibit sublinear recombination, the solid state devices fabricated in this chapter exhibit linear or superlinear recombination rates, yet inaccuracies in η_{approx} persist. Thus, the existence of the nonlinear recom-

bination parameter, b, is not sufficient to explain inaccuracies in translating a transient decay rate into a steady state parameter like the diffusion length or the collection efficiency.

Another method for measuring the competition between electron collection and recombination has emerged recently and involves illuminating the solar cell from both sides and computing a ratio of external quantum efficiencies (EQE).[10] The method entails further optical measurements which, when combined with the EQE measurement, allow an estimation of the diffusion length and the charge injection efficiency from the dye. Subsequently, by taking the ratio of EQE from top and bottom illumination, the injection efficiency term and any instrument calibration errors cancel, theoretically enabling an accurate estimate of the diffusion length. This method does rely on the (incorrect) assumption of linear recombination, but the authors maintain the assumption causes minimal errors.[12] Larger errors occur, they concede, when the diffusion length, L_n, is much greater than the device thickness, L; i.e., $L_n \geq 2L$.

We argue that this is approximately the lower boundary for accurate charge collection efficiencies extracted from transient perturbation, thus providing a neat switch-over point between steady-state and transient regimes of measurement. The reason is that the transient processes which affect small perturbation measurements have negligible effect on estimation of steady state parameters for devices which efficiently collecting charge. Following efforts elsewhere to unify electronic measurements using impedance spectroscopy and intensity-modulated photocurrent/photovoltage (IMPS/IMVS) AC response methods,[13] we aim to similarly unify EQE and transient decay techniques for ascertaining the collection efficiency, specifying the regimes under which each method is appropriate. Thus, steady state techniques are accurate for devices exhibiting low collection efficiencies while small perturbation measurements, as we will endeavor to demonstrate, are accurate only for devices endowed with high collection efficiencies.

4.3 Simulating Transient Decays at Short Circuit

We begin by applying the nondimensional model developed in Chapter 3 to treat the transient decays of current and voltage at short circuit introduced in the section above. The basic assumptions behind the transient perturbation are that the light absoption is uniform over the device thickness and the increase in charge density small enough to change Equation 3.13 from nonlinear to linear in charge density.[14]

4.3.1 Linearization of the Governing Equation Under Small Perturbations

The nonlinearity inherent in Equation 3.13 makes analytical treatment of time dependence difficult. However, with simplifying assumptions that can be met by carefully designed experiments, we can linearize small perturbation time dependent problems. Explicitly, we can write the following expression for the charge density following a small perturbation:

$$\bar{n}(\bar{t}=0) = \bar{n}_0 + \epsilon \bar{n}_{initial} \tag{4.2}$$

where $\bar{n}_0$ is the steady state charge density prior to the perturbation and $\bar{n}_{initial}$ is on the same order of magnitude as $\bar{n}_0$. Our assumption, when we call the perturbation small, is that ϵ is a small enough parameter to write the following expansion for the charge density in Equation 3.13:

$$\bar{n} = \bar{n}_0 + \epsilon \bar{n}_1 + O(\epsilon^2) \tag{4.3}$$

By executing this substitution and discarding terms higher than first order in ϵ, we obtain the following linear partial differential equation describing the time evolution of the marginal charge density generated by the small perturbation:

$$\frac{\partial \bar{n}_1}{\partial \bar{t}} \approx -b\bar{n}_0^{b-m\beta}\bar{n}_1 + \lambda^2 \bar{n}_0^{1-m\beta}\frac{\partial^2 \bar{n}_1}{\partial \bar{x}^2} \tag{4.4}$$

with boundary conditions:

$$\bar{n}_1|_{\bar{t}=0} = \bar{n}_{initial} \tag{4.5a}$$

$$\frac{\partial \bar{n}_1}{\partial \bar{x}}|_{\bar{x}=1} = 0 \tag{4.5b}$$

$$\frac{\partial \bar{n}_1}{\partial \bar{x}}|_{\bar{x}=0} = 0 \quad \text{OR} \tag{4.5c}$$

$$\bar{n}_1|_{\bar{x}=0} = 0 \tag{4.5d}$$

Depending on the electrical condition under which the solar cell is held during the perturbation, either Equation 4.5c (voltage decay) or Equation 4.5d (current decay) will apply as the boundary condition.

This is illustrated by Figure 4.1, which displays the charge density profile in the film before and instantaneously after transient perturbations at short circuit. The short circuit diffusion current, by Fick's Law, is proportional to the slope of charge density at the collecting electrode, and the measured voltage during the perturbation is proportional to the logarithm of charge density at the collecting electrode.

4.3.2 Analytical Approximation: $\bar{n}_0 \rightarrow \langle \bar{n}_0 \rangle$

To continue in an analytical fashion, we make an approximation commonly used in the literature that the background charge density is invariant across the device thickness.[15] Prima facie, this is a bad assumption; as evident from the charge density profile at short circuit presented earlier, the charge density is clearly not spatially invariant. However, recall that to build intuition about the nondimensional model parameters in Chapter 3, we made assumptions about b and α and later demonstrated that analytical expressions reasonably described the average charge density, $\langle \bar{n} \rangle$, even after these assumptions were relaxed. This motivates us to explore $\langle \bar{n}_0 \rangle$, the average background charge density, through analytical expressions to see if its small perturbation behavior can offer insight into device operation.

Now, we can solve Equation 4.4 by decomposing the marginal charge density, $\bar{n}_1$ into a summation of exponentially decaying spatial eigenfunctions. For

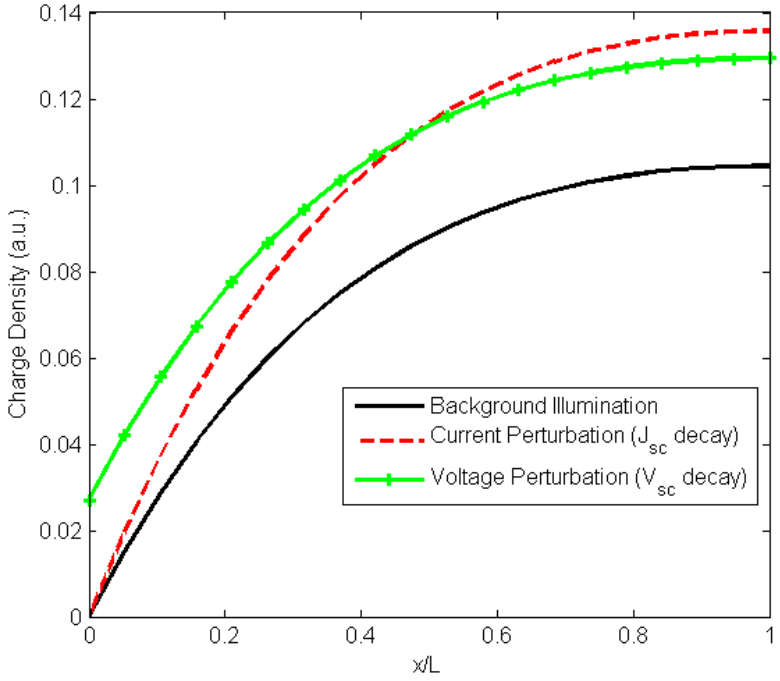

Figure 4.1: Illustration of charge density profiles before and after perturbations. Transient excitation has been exaggerated for ease of distinguishing curves. Note that the voltage perturbation holds $\frac{\partial \bar{n}}{\partial \bar{x}}|_{\bar{x}=1}$ constant and the current perturbation holds $\bar{n}|_{\bar{x}=0}$ constant

illustration, we will consider the full solution of the photocurrent decay case (see Appendix 2 for derivation). The eigenfunctions for the photocurrent decay look like:

$$\lambda_i(\bar{x},\bar{t}) = c_i \sin\left(x\frac{(2i+1)\pi}{2}\right)\exp\left(-\bar{\kappa^J}_i\bar{t}\right) \tag{4.6}$$

with the rate constant:

$$\bar{\kappa^J}_i = \langle\bar{n}_0\rangle^{1-m\beta}\left(\lambda^2(2i+1)^2\frac{\pi^2}{4} + b\,\langle\bar{n}_0\rangle^{b-1}\right) \tag{4.7}$$

The normalized coefficients depend on the initial charge density profile. If we use the following shorthand:

$$\chi_i(\bar{x}) = \sin\left(x\frac{(2i+1)\pi}{2}\right) \tag{4.8}$$

then we can explicitly write the coefficients c_i as:

$$\frac{\int_0^1 \chi_i \bar{n}_{initial}\,\mathrm{d}\bar{x}}{\int_0^1 \chi_i^2\,\mathrm{d}\bar{x}} \tag{4.9}$$

The full form of the coefficients and eigenfunctions were given above for completeness, but in practice we actually are not concerned with the higher eigenfunctions or their relative amplitudes. Rather, we care about the lowest eigenfunction, whose decay constant is slowest and thus causes it to dominate the long-term decay. Qualitatively, this means that the first part of the decay is characterized by a redistribution of charge, followed by a monoexponential decay (this explains characterizations elsewhere of a "biexponential decay" [16]); a sample decay is provided in Chapter 2 to illustrate the fitting protocol used throughout this thesis, whereby we only fit the monoexponential segment of the decay after the highest eigenfunctions have decayed.

Therefore, we only include the expression for the lowest voltage eigenfunction, which turns out to be a constant function in space:

$$\mu_0(\bar{x},\bar{t}) = c_0 exp(-\bar{\kappa}_0^V \bar{t}) \tag{4.10}$$

where the rate constant is:

$$\bar{\kappa}_0^V \bar{t} = b\langle\bar{n}_0\rangle^{b-m\beta} \tag{4.11}$$

Thus we can rewrite the zero-order long-term current decay rate as:

$$\bar{\kappa_0^J} = \langle\bar{n}_0\rangle^{1-m\beta}\left(\lambda^2\frac{\pi^2}{4}\right) + \bar{\kappa}_0^V \tag{4.12}$$

Redimensionalizing Equations 4.11 and 4.12 yields:

$$\kappa_0^V = \frac{N_0^{1-b+m\beta}}{N_{l0}}\frac{b}{m\beta}\langle n_0\rangle^{b-m\beta}\frac{1}{\tau_0} \tag{4.13}$$

$$\kappa_0^J = \frac{N_0^{m\beta}}{N_{l0}} \frac{1}{m\beta} \langle n_0 \rangle^{1-m\beta} \frac{\pi^2}{4} \frac{D}{L^2} + \kappa_0^V \tag{4.14}$$

These power laws for the dependence of the decay rate on charge density match those found by Barnes et al. via a different derivation. [17]

We include the dimensional expressions above to illustrate the complexity inherent in interpreting decay rates, simplistic conventions notwithstanding. The photovoltage decay depends on recombination via the electron lifetime, τ_0, while the photocurrent decay depends on electron transport via the term $\frac{D}{L^2}$. Also, recall the factor 2.47 in Equation 1.9 (reprinted here):

$$D_n = \frac{L^2}{2.47\tau_{trans}} \tag{1.9}$$

This commonly used approximation (which uses the reciprocal of the transport decay constant defined earlier in Equation 4.1) stems directly from the $\frac{\pi^2}{4}$ in Equation 4.14. As an aside, more involved and precise calculations undertaken by Anta et al. culminate in a revision of the 2.47 figure to 2.77.[18] Regardless, from the preceding discussion and that in Chapter 3, Equation 1.9 clearly does not hold in general, and modifying the constant retains the same inadequate level of simplicity of the expression, dependent on a very specific set of device parameters that does not hold across constituent materials or fabrication processes. The free electron diffusion coefficient, D, is difficult to extricate from the thicket of constants in Equation 4.14. Still, it is promising that Equation 4.14 is exactly of the form $D_n = \frac{\partial n}{\partial n_L} D_0 = \frac{L^2}{2.47\tau_{Trans}}$, suggesting that the current decay rate neatly expresses the effective diffusion constant; however, recall that this relation only holds if $b = 1$. Equation 4.14 does not express the general relation between the effective and free diffusion constant because we have replaced n_0 with $\langle n_0 \rangle$.

Indeed, the alert critic will interject at this point that we still are dealing with the unreasonable approximation (at short circuit) that the background charge density is spatially invariant by considering the relevant variable of interest to be the average charge density. Thus we proceed to compare this assumption to simulation results where we consider the real charge density profile.

4.3.3 Fitting Real Device Parameters

To determine the values of the five parameters in the nondimensionalized governing Equation 3.13 and its Boundary Conditions 3.14 for a real device, we need to determine the relationship between experimental methods and nondimensional parameters.

It turns out that using analytical expressions for decay rates based on the average charge density, $\langle \bar{n}_0 \rangle$, does in fact offer useful insight for real device parameter fitting. To move past analytical approximations, we employ a MATLAB simulation to solve the linear partial differential Equation 4.4 for an arbitrary background charge density (more details on the simulation methodology are given later in the Results section). Specifically, we choose to hold the cell at short circuit under background illumination and then apply a uniform perturbation—the resulting decay rates are illustrated in Figure 4.2. We compare the decay rates calculated through the analytical expressions employing $\langle \bar{n}_0 \rangle$ to the decay rates from the full simulation of the decay.

Importantly, the perturbation intensity is kept fairly low in the simulation, <1% of the background light intensity, to ensure that the assumptions we made to derive Equation 4.4 in the first place are met, i.e., that $\bar{n}_{initial}$ is small enough compared to $\bar{n}_0$ that we can drop terms higher than first order.

From Figure 4.2, we can see clearly that the absolute values of the decay rates do not match between the analytical and simulated values. However, the power law dependence on light intensity does carry over (in order to arrive at this conclusion, we assume that generation is proportional to light intensity, whch others in the literature similarly assume by choosing a constant injection efficiency [19]). This means that we can extract the nondimensional parameters b and $m\beta$ from the slopes of the decay rates against light intensity. Recalling that $\kappa_{trans} = \kappa_J - \kappa_V$:

$$m\beta = 1 - \frac{\partial \log(\kappa_{trans})}{\partial \log(\Phi)} \tag{4.15}$$

$$b = m\beta + \frac{\partial \log(\kappa_V)}{\partial \log(\Phi)} \tag{4.16}$$

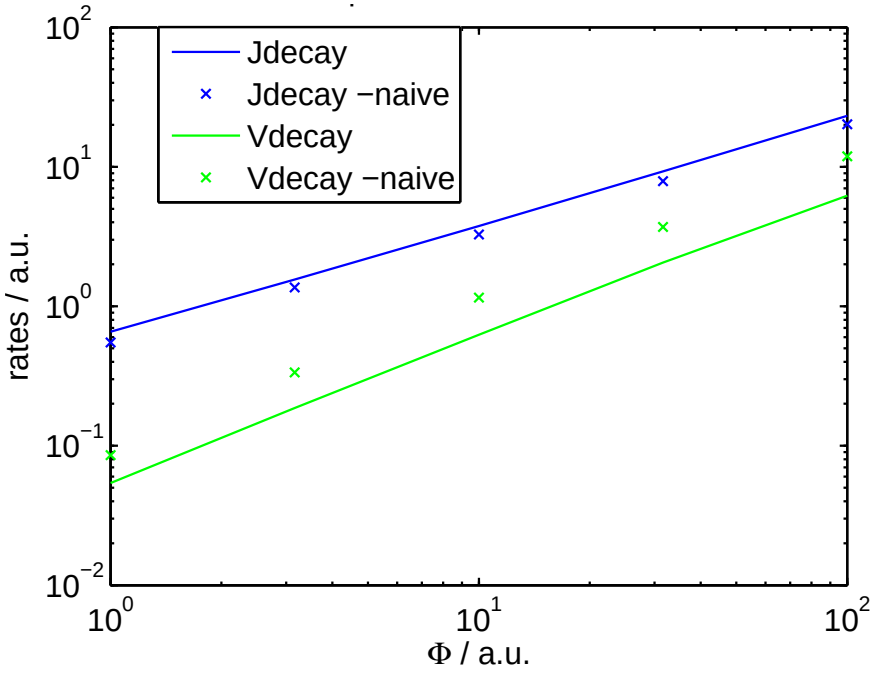

Figure 4.2: Comparison of current and voltage decay rates as a function of light intensity. Solid lines refer to decay rates computed from Equations 4.14 (blue, current) and 4.13 (green, voltage) based on the average charge density, $\langle \bar{n}_0 \rangle$. The plotted points refer to decay rate values obtained through a full simulation of Equation 4.4 using a varying charge density profile; the parameter values used for the simulation are: $\alpha = 2$, $b = 1.5$, $\lambda = 1$, $m\beta = 0.3$.

As we will discuss later, the transient voltage decay at short circuit is liable to large deviation if the experimenter is not careful to limit the perturbation intensity. Therefore, we opt to use the transient open circuit voltage decay constant dependence on light intensity instead in Equation 4.16. Equation 4.13 applies just as well (in fact better, since the charge density is actually close to spatially invariant) to open circuit transient decays, and the signal from the V_{OC} decay is much more consistent. By extension, if the reliability of the V_{SC} decay is not fully trustworthy, that can jeopardize the accuracy of Equation 4.15. This concern, however, is only valid if the voltage decay rate at short circuit approaches the same order of magnitude as the current decay rate; this is not the case for devices with high collection efficiencies. If we have an inefficiently collecting device, we can validate or correct the value of $m\beta$ by independently finding m and β. Recall

the Chapter 3 Equations 3.3 and 3.4, reprinted below:

$$n_l = N_{l0} exp\left(\frac{\beta E_f}{kT}\right) \tag{3.3}$$

$$n = N_0 exp\left(\frac{E_f}{mkT}\right) \tag{3.4}$$

We can deduce β by applying Equation 3.3 to a plot of capacitance (C) vs open circuit voltage, as described in the Introduction. Namely:

$$\beta = \mathrm{kT}\frac{\partial \log(C)}{\partial \mathrm{V_{OC}}} \tag{4.17}$$

Similarly, we can extract m, the diode ideality parameter (which is different from our solar cell ideality factor, which was defined in Chapter 3 as $\frac{m}{b}$) from:

$$m = \frac{b}{\mathrm{kT}}\frac{\partial \mathrm{V_{OC}}}{\partial \log(\Phi)} \tag{4.18}$$

Now, Equation 4.18 does depend on the value of b; if there is a discrepancy at this point between the value of $m\beta$ calculated from Equation 4.15 and Equations 4.17 and 4.18, then we employ an iterative method such that Equations 4.16, 4.17, and 4.18 are mutually compatible.

Next, the absorption coefficient, α is extracted from the absorption spectrum of the sensitizing dye. Specifically, we determine the absorption depth at the peak absorbing wavelength and divide by the device thickness to obtain α. An alternative method involves computing a weighted average of the absorption depth for each wavelength in the spectrum—while this yields a different value of α, we find that the difference affects the simulation results negligibly, so either method of fitting α works adequately.

For simulating the short circuit condition, the non-dimensional charge density at the boundary, ν, is chosen to be very small, $\sim 10^{-6}$ (we arrive at this value by reducing the magnitude of ν until the simulation results converge. Recall that ν refers to the nondimensional charge density at the left hand boundary, which we can assume at short circuit to be vanishingly small but cannot assign a value of zero for computational reasons). Finally, the nondimensional recombination

length, λ, is adjusted until the simulated value matches the measured value of $\frac{\kappa_0^J}{\kappa_0^V}$ at the desired light intensity (if $b \approx 1$ this should be invariant).

The following table summarizes how we fit the five parameters in Equation 3.13 and its Boundary Conditions 1.11:

Parameter	Meaning	Method	Equation
α	Absorption Depth	Absorption Spectrum	
$m\beta$	Relationship between n and n_l	Small Perturbation J_{SC} and V_{SC} decays	4.15
b	Nonlinear Recombination Parameter	Small Perturbation V_{OC} decay	4.16
β	Trap DOS Parameter	Capacitance vs V_{OC}	4.17
m	Diode Ideality Parameter	V_{OC} vs Φ	4.18
λ	Diffusion Length	Match Ratio of Simulated to Measured κ_0^J to κ_0^V	
ν	LHS Charge Density	N/A	$\sim 10^{-6}$

Table 4.1: Nondimensional Parameters in Equation 4.4, their meanings, the experimental data used to fit them, and the equations introduced earlier, if any, used to link experimental data to simulation parameters. Note that the value of ν used here is only valid at short circuit.

4.4 Results

We have introduced the relevant methodological tools above and will use them to assess η_{approx}, the estimated value of the collection efficiency η_c obtained from small perturbation measurements.

4.4.1 Effect of Perturbation Size

We begin by assessing the effect of perturbation size on the measured photocurrent and photovoltage decay rates. Recall that the perturbation pulse must be appropriately small to justify the linearity approximation, Equation 4.3, in the linear partial differential equation describing transient decays, Equation 4.4. Therefore, we basically compare the simulated solution of the full governing equation, Equa-

tion 3.13, under large perturbations to that of its linearized counterpart valid under small and uniform charge generation, Equation 4.4

Figure 4.3 illustrates the effect of increasing the size of the perturbation on the measured decay constants for voltage and current decays. The solid lines use MATLAB simulations to compare the device decay rate to its "ideal" value, i.e., that obtained in the limit of low perturbation intensity and uniform charge generation. To simulate the actual decay rate, we numerically solve Equation 3.13, using MATLAB's `pdepe` partial differential equation solver. To determine the ideal decay rate, we numerically obtain the exponential parameter corresponding to the lowest spatial eigenfunction of the solution to 4.4, using MATLAB's `bvp5c` boundary value problem solver (recall that we cannot just use Equations 4.13 and 4.14 if we want to correctly treat a varying charge density profile). Plotted data points correspond to experimentally measured decay rates of a fabricated cell, and the fitted cell parameters ($b = 1.026,\ m\beta = .348,\ \lambda = 2.2$) were used to simulate the ideal decay rates. Experimental decay rates were fit according to the fitting protocol described earlier in this Chapter and in Chapter 2 whereby only the monoexponential long-term behavior was fit.

While the J_{SC} decay constant (κ_J) stays relatively constant with increasing perturbation size, the V_{SC} decay constant (κ_V) is rapidly overestimated. To understand this effect, recall from Equation 1.11 that κ_V is a proxy for the decay of the logarithm of charge density decay at $x = 0$. Since the equilibrium value of charge density, $n_0|_{x=0}$ is nearly 0, any perturbation, n_1, is comparatively enormous, evident from Figure 4.1. Thus for any $b > 0$, the decay rate will be very sensitive to perturbation size, since the recombination rate goes as n^b. Conversely, κ_J is not as sensitive to perturbation intensity because the value of $n|_{x=0}$ is held constant and the perturbation in $\frac{\partial n}{\partial x}|_{x=0}$ is much smaller than its equilibrium value $\frac{\partial n_0}{\partial x}|_{x=0}$.

Since the error in the measured decay rate is on the order of 2-3$\times$ at most, this effect only significantly influences estimation of η_c when κ_V approaches the same order of magnitude as κ_J, corresponding to values of η_c below 0.9. Above that threshold value, the magnitude of κ_J is sufficiently greater than κ_V such that variation in κ_V causes underestimation of η_c by at most 5 %. However, as κ_J and κ_V approach each other and the collection efficiency drops, underestimation

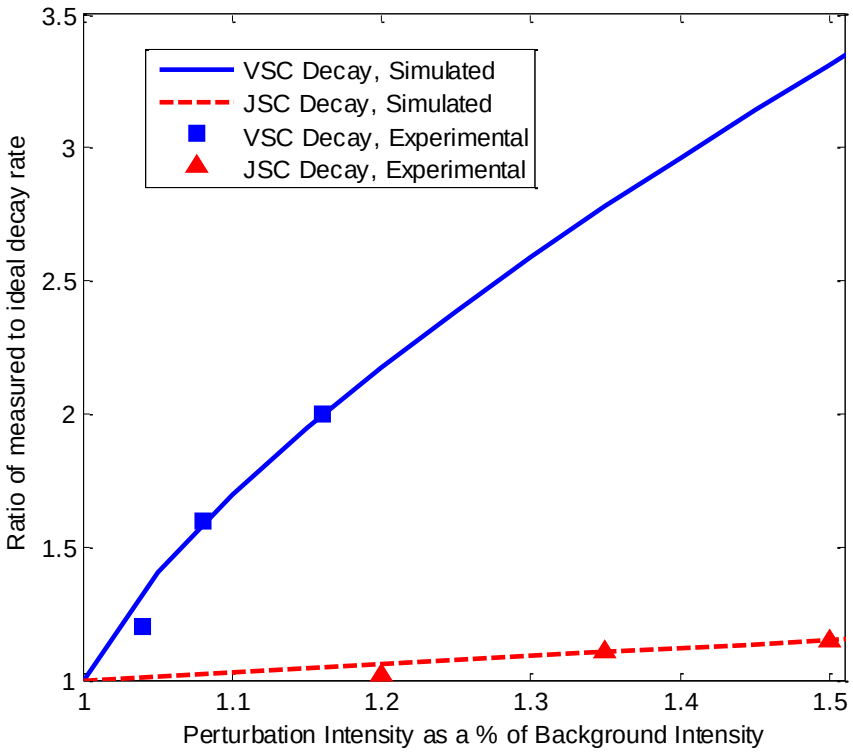

Figure 4.3: Divergence of observed decay constants for V_{SC} and J_{SC} decays from their "ideal" values as a function of perturbation light intensity.

from large perturbations becomes increasingly significant. Good experimental practice should involve varying the size of the voltage perturbation to ensure that the decay constant has stabilized (at full sun, our measured κ_V stabilized at a perturbation of <10mV); this process should be repeated for each background light intensity. We note that although a high η_c is quite insensitive to changes in κ_V, the often quoted electron diffusion length will be underestimated by the squareroot of the overestimation in κ_V.

4.4.2 Divergence of η_{approx} and η_c

Even if the perturbation is kept extremely small, there are still inherent errors in η_{approx}; these arise from the fact that we are estimating a steady state property, the collection efficiency, with transient techniques. Therefore, under the assumptions of small and uniform charge generation, we proceed to compare the

collection efficiency calculated through full simulation of Equation 3.13 to an ideal measurement of η_{approx}.

4.4.2.1 Simulated Comparison

Figure 4.4(a) displays simulation results for η_{approx} and η_c for a range of values of λ and b. Since the collection efficiency is a steady state parameter, we used MATLAB's ordinary differential equation solver `ode45` to evaluate η_c via Equation 3.19, and we obtained η_{approx} by applying Equation 4.1 on the simulated ideal decay rates. The results suggest that for devices with measured η_{approx} above 0.9, the error is less than 5%. However, measured values of η_{approx} below 0.9 can significantly overestimate the real value of η_c by up to 20% over the range simulated.

The simulated devices in Figure 4.4 were all given the same value of $m\beta$, 0.3, which characterizes almost all of the solid-state DSSCs we tested. The value of $m\beta$ is a function of the trapped charge DOS shape and the solar cell ideality factor and describes the relationship between free and trapped charge populations. It has no effect on the collection efficiency (which is a function of the steady state current), but it does affect transient equilibration of trapped and free electrons and therefore changes the measured value of η_{approx}.[20]

This is the crux of the disagreement between η_c and η_{approx}; only the latter is a function of $m\beta$. If $m\beta = 0.3$, η_{approx} overestimates η_c, if $m\beta = 0.5$, η_{approx} underestimates η_c, and the researcher who unwittingly fabricates a device with $m\beta = 0.4$ will find his measured collection efficiency delightfully accurate. Below, Figure 4.5 details the effect of changing $m\beta$ on the size and direction of the error in estimating η_c (in this figure, the value of b was held at 1 and the recombination length, λ, was varied, but the trends are consistent for any constant value of b. For devices with a high collection efficiency (i.e., $\kappa_J \gg \kappa_V$), the effect of $m\beta$'s value is to change the values of the decay rates, but their ratio will still remain large and η_{approx} will remain close to η_c.

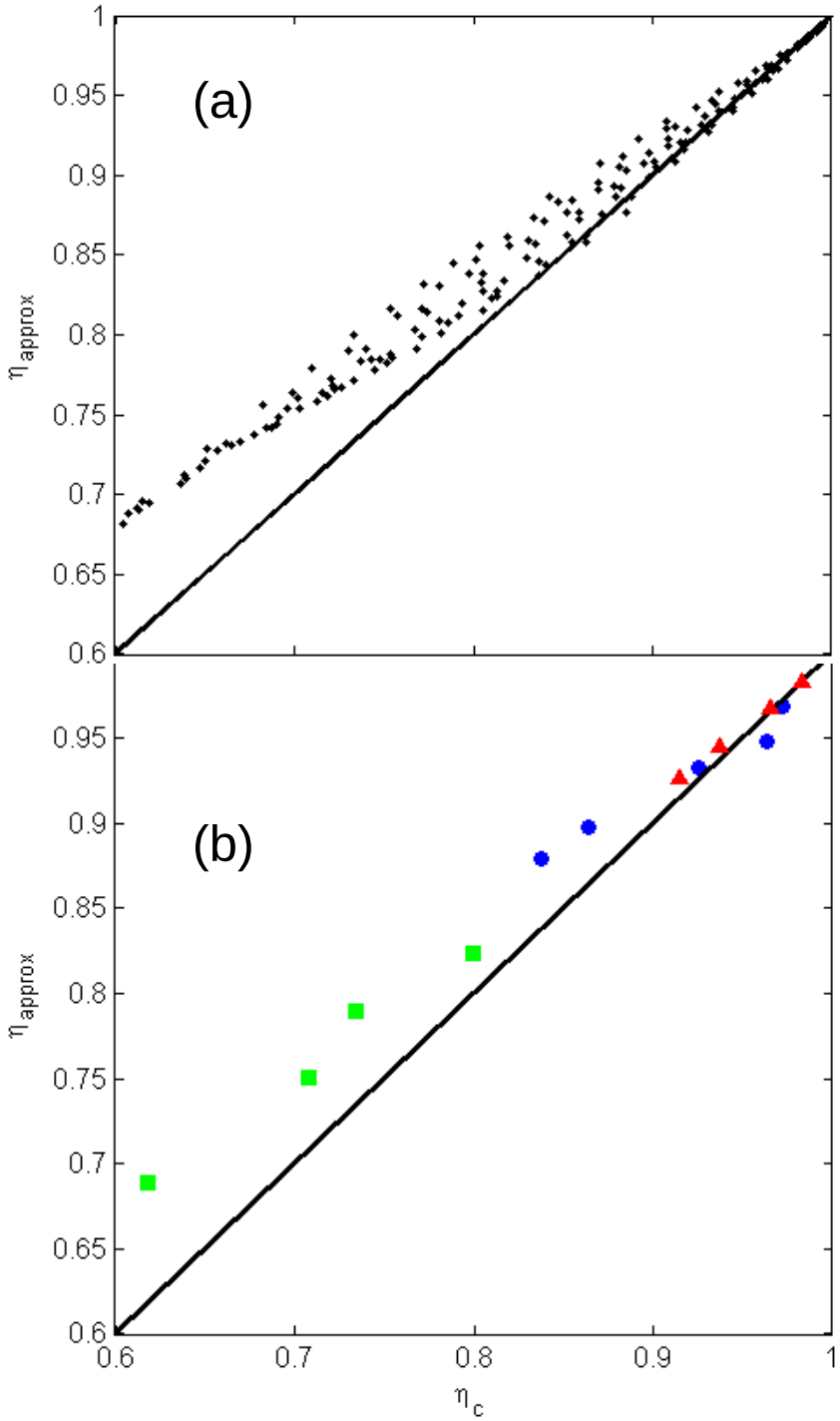

Figure 4.4: a) Various simulated values of η_{approx} vs η_c for $m\beta = 0.3$, $b \in [0.5, 1.5]$, $\lambda \in [0.3, 3]$ b) Experimental values of η_{approx} vs η_c for i) (blue circles) [Li-TFSI] varied from 2mM to 50mM, ii) (red triangles) Al_2O_3 immersion time varied from 1 to 20 minutes, and iii) (green squares) Spiro concentration varied from 4% to 7%. The solid lines denote agreement between η_{approx} and η_c.

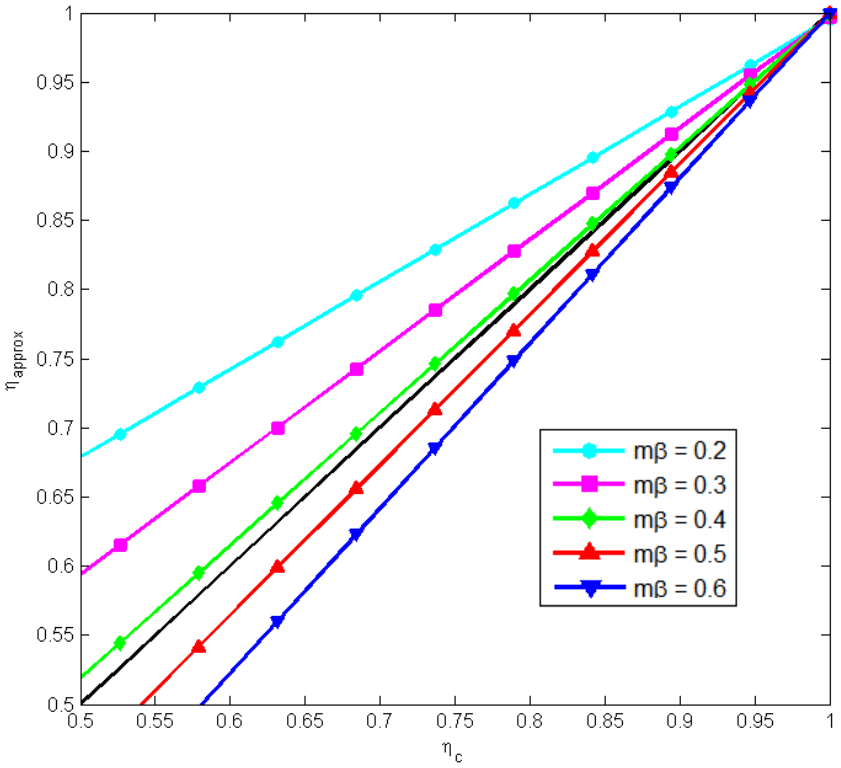

Figure 4.5: η_{approx} vs ηc for various values of $m\beta$. The value of b was held constant at 1, and λ was varied to generate each line

4.4.2.2 Simulation Using Fitted Parameters from Real Devices

Figure 4.4(b) presents three series of solid-state DSSCs fabricated with a range of material parameters (i.e., concentration of Li-TFSI in the hole transporter) to vary the resultant collection efficiency. All devices were fabricated according to the standard protocol introduced in Chapter 2 with any deviations noted below. For each device, simulation parameters were extracted, the steady state simulation was run on MATLAB, and the value of η_c calculated from Equation 3.19 was compared to the measured value of η_{approx}. The fitted parameter values are listed below in Table 4.2.

We begin with an Al_2O_3 shell thickness series, designed to inhibit electronic recombination from the TiO_2 to the surrounding hole transporter. To create this shell, substrates having just undergone $TiCl_4$ treatment were subsequently immersed for 1-20 minutes in a solution of 10mM aluminum isopropoxide in a

Treatment	$m\beta$	b	λ
2mM Li-TFSI	0.28	0.95	1.20
5mM Li-TFSI	0.24	1.01	1.25
10mM Li-TFSI	0.31	1.09	1.58
20mM Li-TFSI	0.41	1.19	2.20
50mM Li-TFSI	0.62	1.17	1.80
No Al_2O_3	0.31	1.01	1.65
1 min Al_2O_3	0.32	1.01	1.95
6 min Al_2O_3	0.35	1.02	2.60
20 min Al_2O_3	0.36	1.02	3.71
4% Spiro	0.32	1.19	0.50
5% Spiro	0.31	1.22	0.62
6% Spiro	0.27	1.17	0.69
7% Spiro	0.30	1.20	0.82

Table 4.2: Fitted simulation parameters for the synthesized solid-state DSSCs whose collection efficiencies are plotted in Figure 3(b). α was held at 1.5.

1:1 solution of tert-butanol:acetonitrile. Consistent with previous reports demonstrating reduced recombination rates, increasing the immersion time and hence the shell thickness almost exclusively modified the recombination length, λ, while leaving b and $m\beta$ constant.[21; 22] Since these devices all had high collection efficiencies, the error in measurement was minimal.

(Note that the devices likely had different injection efficiencies, inversely related to the thickness of the shell. The generation term in Equation 3.13 does not explicitly account for injection efficiency, but as long as the generation rate for each device remains proportional to light intensity, albeit with different constants of proportionality, the power law parameter fitting protocol introduced earlier will remain valid.)

Therefore, we next aimed to fabricate devices in the regime of charge collection efficiency where measurement errors would be significant. By varying the concentration of the spincoated Spiro-OMeTAD hole-transporter solution between 4% and 7% (holding the additive:Spiro ratio (m/m) constant), we modulated the pore-filling fraction.[23] Again, this mostly changed the value of λ. This is consistent with previous reports which assert that the thicker the hole transporter coating on TiO_2 nanoparticles, the slower the rate of recombination; we can ra-

tionalize this by noting that the hole density in a well infiltrated hole transporter will be lower than that in a device with poor pore filling. Since these devices were much inferior to those in the Al_2O_3 shell series, the discrepancy between η_{approx} and η_c is pronounced and reflects the severe underestimation which we predicted by simulating devices with similar values of $m\beta$ and b.

Finally, we varied the Li-TFSI ionic salt concentration, which has been shown to have multiple effects on device operation. The concentration of Li-TFSI was varied between 2mM and 50mM, while the Spiro-OMeTAD concentration was held constant at 10%. Notably, addition of Li-TFSI broadens the trap DOS, increasing the value of $m\beta$; the lone underestimating value of η_{approx} corresponds to the highest Li-TFSI concentration, demonstrating that there is no simple correction factor to adjust for the inaccuracy of η_{approx}.[24]

To summarize the above findings, η_{approx} deviates from η_c as either the measured or true collection efficiency decreases. This occurs as a result of two errors: first, the V_{SC} decay constant is very sensitive to perturbation size, and second, η_{approx} is influenced by trapping kinetics and thus misapprehends the steady state collection efficiency. These effects conspire to generate large errors only if devices exhibit measured collection efficiencies below 90%. This finding neatly dovetails with the insight that steady state measurements of the collection efficiency, via illumination of both sides of the device to extract external quantum efficiency, are only accurate for low collection efficiencies. The steady state measurement loses resolution when there is not a sufficient difference between measurements under substrate and counterelectrode side illumination, indicating that the diffusion length considerably exceeds the device thickness. Conversely, transient perturbation measurements lose resolution when the voltage and current decay rates approach each other, i.e., when the timescales for transport and recombination are comparable and the collection efficiency is low. Together, steady state and transient measurements can be used to characterize the whole range of collection efficiencies. Parameter fitting and simulation can be employed to refine low estimated η_{approx} values from small perturbation measurements, but barring this, it would be prudent to use η_{approx} as just a litmus test for high collection efficiency.

Despite its wide use, the short circuit collection efficiency may be an inferior

performance metric than the collection efficiency at the cell's ideal operating point, that at maximum power. In fact, Equation 3.19 is not restricted to the short-circuit condition; it is an equally valid expression for collection efficiency at any cell operating condition. However, the short circuit collection efficiency, η_c, is a worthwhile measure to study because the collection efficiency scales linearly with the photocurrent for a given light intensity. At short circuit, the dark current through the diode is close to zero, so the current under illumination is approximately the photocurrent. However, at forward bias, the photocurrent needs to be calculated by subtracting the non-negligible dark current from the current through illumination. In order to determine the collection efficiency at the maximum power point, and assuming that charge generation is independent of voltage, we can scale η_c by the ratio of photocurrent at maximum power point (the light minus dark current) to the short circuit current. An alternative experimental procedure entails transient decays at the maximum power point, either holding the voltage constant to determine κ_J or the current constant to determine κ_V. In this case, the charge density profiles before and after perturbation would be more uniform than under the short circuit conditions of Figure 4.1; i.e., the current, proportional to $\frac{\partial n}{\partial x}|_{x=0}$, would be lower, and the charge density at the electrode, $n|_{x=0}$, would be higher. While this would reduce the sensitivity of the voltage perturbation decay rate, the first of the two sources of error in measuring the collection efficiency, the fundamental error caused by transient equilibration would remain. Therefore the conclusions of this study hold for determining the maximum power point collection efficiency—whether calculated by scaling η_c or by conducting the measurement at the maximum power point, the measurement has its discussed limitations because it is a transient determination of a steady-state quantity.

4.5 Conclusion

The use of η_{approx} as an accurate measure of η_c is justifiable only when the device collection efficiency is above 90%. Below that value, the sensitivity of η_{approx} to changes in κ_J and κ_V becomes substantial. κ_V is susceptible to large over-estimation as the perturbation size increases, leading to underestimates of η_c.

Both decay rates are affected by transient equilibration between free and trapped charge, and for the most common value of the trap DOS shape, this causes η_{approx} to overestimate η_c. As a device's collection efficiency improves, the error in the decay rates does not decrease, but the impact of errors in measuring the decay rates is mitigated by the increased difference between κ_J and κ_V.

In this Chapter, we applied the nondimensional modeling framework developed in Chapter 3 to perform simulations of transient decays and fit experimental data. We demonstrated a simple fitting protocol, complete with extra validating methods, to translate between experimental measurements and simulated characterization of a device without requiring extensive knowledge of the material. By comparing simulation results to experimental data from DSSCs intentionally fabricated to exhibit a range of collection efficiencies, we have demonstrated increasing inaccuracy in transient methods as η_c decreases. Fortunately, this corresponds to the regime under which steady state measurements excel at providing accurate estimates of the collection efficiency. We therefore suggest that researchers use small perturbation methods with confidence first to separate efficiently collecting devices from inefficient ones and then only to quantify the collection efficiency of the superior devices. Unfortunately, because $m\beta$, a parameter specific to device materials and preparation, influences the size and direction of the error, a simple universal correction factor cannot be applied; more accurate quantification of the collection efficiency for inefficient devices requires determination of $m\beta$ followed by simulation.

4.6 References

[1] Varun Sivaram, James Kirkpatrick, and Henry Snaith. Critique of charge collection efficiencies calculated through small perturbation measurements of dye sensitized solar cells. *Journal of Applied Physics*, 113(6):063709–063709–6, 2013. 64

[2] J. van de Lagemaat, N.-G. Park, and A. J. Frank. Influence of electrical potential distribution, charge transport, and recombination on the photopotential and photocurrent conversion efficiency of dye-sensitized nanocrystalline

TiO2 solar cells: A study by electrical impedance and optical modulation techniques. *The Journal of Physical Chemistry B*, 104(9):2044–2052, 2000. 64

[3] Matt Law, Lori E. Greene, Justin C. Johnson, Richard Saykally, and Peidong Yang. Nanowire dye-sensitized solar cells. *Nat Mater*, 4(6):455–459, June 2005. 64

[4] Brian C. O'Regan, James R. Durrant, Paul M. Sommeling, and Nicolaas J. Bakker. Influence of the TiCl4 treatment on nanocrystalline TiO2 films in dye-sensitized solar cells; charge density, band edge shifts, and quantification of recombination losses at short circuit. *The Journal of Physical Chemistry C*, 111(37):14001–14010, 2007. 65, 66

[5] Brian C. O'Regan and Frank Lenzmann. Charge transport and recombination in a nanoscale interpenetrating network of n-type and p-type semiconductors: Transient photocurrent and photovoltage studies of TiO2/Dye/CuSCN photovoltaic cells. *J. Phys. Chem. B*, 108(14):4342–4350, March 2004. 65

[6] Juan Bisquert, David Cahen, Gary Hodes, Sven Rahle, and Arie Zaban. Physical chemical principles of photovoltaic conversion with nanoparticulate, mesoporous dye-sensitized solar cells. *The Journal of Physical Chemistry B*, 108(24):8106–8118, 2004. 66

[7] Ivan Montanari, Jenny Nelson, and James R. Durrant. Iodide electron transfer kinetics in dye-sensitized nanocrystalline TiO2 films. *The Journal of Physical Chemistry B*, 106(47):12203–12210, 2002. 66

[8] W. H. Leng, Piers R. F. Barnes, Mindaugas Juozapavicius, Brian C. O'Regan, and James R. Durrant. Electron diffusion length in mesoporous nanocrystalline TiO2 photoelectrodes during water oxidation. *The Journal of Physical Chemistry Letters*, 1(6):967–972, 2010. 66

[9] Piers R. F. Barnes, Assaf Y. Anderson, Sara E. Koops, James R. Durrant, and Brian C. O'Regan. Electron injection efficiency and diffusion length in

dye-sensitized solar cells derived from incident photon conversion efficiency measurements. *The Journal of Physical Chemistry C*, 113(3):1126–1136, 2009. 66

[10] Piers R. F. Barnes, Lingxuan Liu, Xiaoe Li, Assaf Y. Anderson, Hawraa Kisserwan, Tarek H. Ghaddar, James R. Durrant, and Brian C. O'Regan. Re-evaluation of recombination losses in dye-sensitized cells: The failure of dynamic relaxation methods to correctly predict diffusion length in nanoporous photoelectrodes. *Nano Letters*, 9(10):3532–3538, 2009. PMID: 19645462. 66, 67

[11] J. Villanueva-Cab, G. Oskam, and J.A. Anta. A simple numerical model for the charge transport and recombination properties of dye-sensitized solar cells: A comparison of transport-limited and transfer-limited recombination. *Solar Energy Materials and Solar Cells*, 94(1):45 – 50, 2010. 17th International Materials Research Congress 2008. 66

[12] Piers R. F. Barnes and Brian C. O'Regan. Electron recombination kinetics and the analysis of collection efficiency and diffusion length measurements in dye sensitized solar cells. *The Journal of Physical Chemistry C*, 114(44):19134–19140, 2010. 66, 67

[13] Janne Halme. Linking optical and electrical small amplitude perturbation techniques for dynamic performance characterization of dye solar cells. *Phys. Chem. Chem. Phys.*, 13:12435–12446, 2011. 67

[14] Brian C. O'Regan, Klaas Bakker, Jessica Kroeze, Herman Smit, Paul Sommeling, and James R. Durrant. Measuring charge transport from transient photovoltage rise times. a new tool to investigate electron transport in nanoparticle films. *The Journal of Physical Chemistry B*, 110(34):17155–17160, 2006. 68

[15] Juan Bisquert and Ivan Mora-Sero. Simulation of steady-state characteristics of dye-sensitized solar cells and the interpretation of the diffusion length. *The Journal of Physical Chemistry Letters*, 1(1):450–456, 2010. 69

[16] Emil Enache-Pommer, Janice E. Boercker, and Eray S. Aydil. Electron transport and recombination in polycrystalline TiO2 nanowire dye-sensitized solar cells. *Applied Physics Letters*, 91(12):123116, 2007. 71

[17] Piers R. F. Barnes, Assaf Y. Anderson, James R. Durrant, and Brian C. O'Regan. Simulation and measurement of complete dye sensitised solar cells: including the influence of trapping, electrolyte, oxidised dyes and light intensity on steady state and transient device behaviour. *Phys. Chem. Chem. Phys.*, 13(13):5798–5816, 2011. 72

[18] Juan A. Anta, Jesus Idigoras, Elena Guillen, Julio Villanueva-Cab, Humberto J. Mandujano-Ramirez, Gerko Oskam, Laila Pelleja, and Emilio Palomares. A continuity equation for the simulation of the current-voltage curve and the time-dependent properties of dye-sensitized solar cells. *Phys. Chem. Chem. Phys.*, 14:10285–10299, 2012. 72

[19] PM Sommeling, BC O'Regan, RR Haswell, HJP Smit, NJ Bakker, JJT Smits, JM Kroon, and JAM Van Roosmalen. Influence of a TiCl4 post-treatment on nanocrystalline TiO2 films in dye-sensitized solar cells. *The Journal of Physical Chemistry B*, 110(39):19191–19197, 2006. 73

[20] Juan A. Anta, Fabiola Casanueva, and Gerko Oskam. A numerical model for charge transport and recombination in dye-sensitized solar cells. *J. Phys. Chem. B*, 110(11):5372–5378, March 2006. 79

[21] V. Ganapathy, B. Karunagaran, and Shi-Woo Rhee. Improved performance of dye-sensitized solar cells with TiO2/alumina core/shell formation using atomic layer deposition. *Journal of Power Sources*, 195(15):5138 – 5143, 2010. 82

[22] Francisco Fabregat-Santiago, Jorge Garcia-Canadas, Emilio Palomares, John N. Clifford, Saif A. Haque, James R. Durrant, Germa Garcia-Belmonte, and Juan Bisquert. The origin of slow electron recombination processes in dye-sensitized solar cells with alumina barrier coatings. *Journal of Applied Physics*, 96(11):6903–6907, 2004. 82

[23] Henry J Snaith, Robin Humphry-Baker, Peter Chen, Ilkay Cesar, Shaik M Zakeeruddin, and Michael Gratzel. Charge collection and pore filling in solid-state dye-sensitized solar cells. *Nanotechnology*, 19(42):424003–, 2008. 82

[24] H. J. Snaith and M. Grätzel. Enhanced charge mobility in a molecular hole transporter via addition of redox inactive ionic dopant: Implication to dye-sensitized solar cells. *Applied Physics Letters*, 89(26):262114, December 2006. 83

Chapter 5

Higher Mobility Materials for Improving Charge Transport

5.1 Introduction

The nanocrystalline TiO_2 (nc-TiO_2) network invented by O'Regan and Gratzel in the first incarnation of the DSSC has largely survived intact to the present day.[1] Setting aside improvements in the synthesis protocol and surface treatment optimization, the photoanode of choice looks and acts largely the same over 20 years later.[2] We have discussed some of the reasons previously, but fundamental to the resilience of nc-TiO_2 is a surprisingly long electron lifetime that allows a low effective diffusion coefficient to yield respectable collection efficiencies.[3; 4]

However, while the nc-TiO_2 scaffold has served the liquid DSSC well, it is not clear that it is well suited to the solid state DSSC (SDSC). Indeed, the Achilles' Heel of the SDSC has been the requirement that the cell thickness remain at or below 2μm, over five times thinner than the TiO_2 film of a liquid DSSC counterpart.[5; 6] The canonical reason is that at higher film thickness, the solid state hole transporter cannot infiltrate the nanocrystalline porosity as well as a liquid electrolyte can. As a result, the light absorption is far from complete and the short circuit current is undercut.

Put differently, the single greatest problem obstructing the advancement of the SDSC is that the competing requirements of light absorption and charge

collection cannot be jointly optimized.[7] As the film thickness increases in the SDSC, the long electron lifetime realized in the liquid DSSC diminishes, and without a generous lifetime to compensate for the languid electronic transport processes, recombination quickly overtakes transport and reduces the device efficiency. Therefore, this Chapter aims to alter the balance between transport and recombination by opting for different materials and nanostructures which promise enhanced transport. Under a quicker transport regime, the electron lifetime degradation in thicker SDSCs may not fatally compromise device performance.

(Note that other researchers have already abandoned the nc-TiO_2 paradigm of solid-state solar cells, opting instead for an insulating alumina scaffold to support a perovskite material which performs absorption and transport functions.[8] That device architecture is sufficiently radical that the SDSC designation does not really apply; this Chapter aims to investigate methods of enhancing charge transport in devices which will still be SDSCs.)

SnO_2 and ZnO are promising replacement materials for conventionally used TiO_2 because of their higher bulk mobilities—250 $cm^2V^{-1}s^{-1}$ and 205 $cm^2V^{-1}s^{-1}$, respectively, each over 2 orders of magnitude higher than the $\sim$1 $cm^2V^{-1}s^{-1}$of bulk TiO_2.[9; 10] Moreover, single crystal nanowires of high mobility metal oxides can leverage the high electronic mobility because electron transport will, ideally, not be limited by trapping process rate constants.[11] In this Chapter, we fabricate SDSCs by first replacing the photoanode and hole transporter with high mobility materials. Subsequently, we investigate nanowire photoanodes and their potential for advancing the performance and characterization of SDSCs.

5.2 Optimized electronic contacts in SnO_2-dye-P3HT based Solid State Dye Sensitized Solar Cells [1]

5.2.1 Background

Increasing electron mobility in the nc-TiO_2 while holding the Spiro-OMeTAD hole mobility constant, and vice versa, may cause limited enhancements to charge transport because ambipolar diffusion stipulates that opposite charges are extracted at the same rate. This is especially relevant under forward bias near and beyond the maximum power point, since Spiro-OMeTAD does not exhibit increased conductivity with greater charge density and is in fact the least conductive component under these conditions.[13] Therefore, we sought replacement materials for both TiO_2 and Spiro-OMeTAD to minimize the transport bottleneck over all working conditions.

SnO_2 and Poly(3-hexylthiophene) (P3HT) have been established as promising high mobility alternatives to conventional SDSC components. Bulk and nanostructured SnO_2 exhibit electron mobilities of about 250 and 124 $cm^2V^{-1}s^{-1}$ respectively (recall, over 2 orders of magnitude higher than the $\sim$1 $cm^2V^{-1}s^{-1}$ of bulk TiO_2.[14] This mobility hike is yet to be demonstrated in mesoporous SnO_2 films,[15] but presumably this is due to lack of effort and optimization, rather than fundamental limitations. Similarly, P3HT's mobility of 0.1 $cm^2V^{-1}s^{-1}$ is decisively superior to that of Spiro-OMeTAD (10^{-4} $cm^2V^{-1}s^{-1}$), though the degree of crystallization of P3HT can impact the mobility by orders of magnitude.[16]

Additionally, SnO_2's conduction band energy is reportedly 0.4 V below that of TiO_2, conducive to more efficient electron injection from the dye. Advantageously for UV stability, its 3.8 eV bandgap ensures minimal direct photon absorption compared to TiO_2's 3.2 eV bandgap;[17] however, the conduction band offset does suggest a lower achievable V_{OC}. P3HT has its own attendant advantages: good

[1] The research presented in this section arose from a collaboration with Golnaz Sadoughi (Sharif University, Iran) and is published in [12], from which Figures 5.1 to 5.7 were reprinted with permission. The data for Figures 5.3, 5.4, and 5.5 were obtained from cells jointly fabricated by G.S. and V.S.

solubility in most organic solvents allows low cost, solution based processing, and P3HT's efficient light harvesting behaviour in the UV-visible spectrum anticipates dual employment as a hole transporter and absorber. P3HT already fulfils both roles in tandem with fullerene electron acceptors,[18] and its capacity for Förster Resonant Energy Transfer (FRET) with an appropriate near-IR absorbing dye has yielded optimistic results.[19]

Here, we introduce the combination of SnO_2 and P3HT in a solid-state dye-sensitized solar cell, and to date this is the only study which has successfully incorporated both materials into the SDSCs. We demonstrate that the barrier to obtaining functioning solar cells is in fact the high conductivity of the constituent components which under conventional processing renders the shunt resistance too low to sustain significant diodic rectification. Through optimization of the anode and cathode contacts, we report functional devices with good rectification and greater than 1% full sun power conversion efficiency. This result proves the viability of these materials in the SDSC and opens the door for further research and optimization to advance the charge transport properties and ultimately the efficiency of the SDSC.

5.2.2 Results and Discussion

The following discussion will explore the roadblocks to simple substitution of new materials for the conventional photoanode and hole transporter. The higher mobility of the replacement materials proved to be a double edged sword, and the following narrative illustrates the measures taken to adapt the SDSC architecture to fabricate a viable cell out of high mobility components.

Figure 5.1 shows a cross-sectional SEM image of the optimized device. In addition to the material substitutions at the photoanode and hole conductor, the preparation and resulting structure deviate from the conventional SDSC architecture in two ways: (1) a dual compact layer is utilized, combining spray pyrolysis deposition and spin coating of SnO_2, and (2) a thick capping layer deposition is employed by another double deposition of different concentrations of P3HT in the spin-coating solution. These architectural changes, combined with MgO treatment, sensitization by ID504 dye, and optimization of the additive concentration,

enabled the power conversion efficiency of SnO_2/P3HT devices to improve from a maximum value of 0.13% in the conventional structure to a reliable 1.03%. The light and dark JV characteristics of the primitive cell without an extra compact layer and capping layer (in the presence of the other optimizations) and the final optimized cell are presented in Figure 5.2.

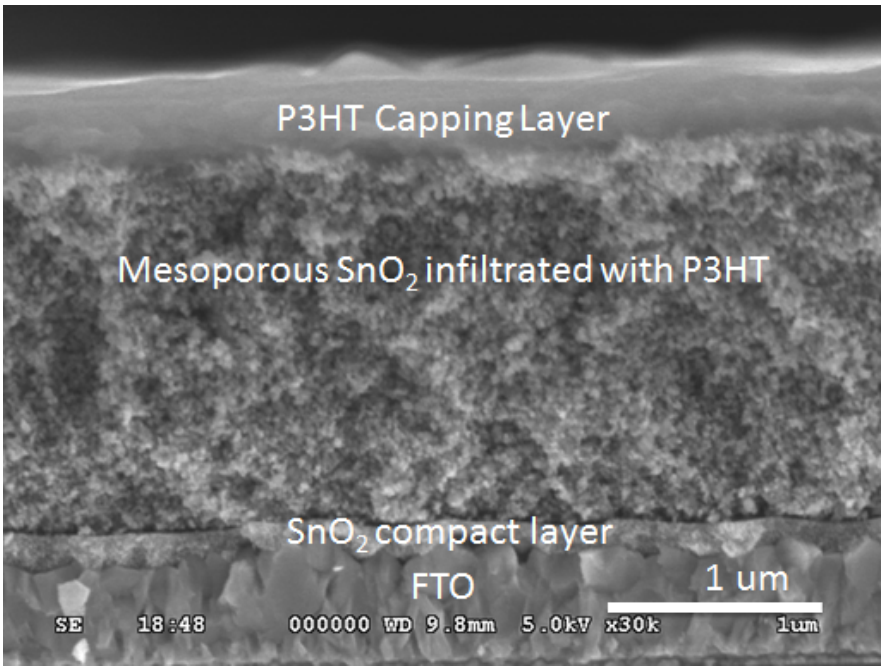

Figure 5.1: Cross-sectional SEM image of the SnO_2/P3HT SDSC, illustrating the thicknesses of the component layers. In the optimized device, the compact layer is both uniform and non-conductive enough to effectively block hole injection, and the P3HT capping layer is similarly thick enough to prevent cell shunting via electronic current.

5.2.2.1 Optimizing the SnO_2 compact layer to inhibit the hole-only leakage current

A compact layer was introduced to prevent short circuiting due to direct contact between the FTO and the hole transporter. The conventional deposition method for SnO_2 compact layers for use in SDSCs is spray pyrolysis deposition (SPD) of butyl tin chloride in ethanol (described in Chapter 2). The measured conductivity of the SnO_2 compact layer deposited by SPD is about 10^{-2}Scm^{-1}. While this SPD

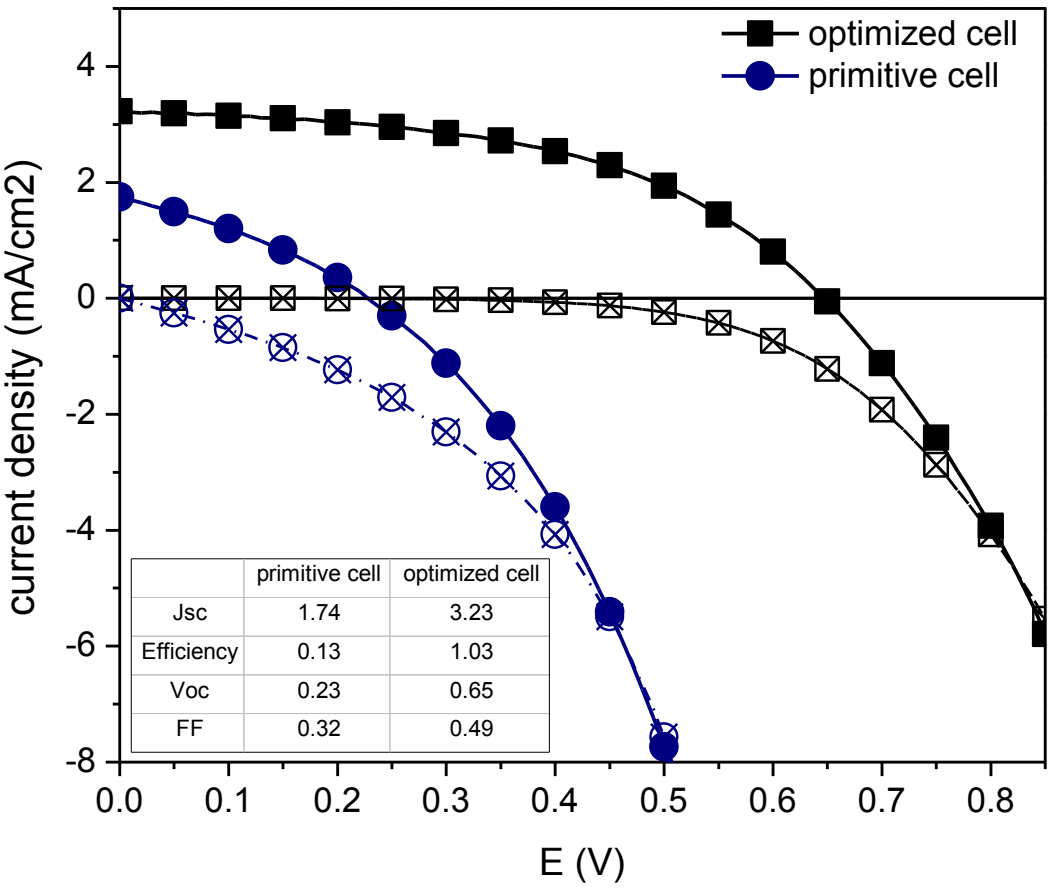

Figure 5.2: The light and dark JV characteristic of the primitive SDSC (without extra compact layer and capping layer, in presence of other optimizations) and the final optimized SDSC.

layer is appropriate for use with Spiro-OMeTAD as the hole transporting material (HTM), it is not adequately resistive when coupled with the high mobility P3HT HTM; recall that P3HT's mobility of $0.1 cm^2V^{-1}s^{-1}$ is decisively superior to that of Spiro-OMeTAD ($10^{-4}cm^2V^{-1}s^{-1}$).

A spin-coating approach was subsequently adopted in the hope of applying a more resistive layer. Indeed, the conductivity of this layer dropped by four orders of magnitude to $10^{-6}Scm^{-1}$. However, the spin-coated layer exhibited poor uniformity due to microscopic pinholes, so it alone did not suffice as a uniformly resistive blocking layer; even a device with five spin-coated layers exhibited

suboptimal leakage current, evident from Figure 5.4. Consequently, to combine the advantages of film uniformity from SPD with sufficient resistivity from spin-coating, we investigated different combinations of SPD and spin-coated layers.

Figure 5.3 details device performance results from various compact layer deposition methods and number of layers in devices infiltrated with P3HT and Spiro-OMeTAD as the HTM respectively. Five different combinations of compact layers were used to optimize SDSC devices with either spiro-OMeTAD or P3HT as the HTM. Adding more spin-coated layers on top of the SPD layer led to low fill factors. Consistent with the hypothesis that the SPD layer resistivity was only too low for use with P3HT, devices employing Spiro-OMeTAD and additional spin-coated layers attained minimal gains in V_{OC} but suffered in other metrics: the J_{SC} decreased due to the current barrier and the fill factor decreased, dominated by an increase in series resistance that was not offset by marginal gains in shunt resistance. Conversely, adding two spin-coated layers to the SPD layer in a P3HT device achieves both higher V_{OC} and J_{SC}, maximizing power conversion efficiency.

An examination of the dark J-V characteristic, presented in Figure 5.4, reveals that leakage current is highest for P3HT cells equipped with only an SPD layer and decreases as additional spin-coated layers are deposited; the dual SPD and spin-coated compact layer therefore serves as the optimized blocking layer for the P3HT hole conductor. Note that the comparisons obtained from Figures 5.3-5.4 involve devices with a double capping layer and MgO surface treatment (these optimizations are explained in subsequent sections); thus the hole leakage under consideration only occurs at the working electrode interface, and we can justifiably link additional compact layers to corresponding improvements in leakage current.

5.2.2.2 Minimizing the electron-only leakage current

Above, we dealt with the unipolar hole current through the compact layer which degrades cell performance. Now we turn to the other possible source of leakage current—shunting through the counter electrode due to an electron-only leakage current. This is traditionally minimized by ensuring a uniform capping layer of the hole transporting material; this prevents direct contact of the SnO_2 with the

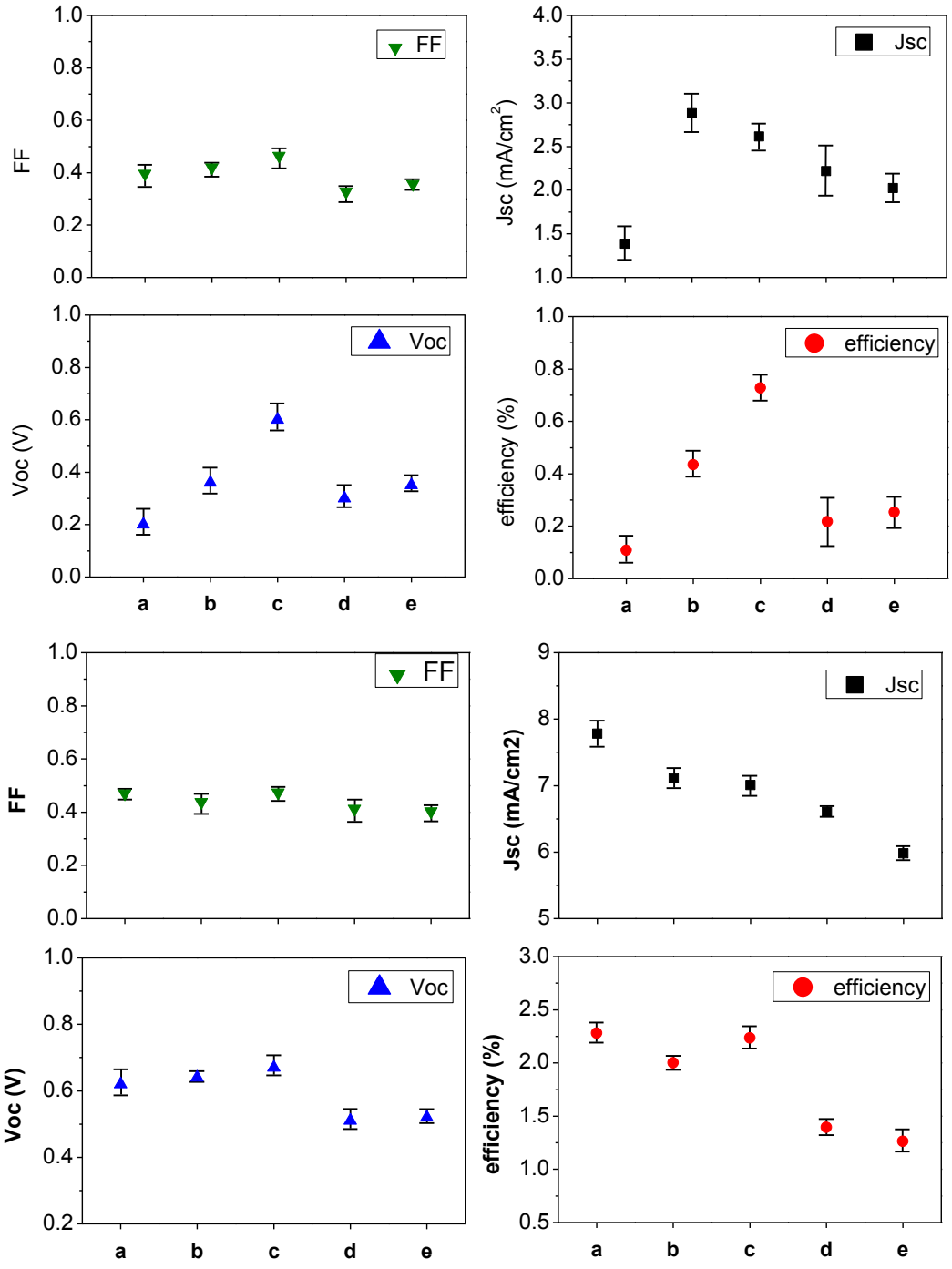

Figure 5.3: Fill factor, short circuit current density, open circuit voltage, and efficiency of SDSCs with P3HT (top panel) and Spiro (bottom panel) as the HTM and various compact layer configurations: (a) single SPD layer, (b) SPD layer with one spin-coated layer, (c) SPD layer with two spin-coated layers, (d) three spin-coated layers, (e) five spin-coated layers.

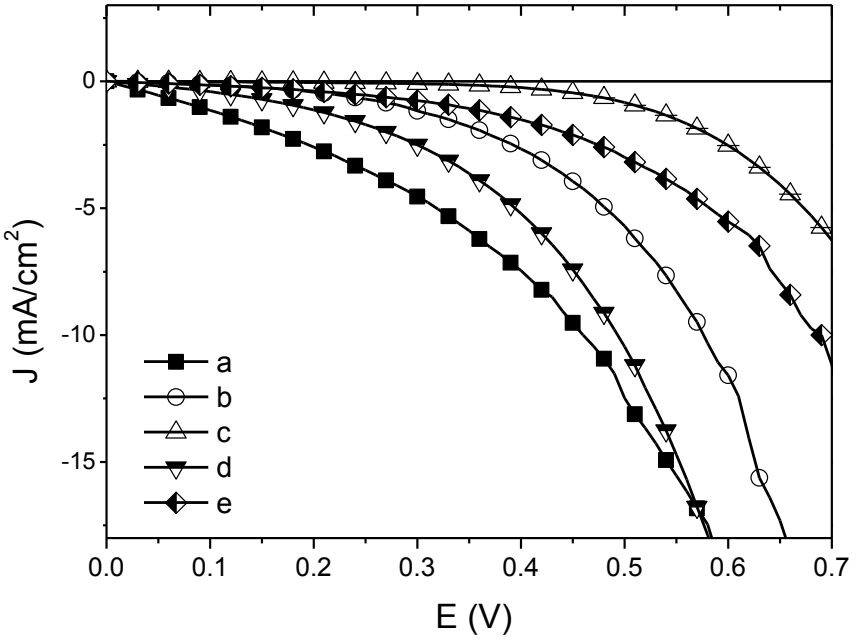

Figure 5.4: Dark JV characteristics of SDSCs with P3HT as the HTM and different compact layers configurations, as enumerated in Figure 5.3.

metallic counterelectrode.[20]

The thickness of the typical single layer of P3HT was inadequate to ensure a thick enough capping layer above the SnO_2. Indeed, a single concentration of P3HT in the chlorobenzene solvent could not accomplish the competing goals of effectively infiltrating the porous mesostructure and ensuring a uniform capping layer. The former objective requires a low concentration of P3HT to reduce the solution viscosity, and the latter goal demands a higher concentration to yield a thicker layer of HTM after solvent evaporation. Therefore, we aimed to accomplish both objectives with a dual-coating protocol which added a high concentration spin-coating step after an initial low concentration infiltration step.

To investigate the effect of capping layer thickness on solar cell performance, a second P3HT layer was deposited by spin-coating following the initial P3HT layer. All cells were given a low concentration of P3HT, 20 mg/ml, for the first layer, thereby controlling for pore filling effects on the performance of the cells. Figure 5.5 shows the effect of increasing the thickness of the P3HT capping layer

(from 50 nm to 600 nm) via variation of the concentration of the P3HT solution. Both J_{SC} and V_{OC} are significantly enhanced over the values obtained from a single low concentration layer of P3HT. While the V_{OC} increases with increasing thickness of the P3HT capping layer, the power conversion efficiency is optimized at a capping layer thickness of 360 nm; the subsequent decrease is dominated by a reduced fill factor due to increased series resistance through the thick capping layer.

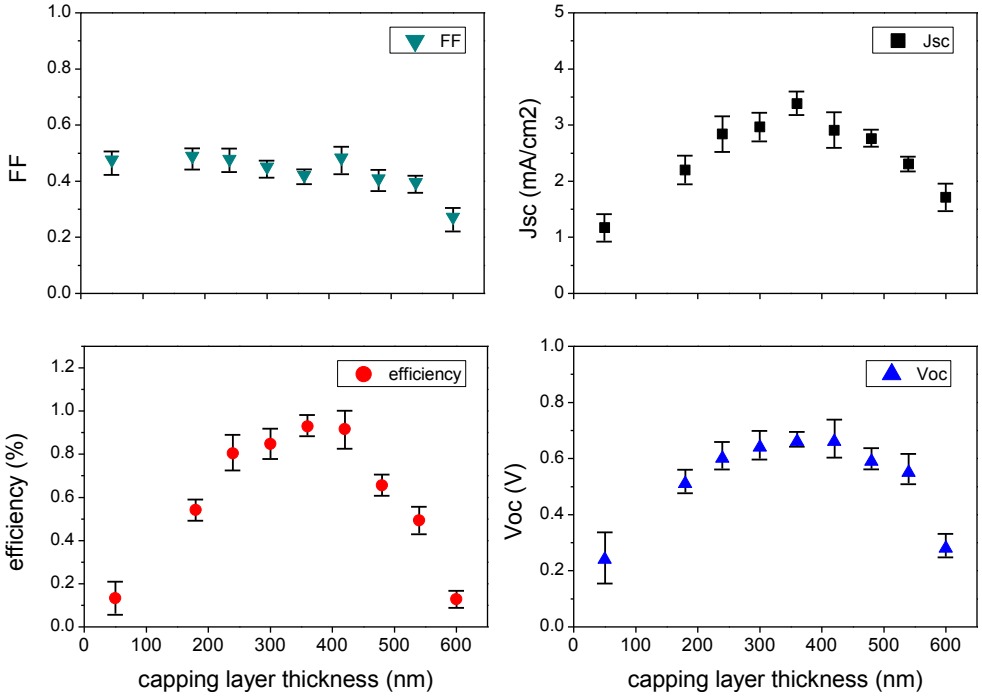

Figure 5.5: Fill factor, short circuit current density, open circuit voltage, and efficiency of SDSCs with various P3HT capping layer thicknesses.

5.2.2.3 Further Optimizations: Additives and Surface Treatments

Beyond reëngineering the cell to prevent parasitic leakage currents arising from the higher mobility replacement components, there were other more generic optimizations necessary to introduce any new material. First, we discuss selecting the appropriate amounts of additives precasted to the HTM. The concentrations of conventional additives, Li-TFSI salts and tert-butyl pyridine (TBP), were varied

on otherwise optimized cells to observe the effect on device performance. Ultimately, the optimal additives were Li-TFSI (20 mM) and TBP (60 mM) in anhydrous acetonitrile added at concentrations sufficient to leverage their advantageous effects on cell current and voltage and largely avoid parasitic effects. The effect of additive concentrations on cell performance is shown in Figure 5.6.

In accordance with previous results in the literature, increasing the concentration of TBP decreases J_{SC} but increases V_{OC}. Previous studies on TiO_2 suggest that TBP shifts the conduction band energy negatively, thus increasing the energy of conduction band electrons but decreasing injection efficiency from the dye excited state; we assume that the same phenomenon occurs with regard to the conduction band of SnO_2.[21] Conversely, addition of Li-TFSI has a unique effect on P3HT devices, elucidated by Abrusci et al.[22] They find that addition of the lithium salt redshifts the fluorescence spectrum of the dye, thus decreasing the overlap between dye emission and P3HT absorption and minimizing parasitic Förster resonant energy transfer to the P3HT. As a result, the J_{SC} should increase, and we observe this with increasing Li-TFSI concentration. Hence the optimal concentration of the additives achieves the voltage increase from TBP and enhanced current from Li-TFSI while avoiding excessive current loss from TBP's conduction band shift.

Subsequently, we proceeded to optimize the surface treatment on the SnO_2 mesostructure. Similar to previous studies of SnO_2 in SDSCs, we find that an MgO shell is an optimal surface treatment for the mesoporous SnO_2 film.[23] The results are shown in the bottom panel of Figure 5.6. Immersion in a magnesium acetate bath deposits only a few atomic layers of MgO over the SnO_2, thus passivating surface dangling bonds of SnO_2 . This passivation reduces recombination via surface traps on the SnO_2 in contact with P3HT. Other surface treatments including TiO_2 and SiO_2 and some combinations of these materials underperform the enhancement from MgO, likely because they deposit a thicker surface shell that increases series resistance of the cell and acts as a barrier to electron injection. While such an approach has proven successful in Spiro-OMeTAD based devices, it is reasonable to accept that the higher hole mobility of P3HT makes this recombination pathway less problematic.

To see why, consider the common modelling formulation explicated by Bis-

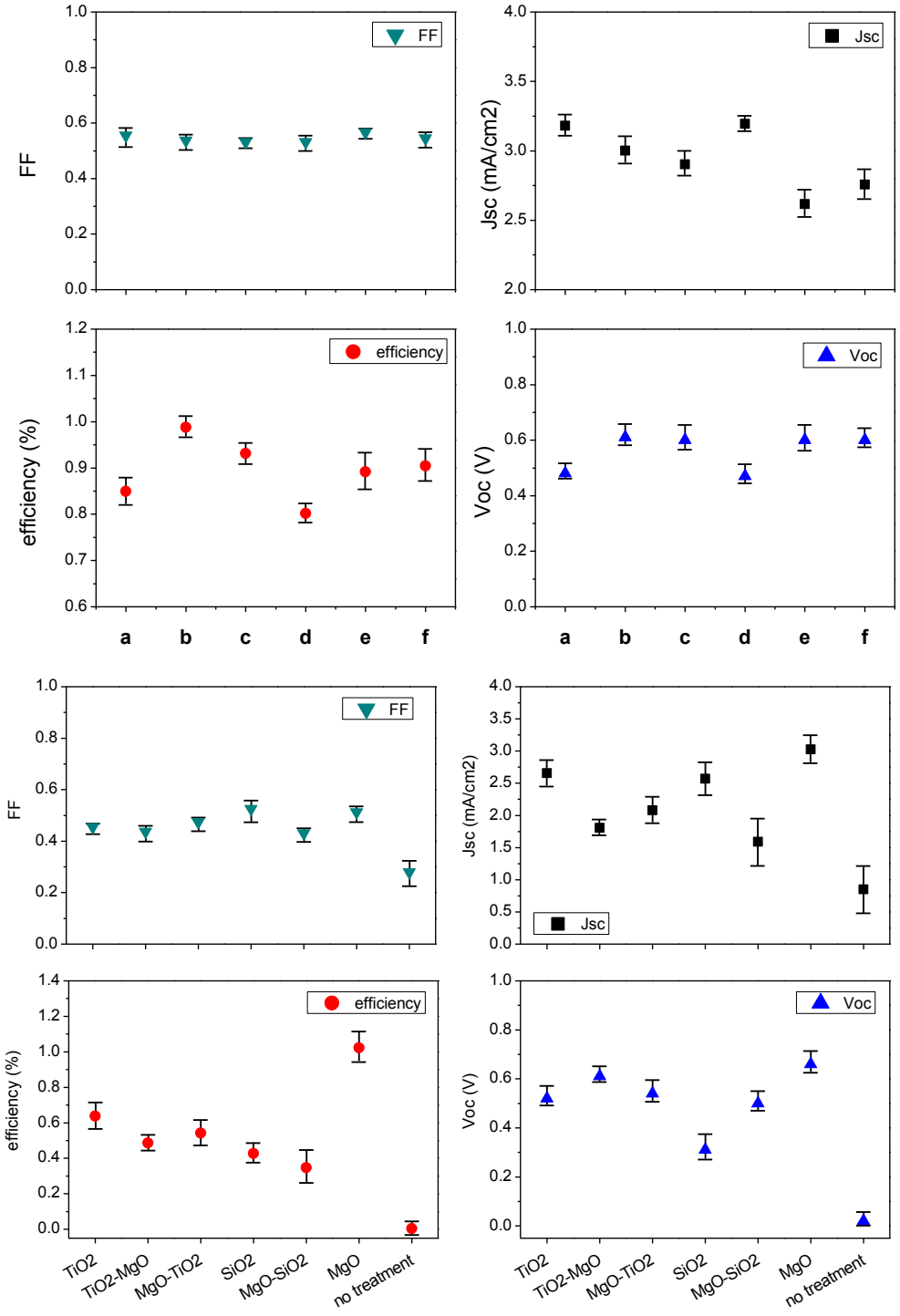

Figure 5.6: Device performance dependence on additive concentrations (top panel) and surface treatment (bottom panel). Additive variations in top panel: (a) [Li-TFSI]: 20 mM, no TBP (b) [Li-TFSI]: 20 mM, [TBP]: 60 mM, (c) [Li-TFSI]: 20 mM, [TBP]: 120 mM, (d) [Li-TFSI]: 40 mM, no TBP (e) [Li-TFSI]: 40 mM, [TBP]: 60 mM, (f) [Li-TFSI]: 40 mM, [TBP]: 120 mM.

quert et al, asserting that recombination occurs between holes in the HTM and electrons in the semiconductor conduction band or electrons trapped in surface states.[24] The probability of a mobile conduction band electron recombining with a hole is low if holes are quickly whisked away in a high mobility hole transporting medium like P3HT, resulting in a low hole density at the SnO_2 surface. Conversely, an electron trapped in a surface state has many more potential interactions with holes (assuming long detrapping times), even though holes spend less time at potential recombination sites. Thus, we expect surface trap recombination to dominate overall recombination given a higher mobility hole transporter, like P3HT. As a result, a thick shell barrier to conduction band electron recombination should offer negligible V_{OC} improvement while presenting a significant barrier to electron injection and that is exactly what we observe. An alternative explanation is that MgO shifts the surface potential of the TiO_2, increasing the conduction band electron energy and improving the open circuit voltage by 200mV.[23]

5.2.2.4 Transient Perturbation Analysis of Electron Transport

Transient photocurrent and photovoltage decay measurements bear out the hypothesis that an insufficient capping layer causes a deterioration in cell performance. Figure 5.7(a) displays the open circuit voltage decay constant for devices with thin and sufficiently thick capping layers of 50nm and 360nm, respectively. Recall that the open circuit photovoltage decay measures recombination in the solar cell, because no photoinjected electrons can leave the cell through collection, and the rate constant is described by Equation 4.13, because the charge density profile is approximately constant throughout the film.[25] We observe an effective electron lifetime, τ_n, that increases by at least two orders of magnitude as the capping layer thickness is increased to its optimized value.

Earlier, we argued that the lack of a uniform capping layer presents a leakage current route for electrons. This is equivalent to identifying a recombination pathway between electrons in the SnO_2 and holes in the P3HT via the silver electrode.

The electronic transport rate, obtained through the conventional short circuit

photocurrent and photovoltage measurements (as explained in Chapter 4), is plotted in Figure 5.7(b); it exhibits a similar trend, albeit less pronounced. The transport rate of electrons in the devices with a thin capping layer is marginally faster than that in optimized devices, indicative of electron collection both by extraction at the anode and through leakage as discussed earlier.

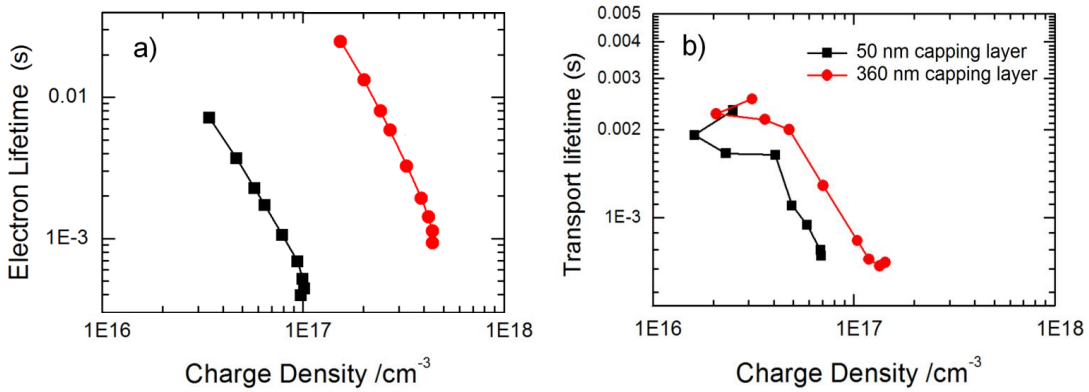

Figure 5.7: (a) Recombination lifetimes obtained through photovoltage decay lifetimes at open circuit and (b) electron transport lifetimes obtained through photocurrent and photovoltage decays at short circuit for devices with a 50 nm thick P3HT capping layer (black, squares) and a 360 nm thick P3HT capping layer (red, circles).

5.2.3 Summary

SnO_2 mesoporous films infiltrated with P3HT hole conductor were assembled, optimized, and probed for the first time, yielding device efficiencies in excess of 1%. By harnessing the intrinsically higher mobilities of SnO_2 and P3HT, this device architecture promises to boost electron lifetimes and thus efficiencies in SDSCs.

The above sections outlined optimization approaches for each process step, including a double compact layer application, two step P3HT deposition, MgO surface treatment, and addition of an optimal concentration of Li-TFSI and TBP. Each process step involved compromise between competing demands on the cells: the optimized double compact layer strikes a balance between high shunt and

low series resistance, the P3HT deposition aims to ensure a uniform and thick enough capping layer, the surface coating aims to decrease surface trap assisted recombination while retaining high current injection efficiency, and the additives increase the voltage and current of the cells.

The critical reader will note that the transport rates obtained for these devices are still electron-limited (evident from the power law decline of the transport lifetime with increasing charge density) and exhibit rate constants comparable to TiO_2/Spiro based devices.[26] Indeed, it appears the SnO_2 nanostructured photoanode is limiting ambipolar charge transport, consistent with a multiple trapping framework where trapping rate constants dominate the effective diffusion constant, and crystal mobility enhancements do not imply transport gains.

Therefore, we proceed to explore single-crystalline nanowires in the subsequent sections to fully leverage the higher mobility of different metal oxides from TiO_2. The above foray into a brand new system composed of a replacement photoanode and hole transporter serves as a model example for eventual optimization once an appropriate architecture is found.

5.3 Enhanced Charge Transport in Flexible, SnO_2 Nanowire based SDSCs

5.3.1 Background

One-dimensional, highly crystalline nanostructures have attracted considerable attention for use in DSSCs because they hold promise for faster charge transport due to lower defect concentration and higher carrier mobility.[27; 28; 29] Single crystal nanowires present additional advantages from a modeling perspective—by simplifying the mode of electron transport, one can more accurately model other phenomena in the cell that are conventionally ignored out of concern for complexity. Thus, in addition to providing new avenues for enhancing charge collection efficiencies, nanowire DSSCs are an ideal learning environment to understand cell operation.

In the preceding section, we incorporated SnO_2 as a replacement material for

TiO_2 because of its intrinsically higher mobility; while the conventionally nanostructured SnO_2 photoanode did not appear to exhibit a transport enhancement, single crystal nanowires can take advantage of the higher mobility by serving as a directional electron highway.[30] Indeed, transient perturbation methods bear out predictions of faster transport by confirming an increase in electron transport rates in ZnO nanowires.[31] SnO_2's bulk mobility is even higher than that of ZnO, but the difficulty of tuning the SnO_2 nanowire morphology has so far limited its application to DSSCs. Others have reported DSSCs combining SnO_2 nanowires and nanoparticles,[10; 32] or comprising a matrix of randomly oriented electrospun SnO_2 nanofibers,[33; 34] but to the best of our knowledge, the highest reported efficiency for a DSSC with only vertically aligned SnO_2 nanowires as the photoanode was 0.4% efficiency by Wang et al, who reported no further experimental data on charge transport rates.[35]

The drawback of using nanowires is their typically lower surface area for a given film thickness compared to the conventional mesoporous nanoparticle films; thus, nanowire based solar cells generate less current than their nanoparticle counterparts.[36] However, transient perturbation measurements require steady-state photocurrents high enough that the perturbation current decay can be considered relatively "small."[37] To ensure sufficient current, we employ perovskite absorbers, which have high extinction coefficients and are thus suitable for thin films. The efficiency of a liquid DSSC sensitized with perovskite quantum dots was reported as 6.5%,[38] and as noted above, Lee et al have recently reported efficiencies in excess of 10% in perovskite sensitized hybrid solar cells.[8]

In addition to fabricating devices, we introduce a new modeling approach which strives to include all relevant fields and carriers. Recall in Chapter 3 that almost all models in the literature, including the one-dimensional model described earlier, assume fast hole transport and ignore electric fields. Both are reasonable assumptions in liquid DSSCs with electrolytes capable of fulfilling both conditions.[39] However, in an SDSC that employs the low-mobility Spiro as the hole transporter, neither assumption is necessarily valid.[40] By constructing a full three-dimensional finite element model that accounts for electron and hole transport as well as electric fields in the device, this section introduces the nanowire solar cell as an ideal testbed for understanding previously ignored processes.

5.3.2 Experimental Results and Discussion

5.3.2.1 SnO_2 Nanowire Morphology

Figure 5.8 illustrates the effect of increasing concentration of NaCl in the nanowire growth bath. NaCl has been previously used to regulate the growth of nanowires, and it has been postulated that the molecule binds to the sides of the growing wire allowing the [001] face to grow preferentially.[41] By increasing the concentration of NaCl beyond the previously reported 3M concentration to 6M, we were able to decrease the nanowire diameter from 400nm to 150nm and create a more regularly spaced nanowire array. The length of the wires, determined from cross-sectional SEM, was between 800nm and 1μm. The clear faceting of the wires, matching the structure predicted by Vayssieres et al., is strong evidence that the wires are indeed single crystalline.[42] Furthermore, the X-ray diffraction spectrum for these wires, displayed with peaks marked in Figure 5.9, clearly matches SnO_2's reference spectrum.

5.3.2.2 Device Performance

Figure 5.10 displays device performance metrics for the SnO_2 nanowire SDSCs. Panel (a) compares the JV characteristics of cells sensitized with D102 dye, a commonly used organic dye in SDSCs,[6] with cells employing mixed halide organometallic perovskites. The perovskite cell exhibits a threefold increase in short circuit current, the driving factor behind the record 0.97% efficiency achieved on vertically aligned SnO_2 nanowires. The perovskite cell exhibits marginally lower open circuit voltage, which aligns with Im's finding that perovskites in liquid cells dramatically improve current and decrease voltage to a lesser extent.[38]

Panels (b) and (c) plot the transport lifetimes and collection efficiencies for devices fabricated from nanowires and from SnO_2 nanoparticles (the films of which were also 1μm thick) against illumination intensity. The nanowire-based devices exhibit transport between 3 and 5 times faster than their nanoparticle-based counterparts. While transport lifetimes in the nanowires remain comfortably faster than the recombination lifetimes, recombination competes with transport in the nanoparticle cell at high illumination. As a result, the collection efficiency

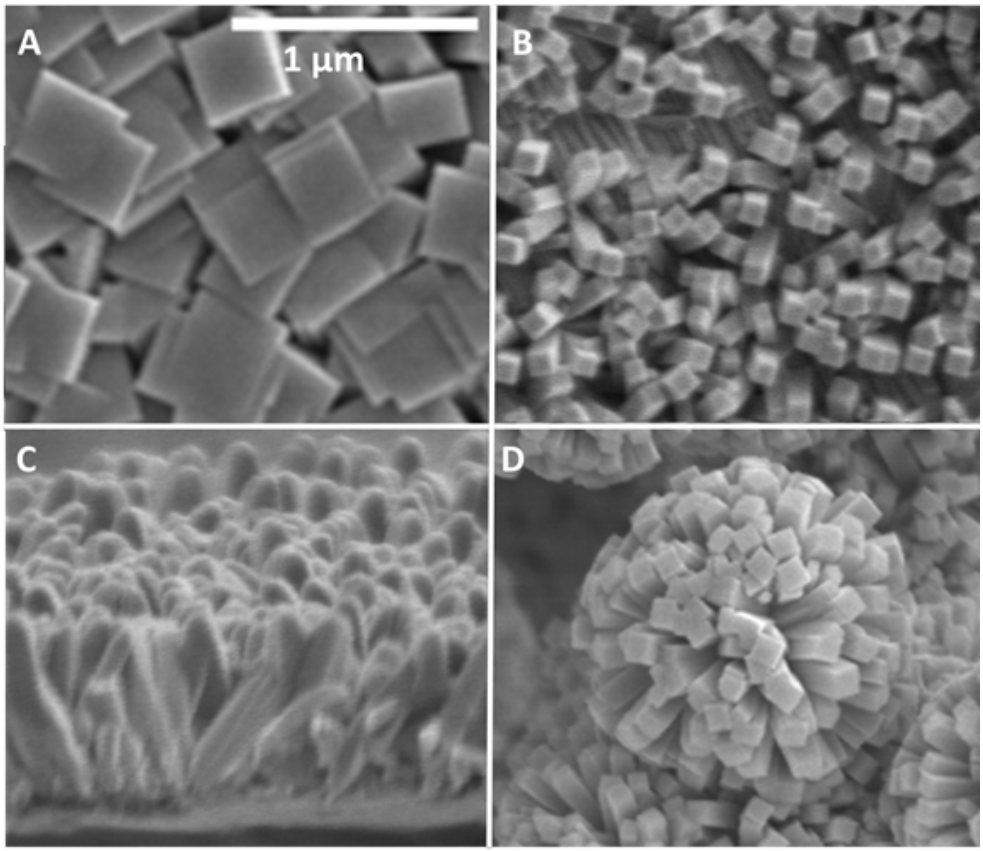

Figure 5.8: SEM micrographs of SnO_2 nanowire morphologies. A) Top view of nanowires grown with 3M NaCl. B) Top view of nanowires grown with 6M NaCl. C) Cross sectional view of rods grown with 6M NaCl. D) "Nucleation Cluster" contributing to nonuniform film thickness. Scale bar applies to all panels.

of nanowire cells is near unity for all illumination levels, compared to decreasing collection efficiency at conditions approaching 1 sun for the nanoparticle controls.

Note that while the transport lifetimes of the nanoparticle control devices tend to decrease with increasing light illumination (consistent with transport in the multiple trapping framework), the SnO_2 nanowire transport rate appears limited by the low mobility hole conductor, Spiro-OMeTAD, as reported previously.[43] Since opposite charges must be extracted at the same rate, the fruits of faster electron transport cannot be fully enjoyed until alternative hole transporting materials are integrated.[44]

Finally, panel (d) displays the density of trapped charge states for nanowire-

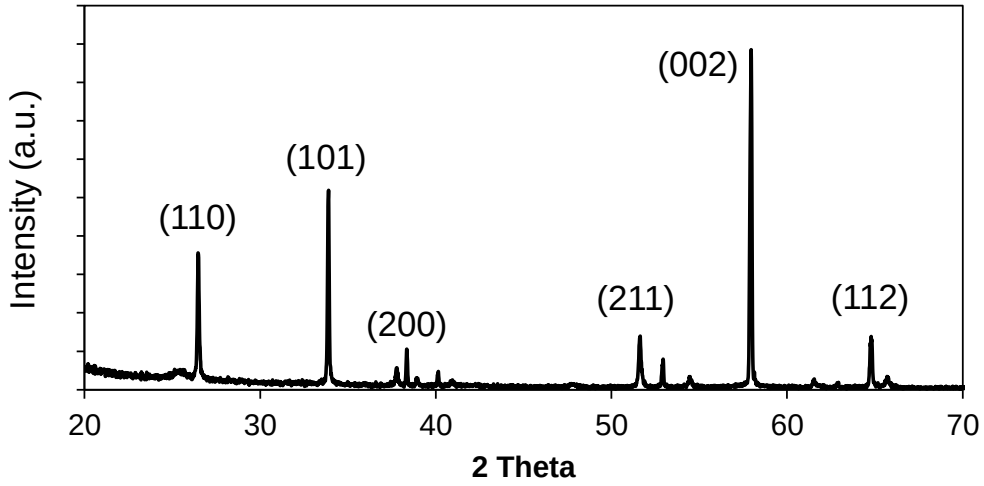

Figure 5.9: Plot of X-Ray Diffraction Intensity for SnO_2 nanowires prepared with 6M NaCl in the precursor solution. Minor, unmarked peaks correspond to FTO/Ti substrate.

based SDSCs, compared to the nanoparticle controls; the capacitance of the latter has been divided by the surface area ratio of the nanowire to nanoparticle films (the ratio is approximately an order of magnitude). The nanowire cell clearly has fewer states below the conduction band edge, and its density of states function bears resemblance to that of a single crystal; conversely, the nanoparticle cell exhibits a strong tail of sub-bandgap states, an expected result given its nanocrystalline structure.

5.3.3 3-D Finite Element Nanowire Model

5.3.3.1 Motivation

The vast majority of electrons in conventional DSSCs are trapped in localized states, and the smaller population of mobile conduction band electrons is in equilibrium with their trapped counterparts via trapping and detrapping rate constants.[45] In Chapter 3, we saw that previous models of the DSSC incorporate additional parameters to fit electron transport to the multiple-trapping diffusion framework; depending on the model complexity, these include nonlinear recombination exponents, charge-density dependent diffusion coefficients, and correction

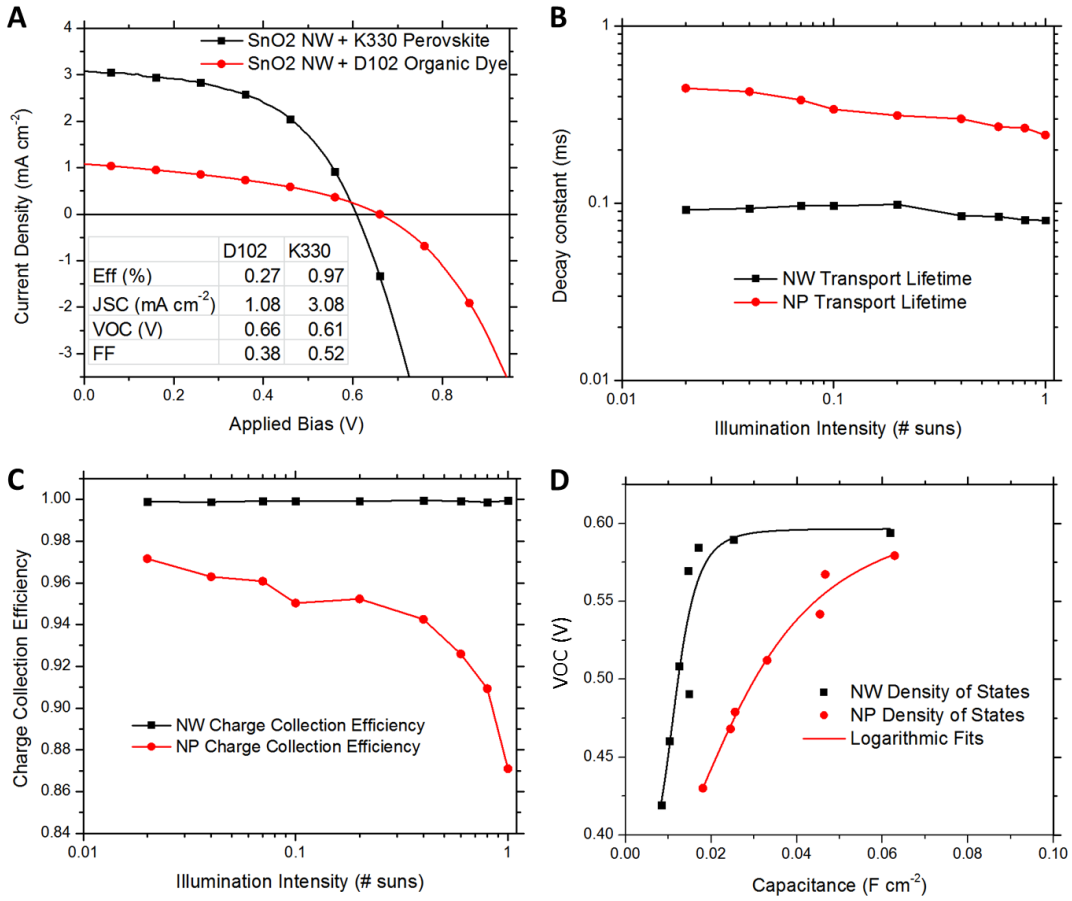

Figure 5.10: (a) JV Curves of SnO_2 Nanowire (NW) SDSCs, sensitized with D102 organic dye (red, circles) and Perovskite (black, squares); (b) Transport Lifetimes for SnO_2 NW (black, squares) and Nanoparticle (NP) control (red, circles) devices; (c) Calculated Charge Collection Efficiencies for SnO_2 NW and NP devices; (d) Density of States for SnO_2 NW and NP devices

factors for deviation from ideal diode operation.[46; 47] Because these free parameters must be fitted, incorporating drift or non-ideal electrolyte behavior is untenable. However, modeling the present SnO_2 nanowires should not require extensive modification to the basic semiconductor diffusion equations to describe charge transport because (a) single crystalline structures have fewer bulk defects than nanocrystalline counterparts, and Figure 2(d) suggests a low density of bulk and surface traps, and (b) charge transport is faster in the nanowires, suggesting that trapping processes are less of a rate-limiting factor and the equilibrium is

shifted to a more populous conduction band.

Below we proceed to introduce the model in more detail. To briefly summarize, the model aims to apply the principles of conventional semiconductor drift-diffusion in the nanowire solar cell, because, pursuant to the observations of crystallinity and low trap state density made above, the multiple trapping transport framework can be simplified in this case. The model geometry consists of a single nanowire in the middle of a unit cell, with periodic boundary conditions applied to the sides of the cell. The model assumes that electrons and holes are injected into the nanowire and surrounding Spiro-OMeTAD, respectively, at the same generation rate, and recombine at the Spiro/nanowire interface via bimolecular recombination with a single rate constant. Charge screening is not assumed, so the electron and hole continuity equations contain drift terms that depend on the potential function simultaneously solved throughout the model geometry. At the charge collecting electrodes, the boundary conditions on electrons and holes are fixed as the dark charge concentrations at a given applied potential; this simulates perfectly efficient charge extraction.

5.3.3.2 Geometry

By analyzing the SEM images of the nanowires from above and in cross-section, estimates for the dimensions of the wires and the packing factor were made. Figure 5.11(a) displays the geometry of the device, with labeled domains 1 (the nanowire) and 2 (the surrounding volume of the unit cell infiltrated by Spiro). The length units are nondimensionalized for ease of use.

Due to a jump discontinuity in charge density at the nanowire/Spiro interface, the FEM mesh was carefully chosen with finer elements at that surface; Figure 5.11(b) displays a sample mesh, but depending on the parameters, even finer meshes were sometimes implemented.

5.3.3.3 Governing equations

The model simultaneously solves three coupled differential equations for electrons, holes, and the electric potential at steady state. COMSOL uses the MUMPS linear systems algorithm to perform the computation. The following are the

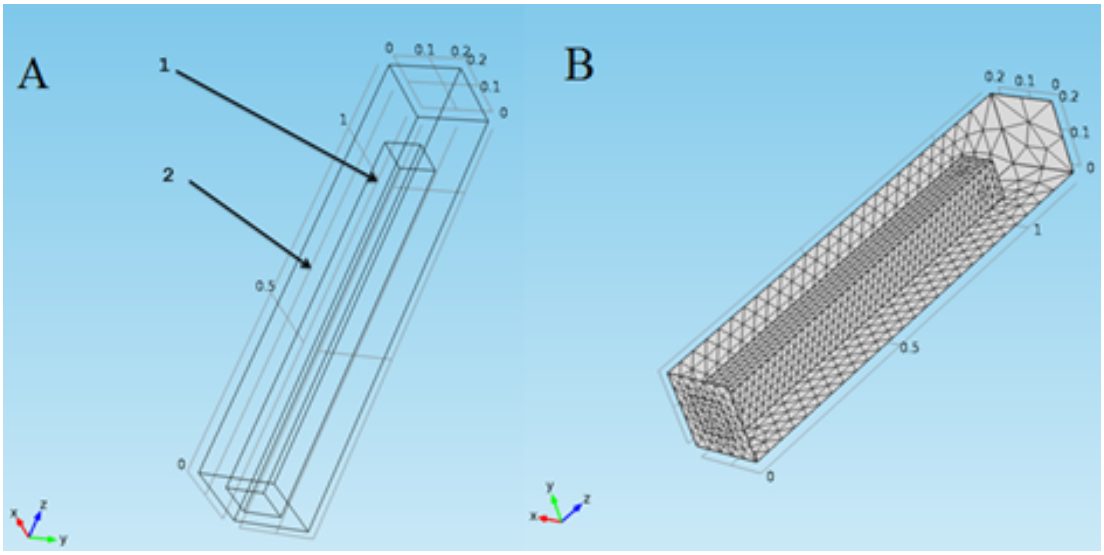

Figure 5.11: Model Geometry (a) and FEM Mesh specification (b) for the nanowire SDSC. Region 1 refers to the nanowire and Region 2 is the surrounding HTM. The model employs periodic boundary conditions.

three coupled equations:[48]

$$-\nabla \cdot (\epsilon \nabla \psi) = q(p - n) \tag{5.1}$$

$$-\nabla \cdot \mathbf{J_n} = 0 \tag{5.2}$$

$$-\nabla \cdot \mathbf{J_p} = 0 \tag{5.3}$$

where

$$\mathbf{J_n} = -qn\mu_n \nabla \psi + qD_n \nabla n \tag{5.4}$$

and

$$\mathbf{J_p} = -qp\mu_p \nabla \psi - qD_p \nabla p \tag{5.5}$$

ϵ is the medium permittivity, $\mathbf{J}_n$ and $\mathbf{J}_p$ are the electron and hole currents, respectively, q is the electronic charge, n and p are the electron and hole concentrations,

respectively, μ and D are the unipolar mobility and diffusion constant, respectively, and ψ is the electric potential.

The electron equation, 5.2, is solved only over domain 1, the hole equation, 5.3, for domain 2, and the electric potential is obtained by solving Equation 5.1 over the entire geometry. To simulate generation and recombination, an identical flux term at the nanowire/Spiro boundary was stipulated for both electrons and holes into the respective domain:

$$\Phi_{n,p} = G - K_r(np) \tag{5.6}$$

G, the generation rate, is in units of $\frac{1}{m^2 s}$ and is a composite measure of the absorption and injection efficiencies. K_r, the bimolecular recombination rate, is in units of $\frac{m^4}{s}$.

Finally, the boundary and initial conditions are as follows. At the bottom of the nanowire, the electron density is pegged at its dark value, n_0, to simulate efficient charge extraction; similarly, the hole density at the top of the unit cell is held at its dark value, p_0. The electric potential is held at zero at the top of the unit cell and at the applied potential at the bottom of the unit cell. On the sides of the unit cell, periodic boundary conditions are applied both to the electric potential and to the hole density.

5.3.3.4 Parameter Values

In a typical simulation, the following parameter values were used:

Parameter	Value
Cell thickness [m]	$1.2 \cdot 10^{-6}$
Nanowire base dimension [m]	$100 \cdot 10^{-9}$
Nanowire height [m]	$1 \cdot 10^{-6}$
Unit Cell base dimension [m]	$200 \cdot 10^{-9}$
Electron mobility $[cm^2V^{-1}s^{-1}]$	35
Hole mobility $[cm^2V^{-1}s^{-1}]$	10^{-3}
n_0 $[cm^{-3})]$	$1 \cdot 10^{19}$
p_0 $[cm^{-3})]$	$1 \cdot 10^{18}$
G $[m^{-2}s^{-1}]$	$3 \cdot 10^{21}$
K_r $[m^4s^{-1}]$	$1.5 \cdot 10^{21}$
Relative electrical permittivity, SnO_2	10
Relative electrical permittivity, Spiro	3

5.3.3.5 Comparison with Experimental Results

Figure 5.12, comparing the actual JV curve of the SnO_2 nanowire cell with simulation results from a three-dimensional model solved in COMSOL, demonstrates that such a modeling approach can generate the requisite solar cell behavior. Moreover, while the simulation results were constrained to fit the J_{SC} and V_{OC} values through adjustment of generation and recombination rates, respectively, the resultant parameter values are reasonable. We note that the fill factor is overestimated because the model did not include a series resistance term for the hole conductor, which can substantially affect the JV curve.[49]

5.3.3.6 Application of Model to Choosing Illumination Side

The model outputs visualizations of the charge densities and electric potential in the device. These are useful to understand the effect of changing parameters, such as the relative diffusion lengths of the electron and hole transporters, as well as the costs and benefits of a particular architecture. Below in Figure 5.13, we consider the example of using the model output to understand the effect of illuminating the device from the bottom or from the top at short circuit. This is an important design question; the experiments shown above were constrained to

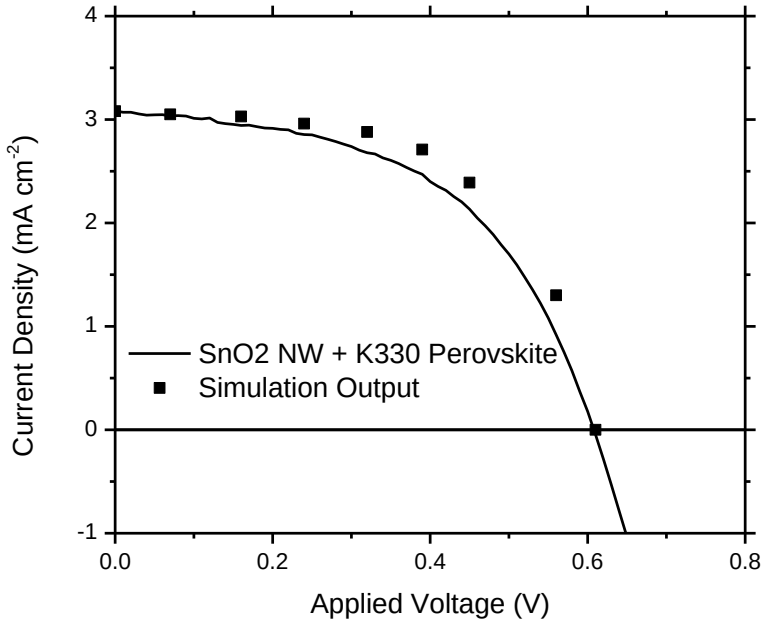

Figure 5.12: Real and simulated JV Curves of an SnO_2 nanowire SDSC sensitized with perovskite

illumination from the top because of the nontransparent Ti foil employed at the anode, but alternative growth methods on conductive glass would accommodate either architecture.

In this example, we treat generation as an exponential decay either from the top or bottom of the nanowire depending on the illumination side. The results are surprising: in panels A-C, most charge generation clearly occurs near the bottom of the nanowire, and there is actually an unfavorable electron diffusion gradient through most of the wire. Moreover, the voltage in the device is not uniformly zero at short circuit, as is widely assumed in the DSSC modeling literature, and the electron drift term is similarly unfavorable for charge collection.

Conversely, illumination from the top seems to generate the electron density gradient expected from the modeling literature. Holes are primarily generated at the top of the nanowire, as expected, and the potential landscape suggests that there is a built in field to oppose electron diffusion. This makes sense, considering that the mobility of the SnO_2 was stipulated as higher than that of Spiro, and charges must be collected at either electrode at the same rate. However, the

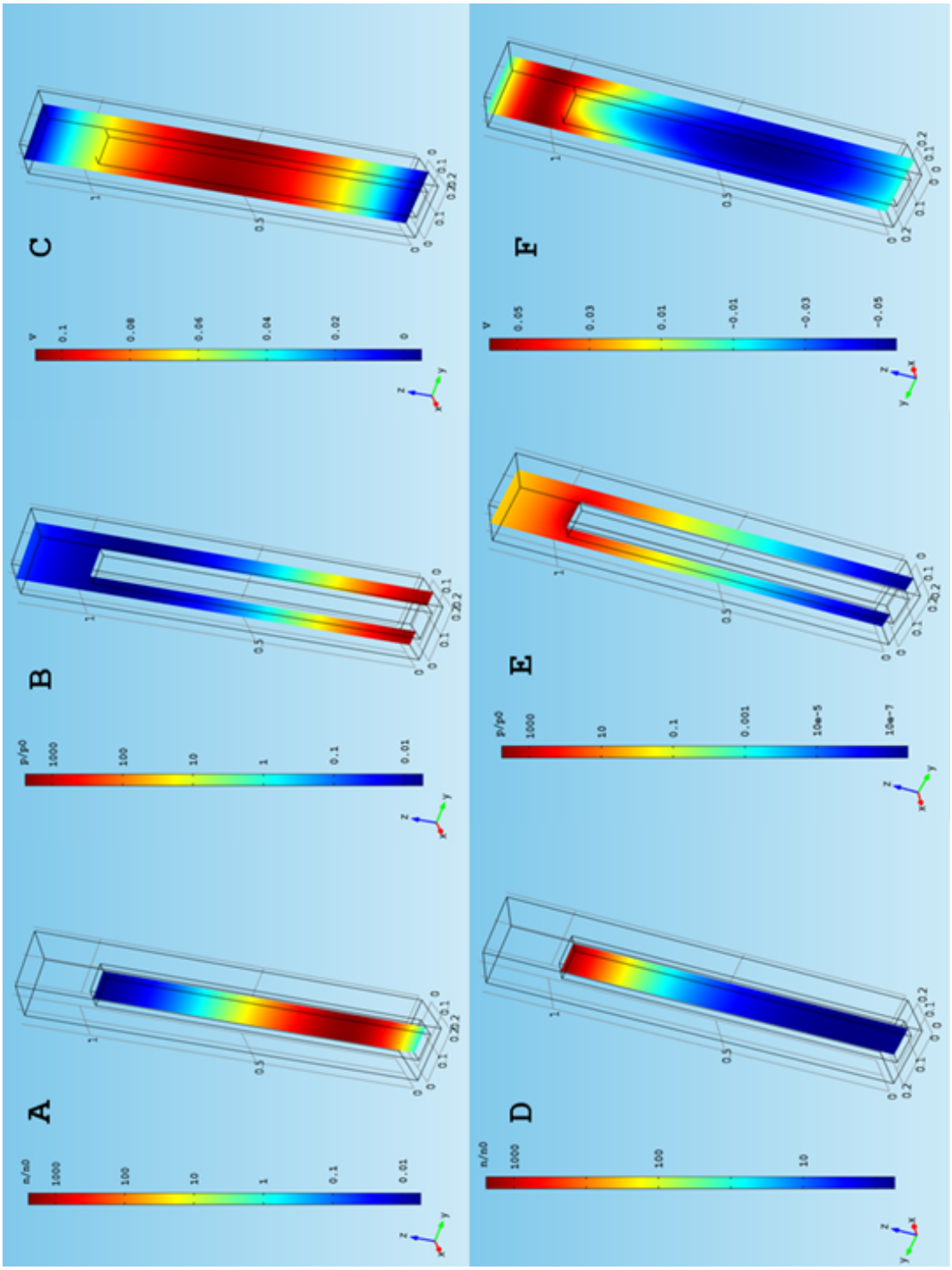

Figure 5.13: COMSOL Model Output for short circuit illumination from bottom of nanowire (panels D, E, F) and from top of nanowire (panels A, B. C). Each row of panels includes electron density, hole density, and electric potential.

potential barrier to electron transport is smaller in the top illumination case and the diffusion gradient is favorable. Given the same generation rate profile (albeit reversed depending on the illuminated side), illumination from the anode yielded around 80% of the current obtained from cathode-side illumination. This is reasonable from an intuitive standpoint—SnO_2 is a far better conductor than Spiro-OMeTAD, so it makes sense to try and generate the majority of the charge carriers close to the hole-collecting electrode; this intuition is advanced through a nuanced understanding of the coupled subprocesses occurring in the nanowire solar cell, an understanding facilitated by the numerical model.

The model presented above promises more detailed information about SDSC functioning once further material parameters are determined through experiment. Due to simplified electron diffusion, a numerical solution of three coupled differential equations for electrons, holes, and electric potential becomes tractable. The model consequently allows insights to be drawn about charge screening lengths, carrier distributions, potential landscapes, and more. Thus, SnO_2 nanowires, in addition to their potential to improve device performance, are an ideal system to probe electronic characteristics of SDSCs.

5.3.4 Summary

In this section, we combined SnO_2 nanowires with a perovskite sensitizer in an SDSC, achieving over twice the previously reported efficiency for vertically aligned SnO_2 nanowires. The cells were synthesized on flexible titanium foil substrates, suitable for unconventional photovoltaic applications.[50] By analyzing transient perturbation measurements, the nanowire devices were found to exhibit faster transport than their SnO_2 nanoparticle counterparts, and the extracted density of states agrees well with the visual evidence that the wires are single crystalline in electronic and physical structure.

Subsequently, the nanowires were used as a template for a three-dimensional computational model which generated a JV characteristic in line with actual solar cell operation. The model's versatility was demonstrated by simulating two directions of illumination and concluding that illumination from the top of the nanowire should yield superior results.

Further optimization of the SnO_2 nanowire system will certainly increase efficiencies even further, reducing the transport bottleneck that limits SDSC performance enhancements. Moreover, the modeling approach pioneered in this section can help researchers better understand the electrical characteristics of SDSCs.

5.4 Hole-Transporter Limited Transport in ZnO Nanowires Leading to Efficient SDSCs[1]

5.4.1 Background

In the previous section, we observed that SnO_2 nanowire based devices exhibited elextron transport rates independent of light intensity, and we surmised that this implies charge transport is limited by the hole transporter. In this section, we aim to investigate this hypothesis with another system, ZnO nanowires. Unlike SnO_2 nanowires, ZnO nanowires are much more amenable to hydrothermal synthesis, and there is therefore a rich literature regarding their use in solar cells. However, armed with the knowledge gained in preceding sections, we can pose the specific question of whether single crystalline nanowires formed from high mobility metal oxides result in limited enhancement to the solid state DSSC due to limitations of the hole transporter. This is not a question that arises in the liquid cell because the electrolyte hole transporter has no such limitations. However, by demonstrating a similar insensitivity to light intensity in the transport rates exhibited by ZnO nanowire devices, we can reinforce our earlier suspicion that focus on unipolar charge transport is not optimal.

We have mentioned ambipolar charge transport earlier, and now formally express the ambipolar diffusion constant as:[51]

$$D_{amb} = \frac{n+p}{\frac{p}{D_n} + \frac{n}{D_p}} \tag{5.7}$$

Thus, if either the hole number density or diffusion coefficient overwhelms that

[1]The research presented in this section arose from a collaboration with Jonathan Downing (Imperial College), who synthesized ZnO nanowires which V.S. subsequently incorporated into devices and performed characterization.

of electrons, then the ambipolar or effective diffusion coefficient will be approximately equal to the electron diffusion coefficient. This is the standard operating condition for DSSCs, except, as we suspect, in systems with highly crystalline, one-dimensional electron conductors, the tables may be turned. In the case of the electronic mobility far exceeding that of holes, the effective diffusion coefficient will now reflect the hole diffusion coefficient.

Note that Equation 5.7 was derived for conventional diffusive transport, not multiple trapping diffusion. However, without delving into modeling formalism, we can intuitively grasp that the requirement of equal charge extraction at each electrode results in an ambipolar diffusion law that behaves like Equation 5.7.[3]

There has been considerable emphasis on developing core/shell ZnO nanowires, because the performance of the devices depends heavily on the ZnO surface treatment.[52; 53; 54] Perhaps because the DSSC field has optimized dyes for operation on a TiO_2 surface (and also because the TiO_2 conduction band is closer to vacuum than that of ZnO, thus resulting in favorable energy level offsets for a core/shell structure), the conventional shell coating for ZnO nanowires is a TiO_2 shell. This shell is deposited by Atomic Layer Deposition (ALD), and significantly increases the open circuit voltage.[55]

However, researchers fabricating solid state devices have reported a solution-based route to a core/shell architecture utilizing MgO or Zr_2O_3 shells and have found smaller, though significant, performance bumps.[56] Such a chemical bath deposition method holds promise for lower cost fabrication than the ALD route, and the logical question to ask is whether a TiO_2 shell can be applied in the same manner. Unfortunately, the traditional solution-based route to applying a TiO_2 shell, using $TiCl_4$ for the surface treatment of nanocrystalline TiO_2 photoanodes in DSSCs, etches ZnO due to the acidity of the solution. We will therefore vary the solution concentration and immersion temperature to attempt to get around the damaging effects of chemical bath deposition of TiO_2 shells on ZnO nanowires. Indeed, Sakai et al. recently succeeded in applying a TiO_2 shell on nanocrystalline ZnO films by immersing the films in $TiCl_4$ solution at low temperatures, and we will adopt the same approach to coat the ZnO nanowires.[57] An alternative chemical bath deposition route to applying a TiO_2 shell was developed after the completion of this research, aiding researchers in fabricating a 5.65% cell

using 50μm ZnO nanowires (it is unclear if their TiO_2 shell is as effective as one deposited by ALD, and the sheer surface area of their long nanowires likely generated sufficient current to compensate for a subpar V_{OC}).[58]

5.4.2 Results and Discussion

5.4.2.1 Optimization of Solution-Deposited Surface Treatment

We aimed to improve ZnO nanowire based SDSC performance by applying an appropriate surface treatment to act as a recombination barrier. Others have demonstrated MgO as a simple, chemical bath deposition based route to applying a thin recombination barrier over the nanowires. We further explored coating of nanowires with ZnS, which was predicted to passivate the surface of the ZnO nanowires effectively. The reason is superb lattice matching between ZnO and ZnS, potentially enabling a heterojunction with few dangling bonds and hence few recombination centers.[59] Finally, we modified the method of Sakai et al. to apply a TiO_2 shell via immersion in a low concentration solution of $TiCl_4$ at 4°C to slow the etching process alluded to earlier (see Chapter 2).

The ZnO nanowires used in this section as photoanodes for SDSCs are displayed in Figure 5.14. The nanowires are approximately 1 μm and reasonably uniform in length distribution; the aspect ratio is over ten.

Figure 5.15 diagrams the energy levels of the core/shell architechtures investigated in this study. TiO_2 has conduction and valence band edges within ~50mV of ZnO; while it does not present a large energetic obstacle to recombination, it may function as a passivating layer as well as a more suitable binding surface for dyes designed to attach to anatase titania surfaces. MgO, a bulk insulator, actually has a smaller bandgap when fashioned into small structures, and forms a Type I heterojunction with ZnO.[60] ZnS, conversely, forms a Type II heterojunction, and the band offsets are much more pronounced. This facilitates charge separation and presents a large barrier to recombination, but also acts as a current barrier, as we will see shortly.[61]

We present the JV characteristics of the devices fabricated with different surface treatments in Figure 5.16. The MgO and ZnS devices surprisingly perform very similarly, despite the salient energy level differences. Both surface treat-

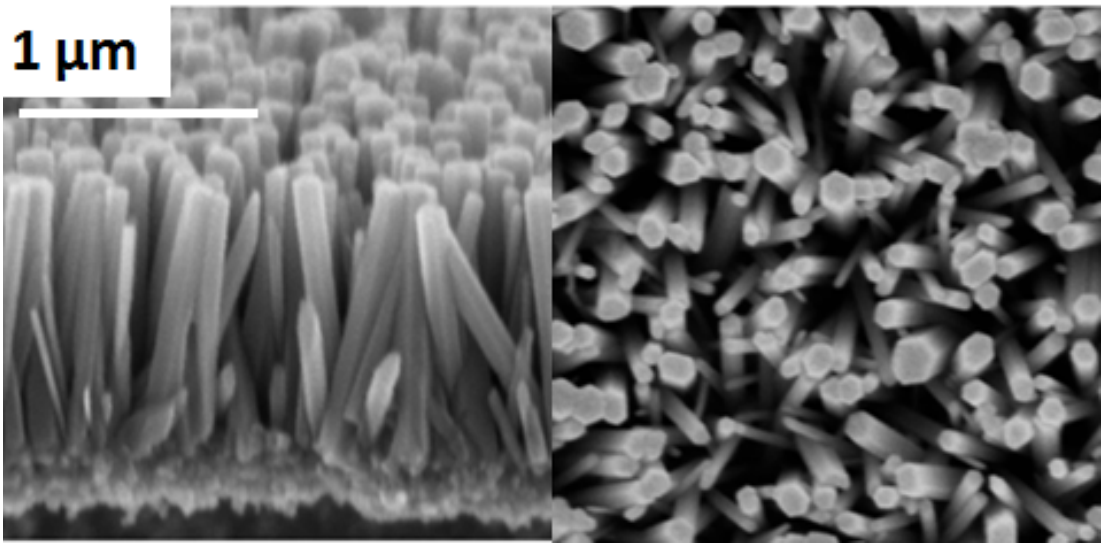

Figure 5.14: (*SEM images courtesy of Jonathan Downing, Imperial College*) SEM images of the ZnO nanowires synthesized through hydrothermal growth. Nanowires are approximately 1 μm and uniform in length.

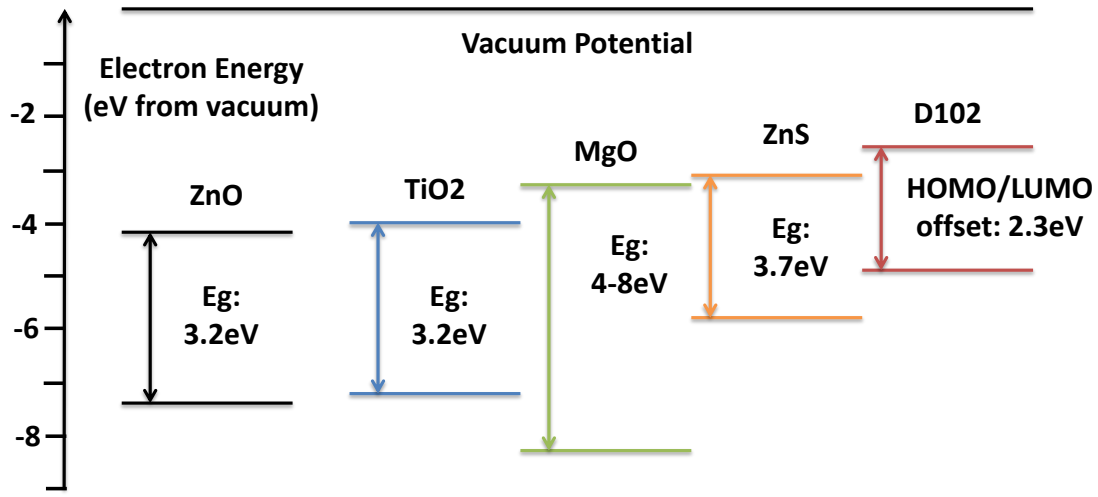

Figure 5.15: Electronic band structure diagram for the ZnO nanowires, the various shell treatments applied in this study, and the sensitizing dye used to fabricate the solar cells. The conduction and valence band are shown for semiconductors (MgO is a bulk insulator, but its bandgap shrinks in thin film applications), and the HOMO and LUMO levels are shown for the D102 dye.

ments result in low open circuit voltages, and the ZnS treatment inhibits current to a greater extent, which we predicted earlier. The TiO_2 surface treatment, however, dramatically improves the open circuit voltage of the solar cell, in line with previous reports of ALD deposition of TiO_2.[62] Apparently, the TiO_2 shell is best at passivating the ZnO surface and removing recombination centers; its value does not appear to be the provision of an energetic barrier to recombination, given the more advantageous ZnS energy levels for that purpose. The ability to form TiO_2 shells that dramatically enhance cell performance and do not require ALD deposition is a clear processability advantage of this method over previous work.

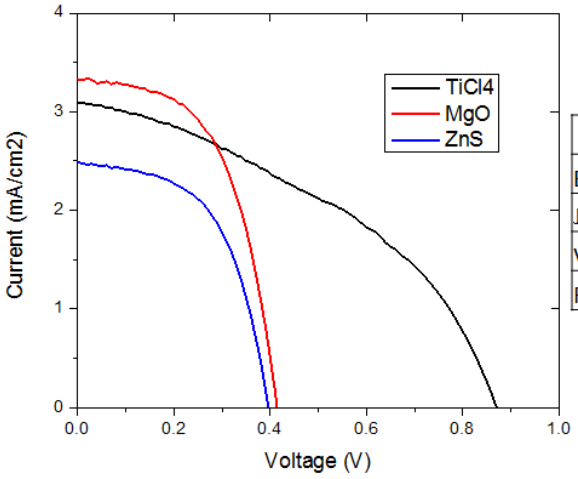

	TiCl4	MgO	ZnS
Eff(%)	1.30	0.77	0.54
JSC (mA/cm2)	3.10	3.33	2.49
VOC (V)	0.87	0.41	0.40
FF	0.48	0.56	0.54

Figure 5.16: JV characteristics for SDSCs fabricated with ZnO nanowires coated with different surface treatments: TiO_2, MgO, and ZnS; the device performance characteristics are listed in the table on the right.

5.4.2.2 Electronic Transport Properties

After optimizing the surface treatment of the ZnO nanowires, we subsequently tested the electronic transport through small perturbation transient decay methods. We present similar figures to those introduced in the SnO_2 nanowire section; Figure 5.17(a) plots the transport rate constant against light intensity, and Figure 5.17(b) plots the charge collection efficiency against light intensity for SDSCs

employing ZnO nanowires or nanoparticles as the photoanode. The nanowire transport rates exhibit complete insensitivity to light intensity, similar to the behavior of the SnO_2 nanowires investigated in the last section, while the nanoparticle films display the expected improvement in electronic transport rate as the charge density increases from illumination.

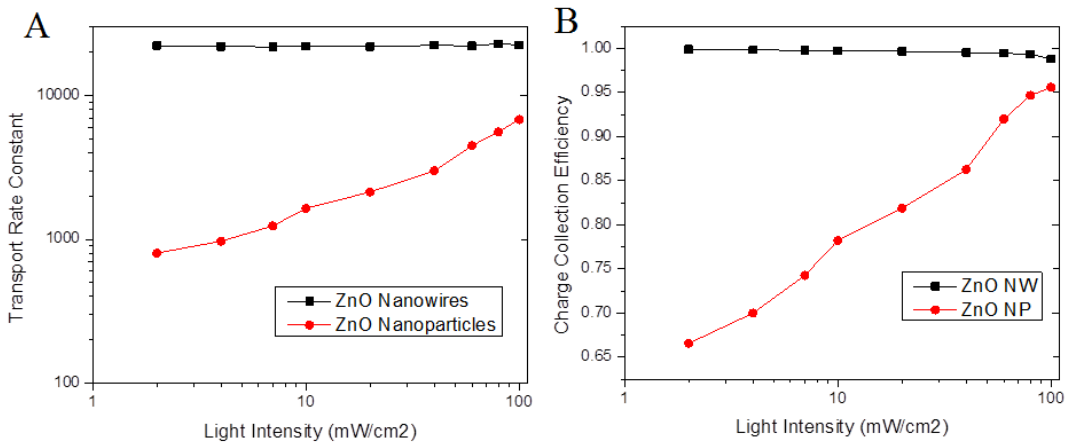

Figure 5.17: (a) Transport Rate constant as a function of light intensity plotted for SDSCs based on ZnO Nanowires and Nanoparticle films ($\sim 2\mu$m films of 40nm ZnO nanoparticles); (b) Charge Collection Efficiency calculated from the ratio of rates approximation for ZnO Nanowires and Nanoparticles as a function of light intensity.

It is instructive to recall that the charge collection efficiency is inaccurate for values below 90%, and most of the plotted points for the nanoparticle based device fall below that threshold collection efficiency. We merely point this out, because the charge collection was calculated using the heuristic approximation criticized in Chapter 3. However, it is not necessary to undergo the involved process of correcting the collection efficiencies listed for the nanoparticle device because the point of this figure is to show that the nanowire device generally exhibits perfect collection efficiency, in contrast to imperfect charge collection of nanoparticle devices. The fact that the ZnO nanoparticle devices exhibit improved charge collection efficiency at higher light intensities, in contrast to SnO_2 nanoparticle control cells investigated earlier, just has to do with the magnitude

of the recombination exponent b but does not fundamentally affect the conclusions we are making about the nanowires. Fundamentally, we have shown here, as we did with the SnO_2 nanowires, that the one-dimensional, single-crystalline architecture delivers unity charge collection efficiencies due to rapid electronic transport.

However, there is reason to believe that the charge transport is not as rapid as could be achieved with the full potential of the high mobility crystalline nanowire. This is evident from of the lack of dependence on light intensity exhibited by the transport rate. Therefore, we prepared control samples comprised of a flat compact layer of ZnO as the photoanode and varying Spiro-OMeTAD layer thicknesses to test the hole-only transport rate (the implicit assumption is that there is very rapid charge transport in the thin (∼20nm) ZnO compact layer, so the measured ambipolar transport rate will correspond to hole transport.)

Figure 5.18 displays the transport rate dependence on device charge density for these flat layer devices. The assumption of sufficiently rapid transport through the thin compact layer is borne out by the independence of transport rate on illumination level. The fit lines corresponding to the average transport rate for Spiro-OMeTAD thicknesses of 380nm to 440nm are most relevant to our study of ZnO nanowires because that is the approximate thickness of the Spiro-OMeTAD capping layer in those devices. Indeed, the transport rates observed for the flat layer devices roughly match those of ZnO nanowire devices. This further corroborates the hypothesis that the transport in nanowire based devices is limited by the hole transporting material.

Finally, to add a last piece of reinforcing evidence to this hypothesis, we sought to fabricate devices with a high mobility electron and hole transporter, combining ZnO nanowires with the higher mobility P3HT hole transporter. While the cells exhibited low power conversion efficiencies of around 0.05% (similar to previous attempts to fabricate such devices [64]), the transient decay data was very revealing. Indeed, Figure 5.19 illustrates the trace of a sample short circuit current transient decay. The decay is quite noisy because, at the microsecond time scale, it is at the limits of the oscilloscope measurement limit. However, after decomposing the function into a rapidly oscillating sinusoid modulated by an exponentially decaying envelope function, we can extract the decay constant

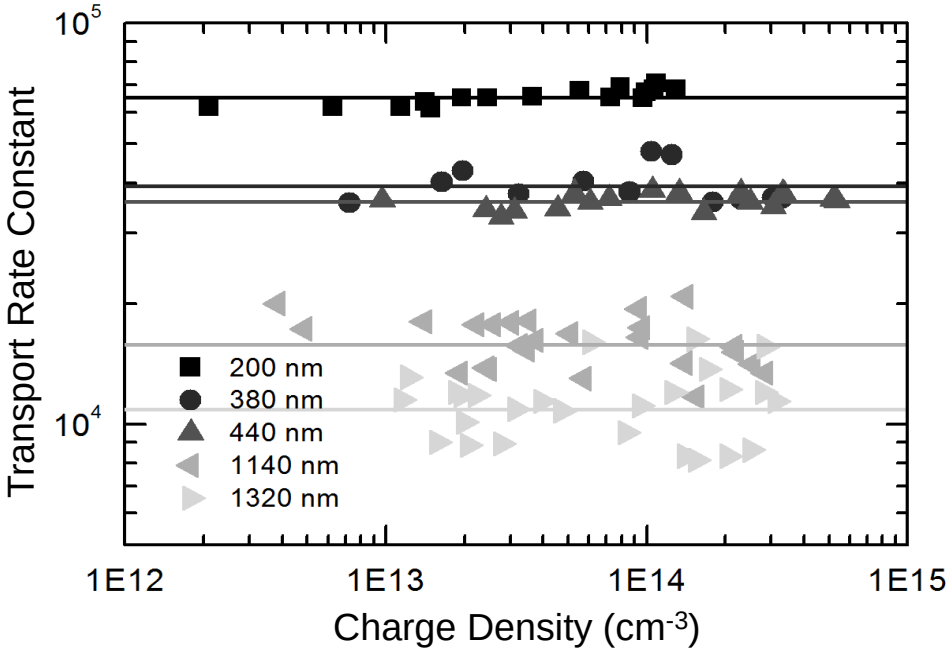

Figure 5.18: Transport rates plotted against charge density for flat layer devices consisting of a dye-sensitized ZnO compact layer of ∼20 nm in thickness for a range of Spiro-OMeTAD thicknesses (see legend). Points shown correspond to at least 3 different devices. Flat lines correspond to the average of the measured data points. Reprinted with permission from [63].

corresponding to that envelope function. The value of the decay constant in Figure 5.19 is 2.79×10^{-6} and corresponds to illumination at 0.6 suns. At full sun illumination, that decay rate grows to 4.12×10^{-6}; however, there are significant errors in the calculation of the decay rate of the exponential envelope considering the noise in the measurement, so we refrain from making any conclusion about the light intensity dependence of the current decay rates.

Nevertheless, the timescale for these decays is over an order of magnitude faster than that observed for the devices employing ZnO nanowires and Spiro as the hole transporting material. Moreover, the short circuit voltage transient decay is over two orders of magnitude slower than the current decay, which means that the transport rate is roughly equal to the decay constants calculated above, and the collection efficiency is a reliable figure near unity.

It appears, therefore, that we can indeed improve charge transport rates by

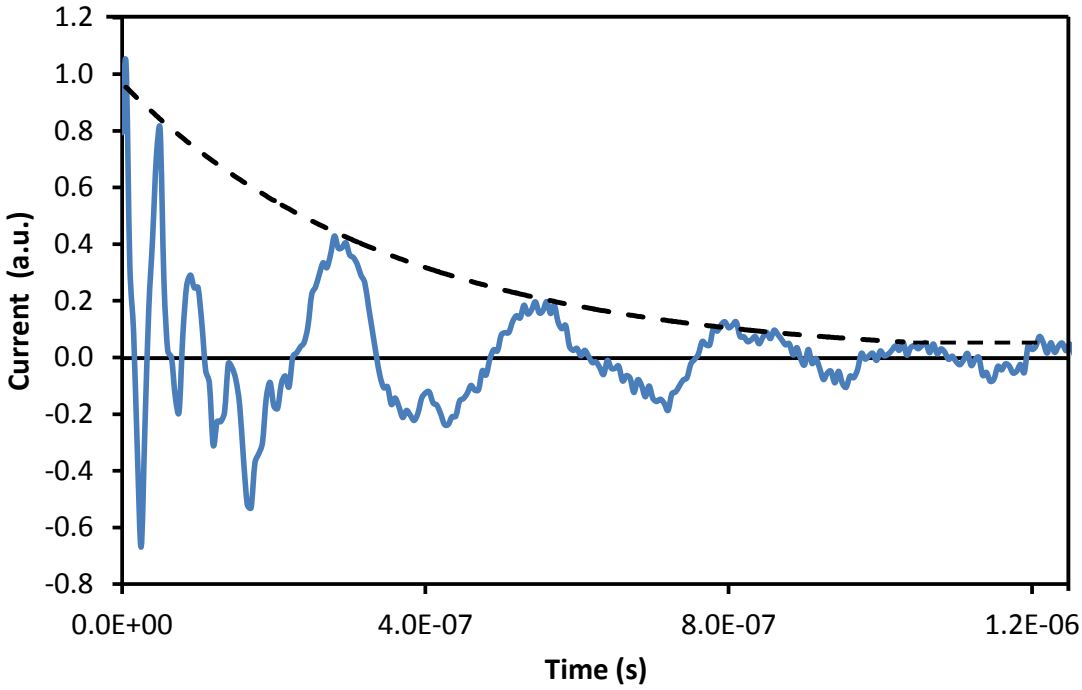

Figure 5.19: Trace of the short circuit current transient decay following a small perturbation for an SDSC comprising ZnO nanowires and P3HT hole transporter. The decay was fitted by applying an envelope function to the modulated sinusoidal signal, an artifact of the decay timescale being at the measurement limit of the instrumentation.

improving the hole transporter mobility. It remains to be seen whether the P3HT or ZnO is the limiting material now; the noisy data above suggests that the latter, the electron conductor, is once again the limiting material, but this is far from certain. Regardless, the transport rate, on the microsecond scale, is faster than anything ever reported in the literature and could hold the key to solving the charge transport problem to SDSCs. To keep things in perspective, the cell efficiency needs to improve by a few orders of magnitude, but these results are promising not just because they cement suspicions of the rate limiting behavior of the hole transporter.

5.5 Concluding Remarks

In this Chapter, we came full circle, first fabricating SnO_2-P3HT devices under the hypothesis that truly enhanced charge transport requires higher mobility electron and hole conductors and ending with a tentative conclusion that material and architectural modifications to the electron conductor require corresponding modifications to the hole conductor. The reason is that ambipolar diffusion limits the gains that can be made by collecting charge on either electrode, holding the other constant.

Although we have not translated transport rate gains into superior device efficiencies, this Chapter has presented significant accomplishments and lays out a clear narrative arc waiting for a sequel. By fabricating the first stable SnO_2-P3HT SDSCs, we demonstrated that the conventional materials upon which the SDSC is currently based need not be static. Rather, by ensuring that unipolar leakage currents at both ends of the device are suppressed via new compact and capping layer deposition methods, we overcame challenges associated with higher mobility materials. Additionally, we report on more generic optimization of additives and surface treatments that will characterize incorporation of any new material in the SDSC.

However, the devices did not live up to the promise of their higher mobility components, likely because multiple trapping diffusion still characterized electronic transport. The free electron diffusion constant may well have been faster, but the overall transport rate was limited by trapping/detrapping processes. Therefore, we endeavored to synthesize one dimensional nanostructures (nanowires) in which charge transport was not governed by the multiple trapping paradigm. We found such behavior in a flexible, SnO_2 nanowire system, the most efficient of its class. In addition to the device performance bottom line, we found these devices promising from a processability as well as a modelling point of view. The latter consideration arises from the simpler diffusive processes in the single-crystalline nanowire system that allow us to add three-dimensional drift terms to the governing equations. Use of such a simulation approach allowed reproduction of the device JV curve along with the production of evidence that top-side illumination is more effective than bottom-side illumination.

Further investigation into the one-dimensional photoanode based device architecture led us to seek a new method for treating the surface of ZnO nanowires. To arrive at a solution-based method to apply a TiO_2 shell on ZnO nanowires, essential for roll-to-roll processing, we employed low-temperature immersion in a $TiCl_4$ solution normally damaging to the ZnO. Upon confirming voltage and efficiency gains, we sought to understand the apparent limitations on electronic transport that we observed in both SnO_2 and ZnO nanowire systems. We hypothesized that the limitation, evident from transport rate insensitivity to light intensity, arose from the hole transporter which had been held constant in contrast to an enhanced photoanode for charge transport. By comparing the constant transport rates to those in a device with a thin compact layer, we confirmed this hypothesis. Subsequently, we investigated a device architecture which combined high mobility ZnO nanowires with P3HT and observed rapid transport, detection of which was at the edge of our instrumentation's ability.

Although we were unsuccessful in fabricating devices with respectable power conversion efficiency based on ZnO nanowires and P3HT, we strongly suspect that this is a surmountable engineering challenge. Our initial optimization of the SnO_2-P3HT devices instantiated an optimization process for incorporation of new materials, the general outlines of which will likely be followed in the future to fabricate efficient devices based on nanowires and a higher mobility hole transporter. We stress that the observed enhancements in charge transport from this Chapter, while not yet translatable to superior device efficiency, indeed are promising because of the centrality of charge transport to improving SDSCs. Because of the thickness limitation of conventional nanostructures and materials, the absorption of SDSCs will not improve until these higher mobility replacements are effectively incorporated into devices; our work demonstrates that the optimization is warranted due to early indications of enhanced transport.

5.6 References

[1] Brian O'Regan and Michael Gratzel. A low-cost, high-efficiency solar cell based on dye-sensitized colloidal TiO2 films. *Nature*, 353(6346):737–740, October 1991. 90

[2] B.E. Hardin, H.J. Snaith, and M.D. McGehee. The renaissance of dye-sensitized solar cells. *Nature Photonics*, 6(3):162–169, 2012. 90

[3] R.D McConnell. Assessment of the dye-sensitized solar cell. *Renewable and Sustainable Energy Reviews*, 6(3):271 – 293, 2002. 90, 118

[4] H.J. Snaith and M. Gratzel. Electron and hole transport through mesoporous TiO2 infiltrated with Spiro-MeOTAD. *Advanced Materials*, 19(21):3643–3647, 2007. 90

[5] John Melas-Kyriazi, I-Kang Ding, Arianna Marchioro, Angela Punzi, Brian E. Hardin, George F. Burkhard, Nicolas Tatreault, Michael Gratzel, Jacques-E. Moser, and Michael D. McGehee. The effect of hole transport material pore filling on photovoltaic performance in solid-state dye-sensitized solar cells. *Advanced Energy Materials*, 1(3):407–414, 2011. 90

[6] H.J. Snaith and L. Schmidt-Mende. Advances in liquid-electrolyte and solid-state dye-sensitized solar cells. *Advanced Materials*, 19(20):3187–3200, 2007. 90, 106

[7] Henry J Snaith, Robin Humphry-Baker, Peter Chen, Ilkay Cesar, Shaik M Zakeeruddin, and Michael Gratzel. Charge collection and pore filling in solid-state dye-sensitized solar cells. *Nanotechnology*, 19(42):424003–, 2008. 91

[8] Michael Lee and Henry Snaith. 10 percent efficient solar cells consisting of perovskite-sensitized mesoporous alumina infiltrated with a solid state hole transporter. 91, 105

[9] D.C. Look, D.C. Reynolds, J.R. Sizelove, R.L. Jones, C.W. Litton, G. Cantwell, and W.C. Harsch. Electrical properties of bulk ZnO. *Solid State Communications*, 105(6):399 – 401, 1998. 91

[10] Suresh Gubbala, Vidhya Chakrapani, Vivekanand Kumar, and Mahendra K. Sunkara. Band-edge engineered hybrid structures for dye-sensitized solar cells based on SnO2 nanowires. *Adv. Funct. Mater.*, 18(16):2411–2418, 2008. 91, 105

[11] Rajan Jose, Velmurugan Thavasi, and Seeram Ramakrishna. Metal oxides for dye-sensitized solar cells. *Journal of the American Ceramic Society*, 92(2):289–301, 2009. 91

[12] Golnaz Sadoughi, Varun Sivaram, Robbert Gunning, Pablo Docampo, Ingmar Bruder, Neil Pschirer, Azam Irajizad, and Henry J. Snaith. Enhanced electronic contacts in SnO2-dye-P3HT based solid state dye sensitized solar cells. *Phys. Chem. Chem. Phys.*, 15:2075–2080, 2013. 92

[13] Francisco Fabregat-Santiago, Juan Bisquert, Le Cevey, Peter Chen, Mingkui Wang, Shaik M. Zakeeruddin, and Michael Gratzel. Electron transport and recombination in solid-state dye solar cell with Spiro-OMeTAD as hole conductor. *Journal of the American Chemical Society*, 131(2):558–562, 2009. PMID: 19140794. 92

[14] ZM Jarzebski and JP Morton. Physical properties of SnO2 materials ii. electronic properties. *Journal of the electrochemical Society*, 123(10):333C–346C, 1976. 92

[15] Priti Tiwana, Pablo Docampo, Michael B. Johnston, Henry J. Snaith, and Laura M. Herz. Electron mobility and injection dynamics in mesoporous ZnO, SnO2, and TiO2 films used in dye-sensitized solar cells. *ACS Nano*, 5(6):5158–5166, May 2011. 92

[16] Wei Zhang, Rui Zhu, Feng Li, Qing Wang, and Bin Liu. High-performance solid-state organic dye sensitized solar cells with P3HT as hole transporter. *J. Phys. Chem. C*, 115(14):7038–7043, March 2011. 92

[17] He Tian, Pei-Hua Liu, Weihong Zhu, Enqin Gao, Da-Jun Wu, and Sengmin Cai. Synthesis of novel multi-chromophoric soluble perylene derivatives and their photosensitizing properties with wide spectral response for SnO2 nanoporous electrode. *J. Mater. Chem.*, 10:2708–2715, 2000. 92

[18] Y. Kim, S. Cook, S.M. Tuladhar, S.A. Choulis, J. Nelson, J.R. Durrant, D.D.C. Bradley, M. Giles, I. McCulloch, C.S. Ha, et al. A strong regioregularity effect in self-organizing conjugated polymer films and high-efficiency

polythiophene: fullerene solar cells. *Nature Materials*, 5(3):197–203, 2006. 93

[19] Nicola Humphry-Baker, Kristina Driscoll, Akshay Rao, Tomas Torres, Henry J. Snaith, and Richard H. Friend. Time-evolution of Poly(3-Hexylthiophene) as an energy relay dye in dye-sensitized solar cells. *Nano Letters*, 12(2):634–639, 2012. 93

[20] Pablo Docampo and Henry J. Snaith. Obviating the requirement for oxygen in SnO2-based solid-state dye-sensitized solar cells. *Nanotechnology*, 22(22):225403–225410, 2011. 98

[21] Xiong Yin, Hui Zhao, Liping Chen, Weiwei Tan, Jingbo Zhang, Yuxiang Weng, Zhigang Shuai, Xurui Xiao, Xiaowen Zhou, Xueping Li, and Yuan Lin. The effects of pyridine derivative additives on interface processes at nanocrystalline TiO2 thin film in dye-sensitized solar cells. *Surface and Interface Analysis*, 39(10):809–816, 2007. 100

[22] Agnese Abrusci, R. Sai Santosh Kumar, Mohammed Al-Hashimi, Martin Heeney, Annamaria Petrozza, and Henry J. Snaith. Influence of ion induced local coulomb field and polarity on charge generation and efficiency in Poly(3-Hexylthiophene)-based solid-state dye-sensitized solar cells. *Advanced Functional Materials*, 21(13):2571–2579, 2011. 100

[23] Pablo Docampo, Priti Tiwana, Nobuya Sakai, Hidetoshi Miura, Laura Herz, Takurou Murakami, and Henry J. Snaith. Unraveling the function of an MgO interlayer in both electrolyte and solid-state SnO2 based dye-sensitized solar cells. *The Journal of Physical Chemistry C*, 116(43):22840–22846, 2012. 100, 102

[24] Juan Bisquert, Arie Zaban, Miri Greenshtein, and Ivan Mora-Sero. Determination of rate constants for charge transfer and the distribution of semiconductor and electrolyte electronic energy levels in dye-sensitized solar cells by open-circuit photovoltage decay method. *J. Am. Chem. Soc.*, 126(41):13550–13559, September 2004. 102

[25] Arie Zaban, Miri Greenshtein, and Juan Bisquert. Determination of the electron lifetime in nanocrystalline dye solar cells by open-circuit voltage decay measurements. *ChemPhysChem*, 4(8):859–864, 2003. 102

[26] Nikos Kopidakis, Kurt D. Benkstein, Jao van de Lagemaat, and Arthur J. Frank. Transport-limited recombination of photocarriers in dye-sensitized nanocrystalline TiO2 solar cells. *The Journal of Physical Chemistry B*, 107(41):11307–11315, 2003. 104

[27] Jason B. Baxter and Eray S. Aydil. Nanowire-based dye-sensitized solar cells. *Applied Physics Letters*, 86(5):053114, 2005. 104

[28] Lori E. Greene, Matt Law, Dawud H. Tan, Max Montano, Josh Goldberger, Gabor Somorjai, and Peidong Yang. General route to vertical ZnO nanowire arrays using textured ZnO seeds. *Nano Lett.*, 5(7):1231–1236, June 2005. 104

[29] Gopal K. Mor, Karthik Shankar, Maggie Paulose, Oomman K. Varghese, and Craig A. Grimes. Use of highly-ordered TiO2 nanotube arrays in dye-sensitized solar cells. *Nano Lett.*, 6(2):215–218, December 2005. 104

[30] Matt Law, Lori E. Greene, Justin C. Johnson, Richard Saykally, and Peidong Yang. Nanowire dye-sensitized solar cells. *Nat Mater*, 4(6):455–459, June 2005. 105

[31] Elena Galoppini, Jonathan Rochford, Hanhong Chen, Gaurav Saraf, Yicheng Lu, Anders Hagfeldt, and Gerrit Boschloo. Fast electron transport in metal organic vapor deposition grown dye-sensitized ZnO nanorod solar cells. *J. Phys. Chem. B*, 110(33):16159–16161, August 2006. 105

[32] Thirumal Krishnamoorthy, Mu Zhi Tang, Akshara Verma, A. Sreekumaran Nair, Damian Pliszka, Subodh G. Mhaisalkar, and Seeram Ramakrishna. A facile route to vertically aligned electrospun SnO2 nanowires on a transparent conducting oxide substrate for dye-sensitized solar cells. *J. Mater. Chem.*, 22(5):2166–2172, 2012. 105

[33] T. Krishnamoorthy, M.Z. Tang, A. Verma, A.S. Nair, D. Pliszka, S.G. Mhaisalkar, and S. Ramakrishna. A facile route to vertically aligned electrospun sno2 nanowires on a transparent conducting oxide substrate for dye-sensitized solar cells. *Journal of Materials Chemistry*, 22(5):2166–2172, 2012. 105

[34] N.K. Elumalai, R. Jose, P.S. Archana, V. Chellappan, and S. Ramakrishna. Charge transport through electrospun SnO2 nanoflowers and nanofibers: Role of surface trap density on electron transport dynamics. *The Journal of Physical Chemistry C*, 2012. 105

[35] Ya-Li Wang, Min Guo, Mei Zhang, and Xi-Dong Wang. Hydrothermal preparation and photoelectrochemical performance of size-controlled SnO2 nanorod arrays. *CrystEngComm*, 12(12):4024–4027, 2010. 105

[36] Jih-Jen Wu, Guan-Ren Chen, Hung-Hsien Yang, Chen-Hao Ku, and Jr-Yuan Lai. Effects of dye adsorption on the electron transport properties in ZnO-nanowire dye-sensitized solar cells. *Appl. Phys. Lett.*, 90(21):213109–3, May 2007. 105

[37] Juan Bisquert and Ivan Mora-Sero. Simulation of steady-state characteristics of dye-sensitized solar cells and the interpretation of the diffusion length. *J. Phys. Chem. Lett.*, 1(1):450–456, December 2009. 105

[38] Jeong-Hyeok Im, Chang-Ryul Lee, Jin-Wook Lee, Sang-Won Park, and Nam-Gyu Park. 6.5 *Nanoscale*, 3(10):4088–4093, 2011. 105, 106

[39] Juan A. Anta, Fabiola Casanueva, and Gerko Oskam. A numerical model for charge transport and recombination in dye-sensitized solar cells. *J. Phys. Chem. B*, 110(11):5372–5378, March 2006. 105

[40] Brian C. O'Regan and Frank Lenzmann. Charge transport and recombination in a nanoscale interpenetrating network of n-type and p-type semiconductors: Transient photocurrent and photovoltage studies of TiO2/Dye/CuSCN photovoltaic cells. *J. Phys. Chem. B*, 108(14):4342–4350, March 2004. 105

[41] Yali Wang, Min Guo, Mei Zhang, and Xidong Wang. Facile synthesis of SnO2 nanograss array films by hydrothermal method. *Thin Solid Films*, 518(18):5098–5103, July 2010. 106

[42] Lionel Vayssieres and Michael Graetzel. Highly ordered SnO2 nanorod arrays from controlled aqueous growth. *Angewandte Chemie*, 116(28):3752–3756, 2004. 106

[43] Pablo Docampo, Stefan Guldin, Morgan Stefik, Priti Tiwana, M. Christopher Orilall, Sven Hattner, Hiroaki Sai, Ulrich Wiesner, Ulrich Steiner, and Henry J. Snaith. Control of solid-state dye-sensitized solar cell performance by block-copolymer-directed TiO2 synthesis. *Adv. Funct. Mater.*, 20(11):1787–1796, 2010. 107

[44] Tomas Leijtens, I-Kang Ding, Tommaso Giovenzana, Jason T. Bloking, Michael D. McGehee, and Alan Sellinger. Hole transport materials with low glass transition temperatures and high solubility for application in solid-state dye-sensitized solar cells. *ACS Nano*, 6(2):1455–1462, January 2012. 107

[45] Juan Bisquert and Vyacheslav S. Vikhrenko. Interpretation of the time constants measured by kinetic techniques in nanostructured semiconductor electrodes and dye-sensitized solar cells. *The Journal of Physical Chemistry B*, 108(7):2313–2322, 2004. 108

[46] Piers R. F. Barnes, Assaf Y. Anderson, James R. Durrant, and Brian C. O'Regan. Simulation and measurement of complete dye sensitised solar cells: including the influence of trapping, electrolyte, oxidised dyes and light intensity on steady state and transient device behaviour. *Phys. Chem. Chem. Phys.*, 13(13):5798–5816, 2011. 109

[47] J. Villanueva-Cab, G. Oskam, and J.A. Anta. A simple numerical model for the charge transport and recombination properties of dye-sensitized solar cells: A comparison of transport-limited and transfer-limited recombination. *Solar Energy Materials and Solar Cells*, 94(1):45–50, January 2010. 109

[48] R.F. Pierret. *Advanced semiconductor fundamentals*. Modular series on solid state devices. Addison-Wesley Pub. Co., 1987. 111

[49] Sandeep Pathak Jol Teuscher Roberto Avolio James Kirkpatrick Pablo Docampo Maria E. Errico Ian McPherson Antonio Abate, Tomas Leijtens and 2012). Henry J. Snaith. Lithium and dye sensitized solar cells. 2012. 113

[50] Mario Pagliaro, Rosaria Ciriminna, and Giovanni Palmisano. Flexible solar cells. *ChemSusChem*, 1(11):880–891, 2008. 116

[51] S.M. Sze and K.K. Ng. *Physics of Semiconductor Devices*. John Wiley & Sons, 2006. 117

[52] Qifeng Zhang, Christopher S. Dandeneau, Xiaoyuan Zhou, and Guozhong Cao. ZnO nanostructures for dye-sensitized solar cells. *Advanced Materials*, 21(41):4087–4108, 2009. 118

[53] Youngjo Tak, Suk Joon Hong, Jae Sung Lee, and Kijung Yong. Fabrication of ZnO/CdS core/shell nanowire arrays for efficient solar energy conversion. *J. Mater. Chem.*, 19:5945–5951, 2009. 118

[54] Kai Wang, Jiajun Chen, Weilie Zhou, Yong Zhang, Yanfa Yan, John Pern, and Angelo Mascarenhas. Direct growth of highly mismatched type ii ZnO/ZnSe core/shell nanowire arrays on transparent conducting oxide substrates for solar cell applications. *Advanced Materials*, 20(17):3248–3253, 2008. 118

[55] Matt Law, Lori E. Greene, Aleksandra Radenovic, Tevye Kuykendall, Jan Liphardt, and Peidong Yang. ZnO/Al2O3 and ZnO/TiO2 core/shell nanowire dye-sensitized solar cells. *The Journal of Physical Chemistry B*, 110(45):22652–22663, 2006. PMID: 17092013. 118

[56] Natalie O. V. Plank, Ian Howard, Akshay Rao, Mark W. B. Wilson, Caterina Ducati, Rajaram Sakharam Mane, James S. Bendall, Rami R. M. Louca, Neil C. Greenham, Hidetoshi Miura, Richard H. Friend, Henry J. Snaith, and Mark E. Welland. Efficient ZnO nanowire solid-state dye-sensitized

solar cells using organic dyes and core/shell nanostructures. *The Journal of Physical Chemistry C*, 113(43):18515–18522, 2009. 118

[57] N. Sakai, N. Kawashima, and T.N. Murakami. Effect of ticl4 treatment on porous ZnO photoelectrodes for dye-sensitized solar cells. *Chemistry Letters*, 40(2):162–164, 2011. 118

[58] Chengkun Xu, Jiamin Wu, Umang V. Desai, and Di Gao. High-efficiency solid-state dye-sensitized solar cells based on TiO2-Coated ZnO nanowire arrays. *Nano Letters*, 12(5):2420–2424, 2012. 119

[59] K. Wang, J. J. Chen, Z. M. Zeng, J. Tarr, W. L. Zhou, Y. Zhang, Y. F. Yan, C. S. Jiang, J. Pern, and A. Mascarenhas. Synthesis and photovoltaic effect of vertically aligned ZnO/ZnS core/shell nanowire arrays. *Applied Physics Letters*, 96(12):123105, 2010. 119

[60] NOV Plank, HJ Snaith, C. Ducati, JS Bendall, L. Schmidt-Mende, and ME Welland. A simple low temperature synthesis route for ZnO–mgo core–shell nanowires. *Nanotechnology*, 19(46):465603, 2008. 119

[61] Xue-Lian Yu, Jun-Guo Song, Ying-Song Fu, Yang Xie, Xin Song, Jing Sun, and Xi-Wen Du. ZnS/ZnO heteronanostructure as photoanode to enhance the conversion efficiency of dye-sensitized solar cells. *The Journal of Physical Chemistry C*, 114(5):2380–2384, 2010. 119

[62] J. Qiu, X. Li, F. Zhuge, X. Gan, X. Gao, W. He, S.J. Park, H.K. Kim, and Y.H. Hwang. Solution-derived 40 um vertically aligned ZnO nanowire arrays as photoelectrodes in dye-sensitized solar cells. *Nanotechnology*, 21(19):195602, 2010. 121

[63] Pablo Docampo, Aruna Ivaturi, Robert Gunning, Varun Sivaram, and Henry Snaith. The influence of 1D meso- and crystal structures on charge transport and recombination in solid-state dye-sensitized solar cells. *Journal of Materials Chemistry*, 1, 2013. 124

[64] Lori E. Greene, Matt Law, Benjamin D. Yuhas, and Peidong Yang. ZnO/TiO2 core/shell nanorod/P3HT solar cells. *The Journal of Physical Chemistry C*, 111(50):18451–18456, 2007. 123

Chapter 6

Incorporation of Mesoporous Single Crystals of TiO_2 into SDSCs and Investigation of Electronic Properties

6.1 Introduction

6.1.1 Motivation

In the preceding Chapter, we explored one-dimensional nanostructures comprised of alternative metal oxides with higher intrinsic mobilities as replacements for nanocrystalline TiO_2 (nc-TiO_2). While the bulk mobilities of those materials, like SnO_2 and ZnO, may indeed be much greater than that of bulk TiO_2, we discovered that replacement of the TiO_2 photoanode did not result in easy performance gains. We stressed at the end of the last Chapter that an exhaustive reëngineering and optimization process could harness the charge transport capabilities of these materials.

In this Chapter, we follow a different approach. Because the DSSC has had a twenty year development history based on the TiO_2 photoanode, including complementary components (dyes, hole transporters, surface treatments, additives,

etc.) optimized for that particular material, we partially subscribe to the view that "If it ain't broke, don't fix it." Yet as described earlier, there are fundamental limitations to the current architecture, the most notable being the thickness restriction which limits absorption.

Arguably, the higher bulk mobilities of the alternate materials used in the preceding Chapter are largely irrelevant; the time constant of note is that of trapping processes. Therefore, a different line of thought urges us to keep TiO_2 as the photanode material, so as to preserve the rich set of device optimizations designed around it, but to restructure it to enhance charge transport. In this Chapter, we introduce a new TiO_2 mesostructure—the mesoporous single crystal—and explore its effects on device performance and charge transport.

The purpose of sintering together nanocrystals of TiO_2 is to achieve a high surface area to allow for a high density of adsorbed dye and therefore a high light extinction coefficient. The drawback of using nc-TiO_2, as expressed earlier, is that charge transport is transformed from simple diffusion to trap-mediated transport. The trap sites, as earlier discussed, arise from interparticle grain boundaries, the absence of long range crystal structure, and intrinsic defects of the particles themselves.

The nanowires explored last Chapter occupy an opposing site from nc-TiO_2 on the spectrum between high surface area and bulk transport properties—they exhibit fast transport but significantly lower surface area and hence lower device current. The TiO_2 mesoporous single crystal rejects the entire premise of such a trade-off. By synthesizing a large single crystal with the high surface area of sintered nanoparticle, we can combine the conventional advantages of nc-TiO_2 with some of the transport enhancements achieved in the last Chapter.

6.1.2 Synthesis and Material Characterization

The growth of the TiO_2 mesoporous single crystal (MSC) follows a seeded templating mechanism more fully described by Crossland et al. [1] The method builds upon previous research demonstrating the hydrothermal synthesis of micron-sized TiO_2 single crystals using a TiF_4 precursor.[2] We apply a similar synthesis approach within a sacrificial silica template, which when etched leaves a single

crystal structure that is the inverse of the high surface area template.[3; 4; 5]

Such templating methods will not normally work with this hydrothermal growth mechanism because nucleation will largely take place in the bulk, rather than in the template. However, by pre-seeding the template with TiO_2 nanoparticles, the barrier to nucleation at low temperatures is no longer insurmountable, and the crystals grow almost uniformly within the template.

The result of the synthesis is a solution of template in which TiO_2 single crystals have grown. The composite Figure 6.1 illustrates this process and offers evidence that indeed single crystals of TiO_2 emerge from the process. The schematic demonstrates the shape of the template and the growth of TiO_2 crystals both within the template and on the edges. Indeed, in rare cases of the latter, we observe such a "half-templated" MSC which has grown out of the edge of the template; the facetting is strong evidence of the single crystallinity of the product. Not shown are Laue and X-Ray diffraction patterns which confirm the single crystallinity of the MSCs.

6.2 MSC based SDSC Device Optimization[1]

6.2.1 Optimization of Deposition Method

As described in the preceding Chapter during the discussion of SnO_2/P3HT devices, uniformity of the hole transporter capping layer is essential to prevent device shorting and a unipolar electron leakage current. An obvious challenge when working with micron-sized MSCs is deposition of a smooth film, or at least accomplishing a conformal coating with the hole transporter. We first attempt to fulfill the former goal, dealing with the latter in the subsequent section.

Following the synthesis, the MSCs are etched in NaOH and cleaned in water and ethanol. Upon disposal of most of the supernatant ethanol, we added variable amounts of ethanol, terpineol, and cellulose to examine the effect on doctor-bladed film quality. The results are displayed in Figure 6.2, in which the optimal ratio

[1]The research presented here regarding device optimization arose from a collaboration with Nakita Noel and Edward Crossland. E.C. and V.S. synthesized MSCs of varying material parameters and N.N. and V.S. fabricated devices and performed transient and SEM characterization.

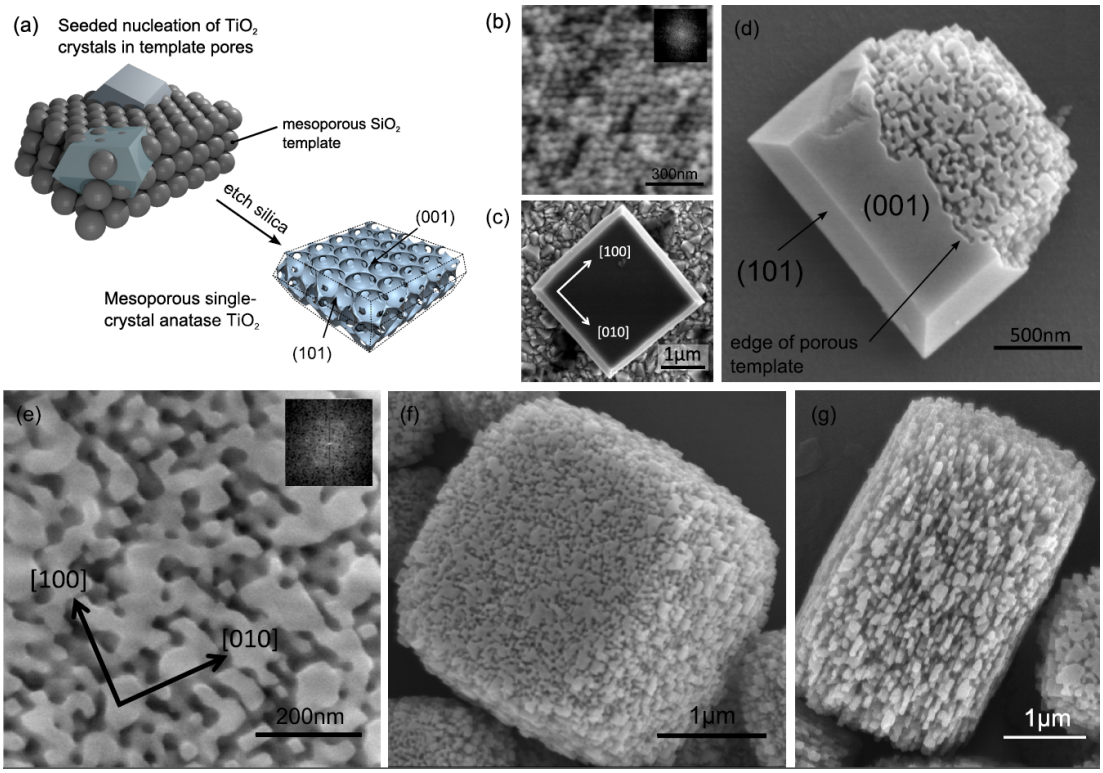

Figure 6.1: Synthesis of mesoporous TiO_2 single crystals. (a) Schematic nucleation and growth of TiO_2 anatase single-crystals within a mesoporous template. (b) Pristine silica template made up of quasi close-packed silica beads (FFT inset 49 ± 3 nm 6-fold symmetry). (c) Non-porous truncated bipyramidal TiO_2 crystal homogeneously nucleated at 210 °C in 20 mM TiF_4. (d) Templated mesoporous variant of (c) (after template removal) nucleated at or near the template surface such that a non-porous volume coexists with a mesoporous region within a single faceted microcrystal. (e) Replication of the mesoscale pore structure within the templated region (FFT inset 47 ± 3 nm 6-fold symmetry) with crystal lattice vectors implied from the particle symmetry overlaid (reaction conditions 170 °C, 40 mM TiF_4). (f,g) Fully mesoporous TiO_2 crystals grown by seeded nucleation in the bulk of the silica template. Reprinted with permission from [1].

of MSC:ethanol (w/w) is 1:10.

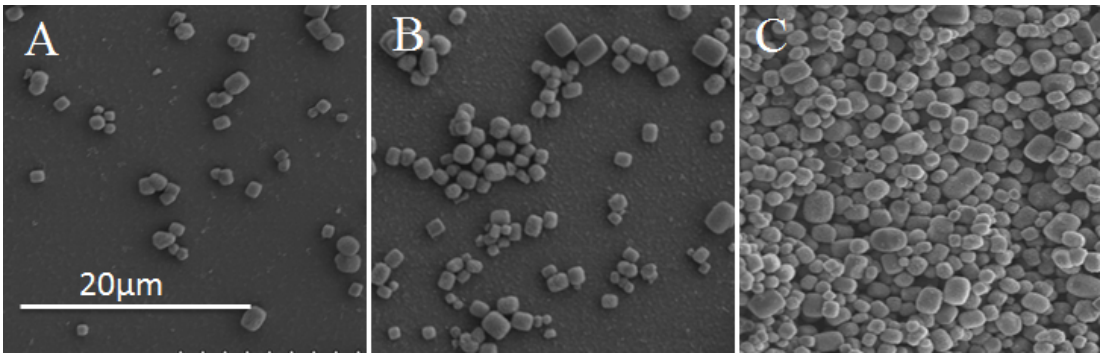

Figure 6.2: SEM images of MSC films deposited using doctor blading of solutions with MSC fractions in Ethanol (w/w) of (a) 0.1%, (b) 1%, (c) 10%.

As the MSC concentration in ethanol increases, we see a corresponding increase in the number density of MSCs deposited per unit area. The objective is to attain a film uniformly coated by at least a monolayer of MSCs. At what we have determined is the optimal concentration, the films are certainly not smooth. However, they are on average two monolayers of MSCs thick, corresponding to film thicknesses of 1-2 μm. The existing literature holds that this roughness is far too severe for a functioning SDSC.[6] However, in the next section we explore routes to achieving a uniform capping layer of the hole transporting material.

6.2.2 Deposition of a Conformal, Infiltrated Hole Transporter Layer [1]

Given the high film roughness of the doctor-bladed MSC films, short circuits appear likely from the non-uniform MSCs to the silver counterelectrode. Indeed, the competing demands of low hole transporter viscosity to effectively infiltrate pores and high viscosity to achieve a conformal capping layer appear to doom the enterprise. This is reminiscent of the dilemma faced with the SnO_2/P3HT cells. The solution then was to implement a double coating strategy, but that approach is infeasible in this case because the chlorobenzene solvent dissolves the Spiro too

[1] In Figures 6.4 and 6.5, N.N. fabricated devices and V.S. characterized them on the solar simulator, SEM, and transients rig.

quickly for a second deposition to avoid wiping out the first.

Therefore, we simply varied the Spiro-OMeTAD concentration in chlorobenzene (by weight) in the spin-coating solution and investigated the effect on capping layer uniformity. The cross-sectional and tilted surface images are displayed in Figure 6.3.

As the Spiro concentration in chlorobenzene in the spin-coating solution increases, so too does the uniformity of the coating of the MSCs. At 10% Spiro concentration, the majority of the MSCs is exposed at the top to potential contact with the counterelectrode without any Spiro capping layer intervening. The tilted view gives a good assessment of the surface roughness, and we can discern the porosity of the crystals from above, indicating that the MSCs have indeed not been infiltrated or covered by the Spiro near the top.

At 13% Spiro concentration, we clearly observe more effective coating of the MSCs with the Spiro hole transporter. However, both from cross-sectional and tilted views, the porosity of the MSCs is evident near the top, signifying device shorting pathways. Nevertheless, there is clearly a trend toward conformal coating of the MSCs, clearly visible in cross-section from the layer of Spiro that covers the compact layer in the absence of an MSC and rises to cover an adjacent MSC.

Finally, at 15% Spiro concentration, the MSCs are indeed covered quite effectively. We choose to include this particular image in cross-section to demonstrate that occassionally, particularly large crystals will be found which even this high concentration Spiro spin-coating solution will not cover. Thus, as evident in Figure 6.3(c), there is generally a uniform, conformal coating of Spiro except over the large crystals, where a clear shorting path exists.

We proceeded to incorporate these photoanodes, sensitized with dye prior to Spiro infiltration, into SDSCs to measure the effects of Spiro concentration on device performance. The results are summarized in Figure 6.4.

The effect of increasing the Spiro concentration and hence the uniformity of the capping layer is clearly positive for all of the device performance metrics. The short circuit current sees a sustained rise from 10 to 13 to 15%, indicative of the elimination of leakage paths. The open circuit voltage improves as the Spiro concentration is increased from 10% to 13% and stabilizes thereafter, indicating that recombination in the cell decreased in the first interval, likely because of

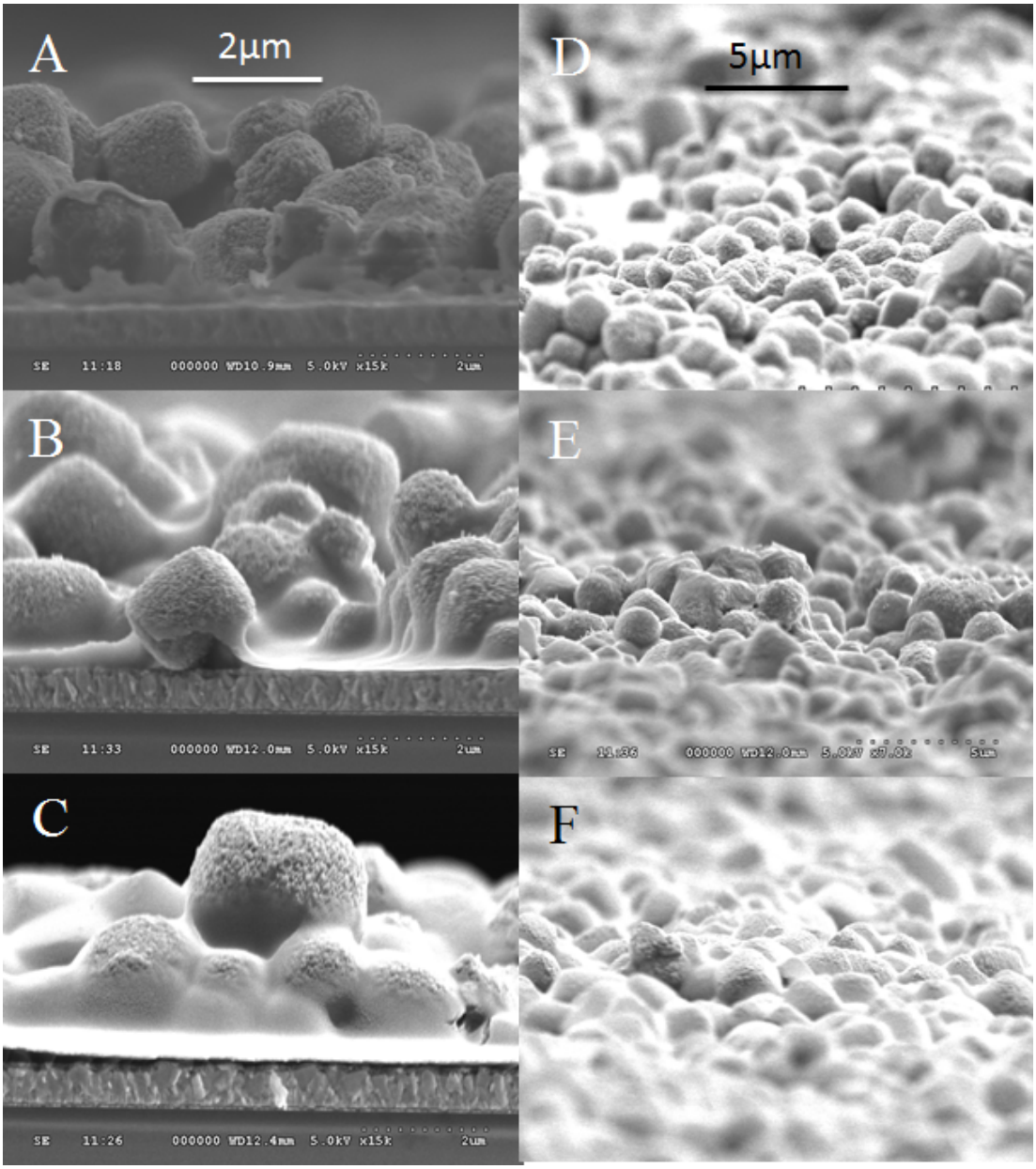

Figure 6.3: SEM cross-sectional images of MSC doctor bladed films infiltrated with Spiro cast from a solution in chlorobenzene at (a) 10%, (b) 13%, and (c) 15% by weight; SEM tilted surface top view of MSCs infiltrated with Spiro, the concentration of which in chlorobenze is (d) 10%, (e) 13%, and (f) 15% by weight.

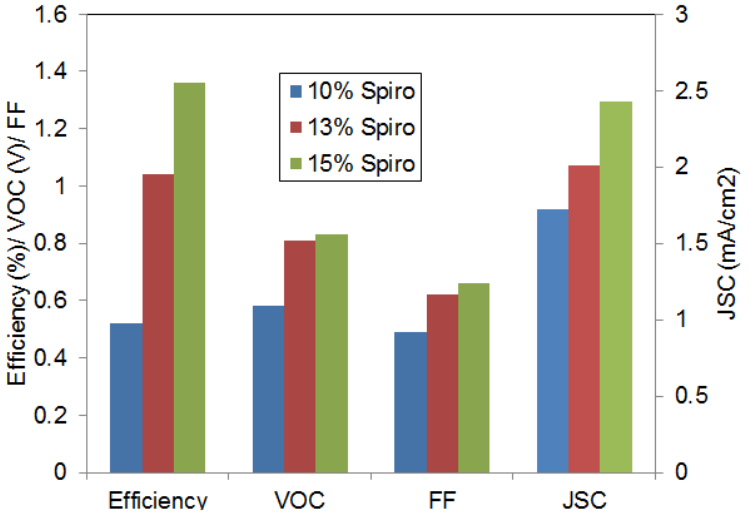

Figure 6.4: Device Performance Characteristics (efficiency, short circuit current, open circuit voltage, and fill factor) for devices fabricated with Spiro concentrations in chlorobenzene in the spin-coating solution of 10%, 13%, and 15%. The short-circuit current is plotted on the right axis, while the other three metrics are plotted on the left axis. Each data point corresponds to the average of four cells, and this convention will be followed in subsequent figures.

insufficient pore filling at the lowest Spiro concentration. Finally, the fill factor increases with increasing Spiro concentration for the simple reason that the shunt resistance is increasing with an increasingly uniform capping layer.[7]

The devices actually perform surprisingly well considering the variation in film thickness from point to point. In this section, the optimization of hole transporter capping layer uniformity has improved device efficiency past 1%, and we present further optimizations below.

6.2.3 Addition of a Titanium Isopropoxide "Glue" Layer

While the purpose of the TiO_2 Mesoporous Single Crystal was to create long range crystal order on the micron scale, electronic transport in our doctor-bladed layers must still traverse at least one inter-MSC connection given the two-monolayer thickness of the photoanode. To facilitate this, we spin-coated a solution of titanium isopropoxide in the same manner in which we deposited a TiO_2 compact

layer. An SEM of the resulting structure and device performance characteristics are found in 6.5.

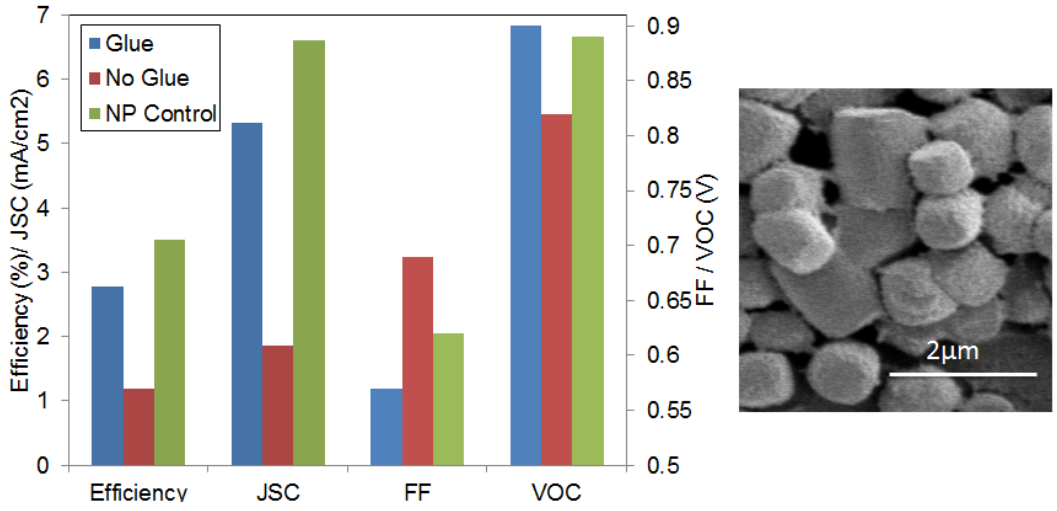

Figure 6.5: (a) Device Performance Characteristics (efficiency, short circuit current, open circuit voltage, and fill factor) for MSC based devices fabricated with and without a "glue" layer formed by spin coating titanium isopropoxide over the MSC film. Metrics for control devices, comprised of conventional TiO_2 nanoparticle (NP) photoanodes are also plotted. The efficiency and short circuit current are plotted on the left axis, while the fill factor and open circuit voltage are plotted on the right axis. (b) SEM image of MSC film after deposition of a "glue" layer.

We can see that the new layer drastically improves the performance of SDSCs based on MSCs. The gain is almost entirely due to an improvement in short circuit current, suggesting that in fact much more charge is now being collected at the electrode after successfully traversing inter-MSC connections facilitated by the "glue." We have chosen this name because of the spiderweb like appearance of the isopropoxide layer, which, from the SEM image, appears to add connections to otherwise separated MSCs. In the performance characteristics, we also choose to include a control device, fabricated using conventional nanocrystalline TiO_2, to demonstrate that the MSC cells are now approaching the performance attributes of conventionally fabricated cells.

6.2.4 Compositional Blends of MSCs with nc-TiO_2

As evidenced in Figure 6.5, the current of MSC based devices lags that of conventional devices. The possible reasons are manyfold, including possible blocked porosity in the interior of the MSCs or poor surface functionalization leading to low dye uptake. Therefore, we endeavored to fabricate a mixed system of MSCs and nanoparticles to "fill in the gaps" or otherwise deposit a smoother film, and contribute to higher dye uptake. To do so, we mixed MSC and nc-TiO_2 pastes in variable ratios to test the effect of the compositional blend on device performance.

Figure 6.6 demonstrates this effect. The SEM images clearly illustrate the smoothening of the film as an increase in the fraction of nc-TiO_2 fills in the gaps between the MSCs, electronically links them together, and smooths the film. The device current clearly increases with increased nanoparticle concentration, but the open circuit voltage decreases; the current trend overwhelms the voltage trend and the efficiency is highest when the device is largely comprised of nanoparticles, as we may have guessed from the results of the previous section.

This concludes the device optimization section of this Chapter. The goal was really to demonstrate that MSCs can be used as viable photoanodes, either in conjunction with nc-TiO_2 or alone. However, different strategies need to be employed to, for example, ensure electronic contact between MSCs using a "glue" layer. Upon reaching this level of device performance, where MSC devices have efficiencies comparable to conventionally processed SDSCs, we can proceed to study the interesting transport properties of MSCs, especially upon thermal treatment.

6.3 Investigating the Source of Doping in Annealed TiO_2 Mesoporous Single Crystals for Use in SDSCs

6.3.1 Background

Since the invention of the DSSC, a strong dependence between cell performance and the anneal temperature of TiO_2 nanoparticles has been observed, and the list

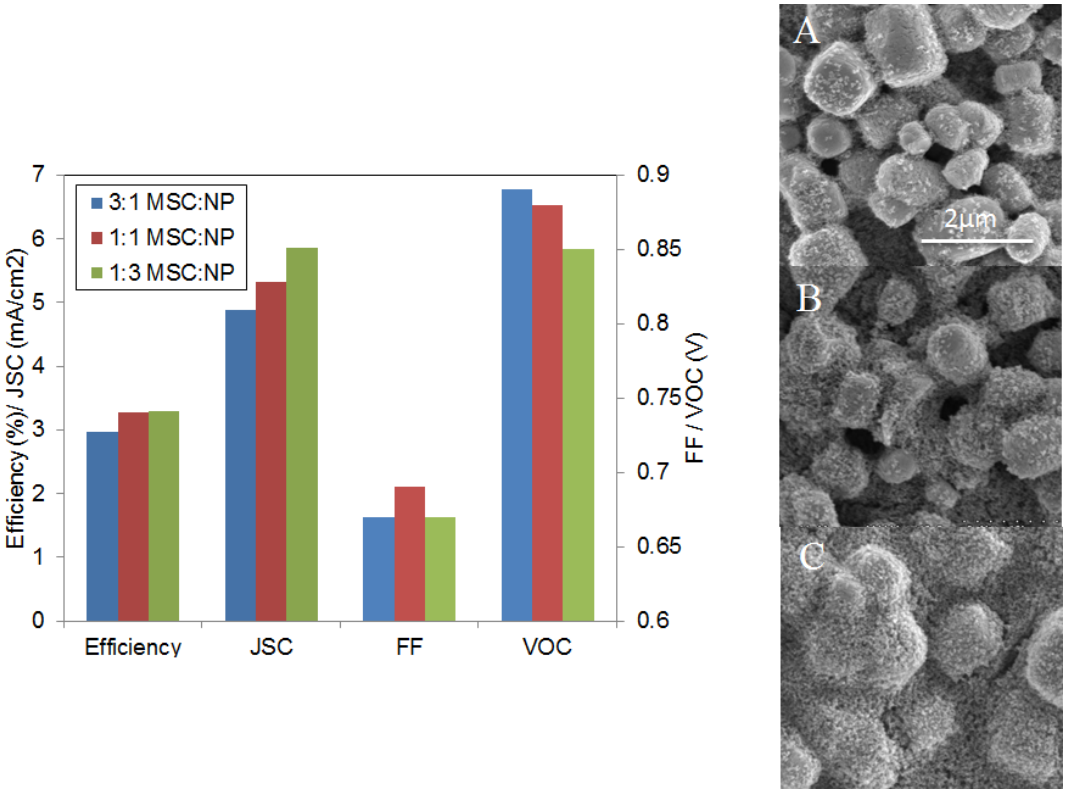

Figure 6.6: SEM images of photoanodes comprised of MSCs and TiO_2 nanoparticles (NP) in the following ratios: (a) 3:1 MSC:NP, (b) 1:1 MSC:NP, (c) 1:3 MSC:NP; (d) Device Performance Characteristics (efficiency, short circuit current, open circuit voltage, and fill factor) for devices incorporating various fractions of MSCs and NPs. The efficiency and short circuit current are plotted on the left axis, while the fill factor and open circuit voltage are plotted on the right axis.

of proposed explanations continues to grow. Indeed, while the inaugural paper asserts that "electronic contact between the particles was produced by brief sintering at 450°C,"[8] subsequent researchers have added increased crystallinity,[9] altered electronic states,[10] water deadsorption,[11] and surface modification,[12] among others, to the catalogue of effects of thermal treatment.

The covariance of these effects makes them difficult to disentangle, but each is important to understand independently to elucidate the processes of charge transport. The quest to improve electronic transport in DSSCs has spawned several approaches and novel nanostructures, generally with the aim of improving the

charge collection efficiency. In the preceding chapter, we pursued one-dimensional structures with higher mobilities (ZnO and SnO_2) to direct charges to collection quickly, before recombination.[13; 14; 15] Others aim to increase the electron lifetime, e.g., via insulating shells around the mesoporous TiO_2[16] or through better pore filling in solid state devices.[17] Finally, a large body of theoretical work investigates the implications of multiple trapping transport in the electronically defective TiO_2.[18; 19] These efforts reflect the field's recognition of the diffusion constant, electron lifetime, and trap state density as important levers to improve charge transport, while no consensus has emerged on the relative merits of each approach with respect to cell performance. Annealing appears to impact all three metrics, and it is therefore crucial to clarify the mechanisms by which it affects the DSSC.

One infrequently studied consequence of annealing of DSSCs with likely impacts on charge transport is the creation of oxygen vacancy defects and the resultant increase in background charge density. As the annealing temperature rises, previous reports assert that oxygen diffuses away from lattice sites, reducing TiO_2 at the vacancy sites.[20] These vacancies can subsequently cause n-type behavior of TiO_2 according to DFT calculations which characterize them as "shallow donors."[21] This doping behavior of such oxygen vacancy defects is enhanced at low oxygen partial pressures, rationalized by oxidation of surface vacancies by atmospheric oxygen.[22] The doping from oxygen vacancy defects is a fourth lever for controlling charge transport because charge density, as we have seen before in Chapter 3, impacts the effective diffusion constant in DSSCs. Others have reported doping TiO_2, e.g., through addition of Nb5+ ions,[23] but unintentional doping as a result of temperature treatment has not been studied.

We will employ the MSC to control many free variables in nanoparticles and isolate a previously unreported effect of annealing temperature on DSSCs: increased doping density from oxygen vacancy creation. As earlier explained, MSCs are a promising material to replace the conventional TiO_2 nanoparticles because they combine the advantages of single crystallinity with high surface area, offering fast electron transport and strong light absorption.

Whereas other studies have found that annealing changes both geometric and electronic properties of TiO_2 nanoparticles, for example neck growth in interpar-

ticle connections and trap state density,[24] using MSCs allows the assumption that the geometry remains constant. Due to the large domain size of an MSC, electrons need only navigate a few MSCs at most in their transit from dye to electrode, so interparticle connections cease to be very important (especially after application of a "glue" layer as described previously). Moreover, the TiO_2 domain size, volume and exposed surface area remain constant with increasing temperature treatment, in contrast to other promising tunable TiO_2 mesoporous systems, like those synthesized from diblock copolymers in which temperature affects domain size.[25]

Additionally, MSCs can undergo thermal treatment prior to deposition onto the substrate, which sets them apart from conventional nanoparticles in terms of processing. Heating MSCs while they are still in the silica template offers the advantage of structural confinement, as the silica acts as a scaffolding to prevent phase changes in the MSC. Previous reports of structurally confined TiO_2 confirm that the phase transition temperature rises above 850°C,[26] allowing us to heat MSCs considerably above the normal 500°C sintering temperature without incurring processability penalties or a phase transition from anatase to rutile.[27] Corollary to this are the tremendous processability advantages of processing an all-low-temperature cell, made possible by the obviation of sintering the photoanode *after* film deposition and instead sintering in-template.

To verify that indeed there is no phase change upon high temperature annealing, we extracted the XRD spectra for MSCs still in template annealed at temperatures up to 850°C. Figure 6.7 plots those spectra and demonstrates clearly that there is no significant phase change from anatase to rutile even at high temperatures due to the structurally confining silica template.

This thesis will study MSCs thermally treated from 500°C to 850°C. We study an in-template sintering temperature range above 500°C in order to control for other effects that have been demonstrated at lower temperatures, such as water de-adsorption, and to integrate MSC films into the normal DSSC process flow which includes steps at 500°C. Thus, thermally treating MSCs in the range of 500°C to 850°C allows us to investigate the changes in electronic structure while holding fixed particle geometry and phase and also leveraging a finely tuned DSSC process flow.

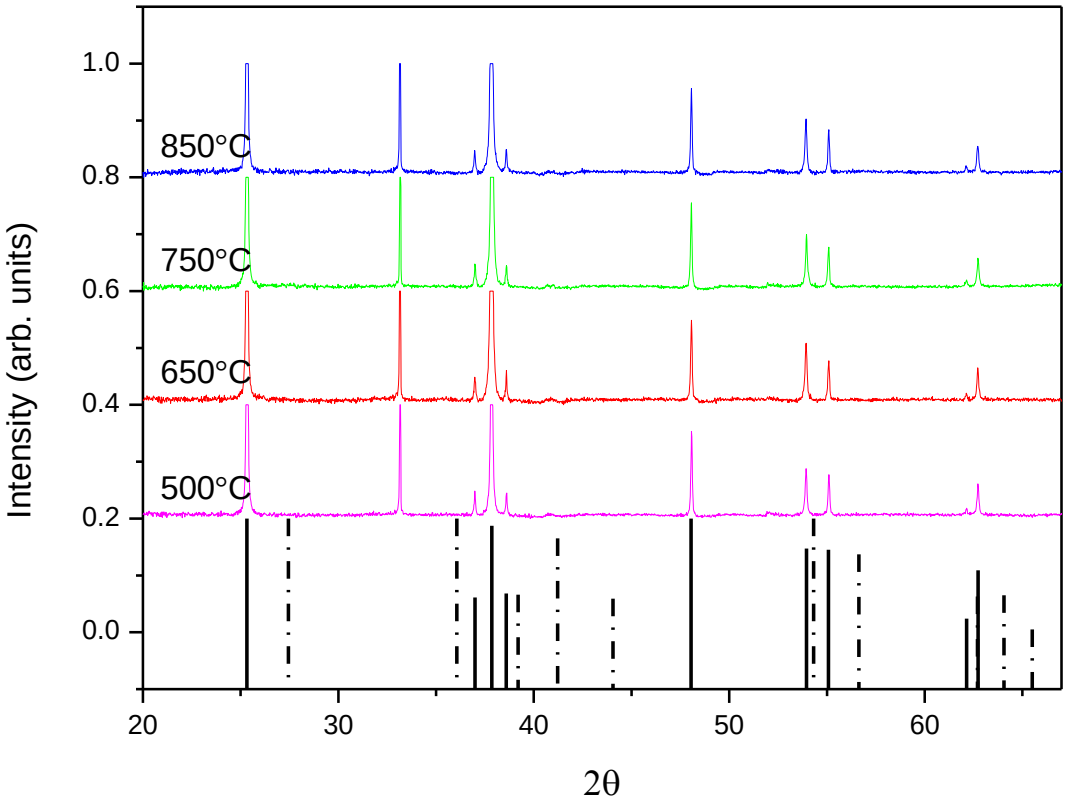

Figure 6.7: XRD Absorption Spectra of MSCs annealed at different temperatures. Solid lines at bottom of graph denote TiO_2 anatase reference spectrum, and dotted lines denote rutile reference. Some peaks have been truncated for visual clarity.

We will proceed by first examining the effect of anneal temperature on the performance of SDSCs with MSCs comprising the photoanode. Subsequently, we probe electronic transport using transient photocurrent and photovoltage decay as well as transient mobility spectroscopy. Finally we appeal to steady state conductivities in vacuum and air to isolate the oxygen vacancy doping mechanism.

6.3.2 Results and Discussion

6.3.2.1 Solar Cell Performance and Characterization

SDSCs were fabricated with photoanodes comprised of TiO_2 MSCs, which had been pre-annealed (prior to etching of the template and subsequent film deposi-

tion). The performance characteristics under full sun illumination are summarized in Figure 6.8 below.

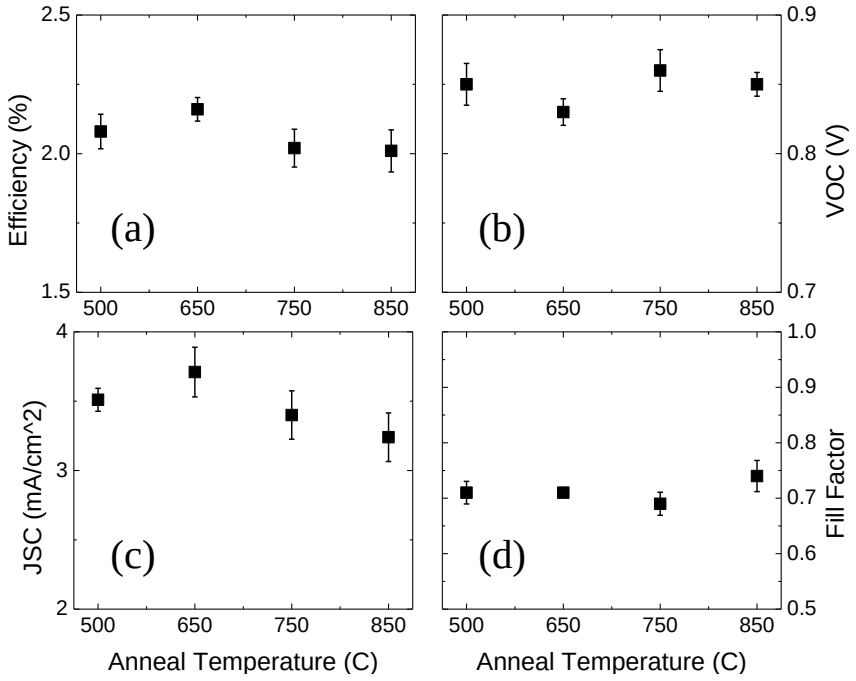

Figure 6.8: Efficiency (a), Open Circuit Voltage (b), Short Circuit Current (c), and Fill Factor (d) for solid state dye sensitized solar cells fabricated with MSCs annealed at different temperatures.

No difference between the devices is obviously discernible from the basic performance metrics after accounting for experimental variation. Routes for improving solar cells based on MSCs will be presented in a future work and include promising prospects for increased dye adsorption through smaller MSC pore size, improved surface functionality, and smoother and more uniform film deposition. Future efficiency enhancements notwithstanding, the current, functional cells serve as important instructional devices for understanding the effect of annealing on TiO_2.

To probe electronic transport beyond solar cell summary metrics, we employed transient photocurrent and photovoltage decay techniques (described in the experimental section), and the results are summarized in Figure 6.9(a).

Unlike the summary cell performance metrics, the transport rate dependence

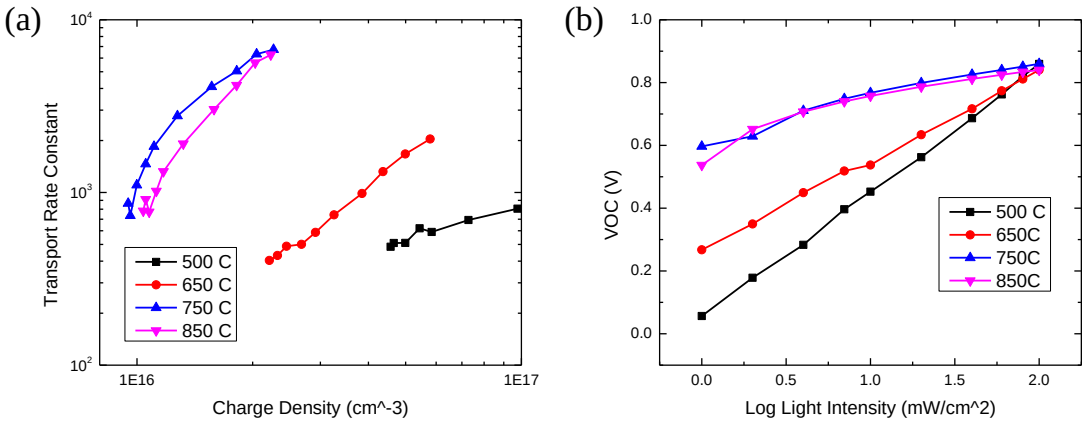

Figure 6.9: (a) Transport Rate Constant dependence on charge density and (b) Open Circuit Voltage dependence on Light Intensity for solar cells fabricated with MSCs annealed at different temperatures.

on anneal temperature exhibits a clear trend. As MSCs are annealed at higher temperatures, the transport rate increases while the injected charge density measured decreases; this trend saturates after an annealing temperature of 750°C. At full sun intensity, the product of charge density and transport rate constant is approximately equal for all four anneal temperatures. Therefore, the present result is intuitively compatible with the similar short circuit current densities measured for these solar cells, since current can be decomposed into transport, or extraction, rate and charge density. By separately measuring these parameters via transient decay methods, we succeed in differentiating devices that perform similarly under solar cell operating conditions.

Figure 6.9(b) plots the dependence of open circuit voltage on light intensity. Again, we can differentiate devices with similar open circuit voltages at full sun by observing the variable loss in voltage with decreasing light intensity. While all devices exhibit the same voltage under full sun intensity, devices with MSCs annealed at higher temperatures lose less voltage under low illumination. The open circuit voltage is a direct indicator of the offset between the quasi-Fermi level of the TiO_2 and the HOMO of the hole conductor. This suggests that the dark electron density is higher in devices annealed at high temperatures, since electron density is exponentially related to the TiO_2 Fermi level.

This apparent background charge or doping density is theoretically consistent with the faster transport rates for devices annealed at higher temperatures shown in Figure 6.9(a).[28] Improvement in the effective electron diffusion coefficient with increasing charge density is a well-studied phenomenon in DSSCs which we have introduced before in Chapter 3. While the increased charge density does not affect the free electron diffusion coefficient, the multiple trapping diffusion rate is limited by trapping/detrapping processes; under this paradigm, a higher charge density increases occupancy of the exponential tail of sub-bandgap trap states, reducing the depth and number of available trap sites and hence the average waiting time for detrapping to the conduction band.[29] Thus, the result is a higher effective diffusion constant, a composite measure reflecting free electron diffusion and trap-related rate constants. Since the charge extraction technique only measures photoinjected charge, Figure 6.9(a) does not reflect the background charge contribution to total charge density; indeed, the higher effective diffusion constant caused by background doping density reduces the photoinjected charge density in the film necessary to achieve the same short-circuit current.

6.3.2.2 Conductivity and Transient Photoinduced Absorption Spectroscopy Results

The preceding discussion presented evidence that higher anneal temperatures increase the effective electron diffusion constant for MSCs and that this is caused by anneal-induced doping. We now rigorously test the former part of the hypothesis by more directly measuring the electronic properties of the MSCs, first in isolation and then assembled into a film. Because the MSCs are not incorporated into the DSSC architecture with its attendant complexities, we can probe electronic properties with greater confidence.

First, we measured the two-probe conductivity of isolated MSCs without dye and in the dark, comparing the values from MSCs annealed at 850°C to those annealed at 500°C. We summarize the method and resulting conductivity values in Figure 6.10. Utilizing electron beam lithography to fabricate gold electrodes spaced 500nm apart, we positioned a single crystal to bridge the gap and measured the current-voltage characteristic, displayed in Figure 6.10(a). The curves

displayed are representative of several repetitions of the experiment and yield reproducible estimates of the conductivity after taking into account geometric factors. We observe that the conductivity recorded for an MSC annealed at 850°C was over twice that of an MSC annealed at 500°C. Since this is a dark measurement, it is again consistent with a higher background charge density in the sample annealed at higher temperature. This measurement also controls for the effects of interparticle connections and allows us to directly probe the internal conductivity of an MSC.

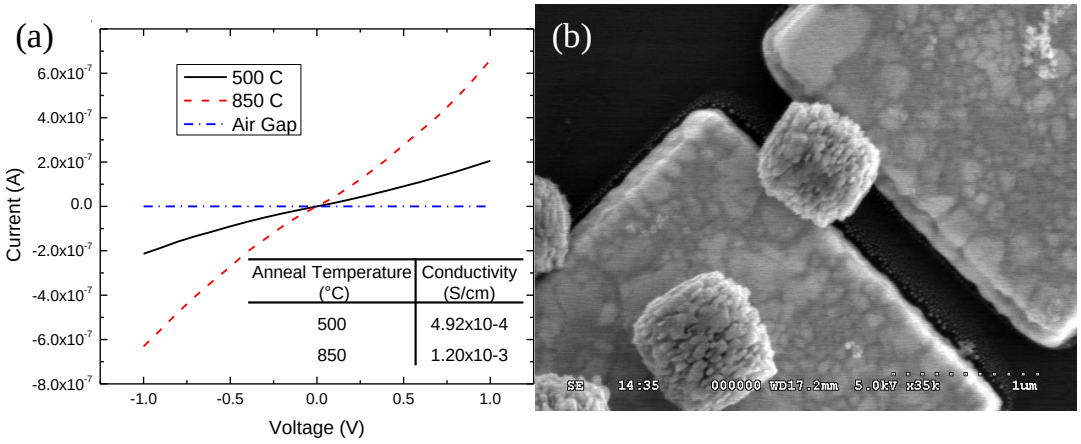

Figure 6.10: (a) Current vs Voltage plot of single MSCs annealed at different temperatures with conductivity values displayed alongside and (b) Scanning Electron Micrograph of the experimental setup, whereby a single MSC was positioned to connect two gold electrodes.

To disaggregate the two factors that comprise conductivity, electronic mobility and charge density, we employed Transient Mobility Spectroscopy (TMS) to probe films of dye-laden MSCs.[30] This technique simultaneously monitors charge density, via transient absorption spectroscopy of the excited dye cation, and lateral conductivity of the MSC film. The resulting mobility values are plotted in Figure 6.11 for a range of charge densities.[1] The bottom axis refers to the effective charge density, computed by simply dividing the number of charges by the device volume; this measure is compatible with the mobility calculation,

[1]TMS measurements, like that in Figure 6.11, were carried out by Tomas Leijtens, Oxford University, on devices prepared by V.S.

which also relies on the entire device volume. To incorporate the geometry of the MSC film, we report a corrected charge density in the top axis which employs the actual TiO_2 volume by multiplying the total device volume by a composite MSC packing/porosity factor. The values of charge density reported on the top axis can now be compared to those reported in Figure 6.9(a); the higher values of corrected charge density in Figure 6.11 reflect the open circuit condition of the transient absorption measurement, whereas a device undergoing transient decay at short-circuit loses charges to collection.

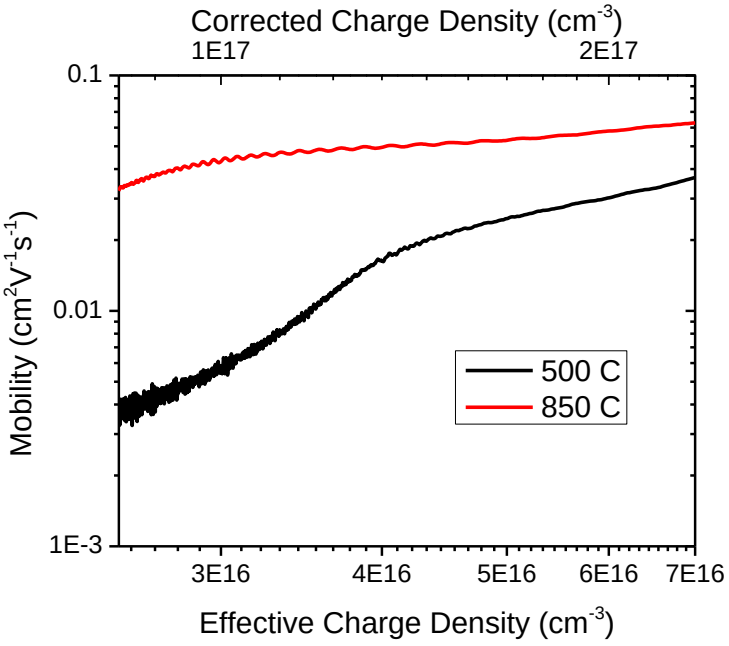

Figure 6.11: Mobility and Diffusion Coefficient (calculated from Einstein Relation) as a function of photoinduced charge density for MSC films annealed at different temperatures. The bottom axis treats the film volume as the device volume, while the top axis corrects for the MSCporosity and packing factors.

The MSC film annealed at higher temperature exhibits a higher effective mobility than that annealed at the lower temperature by about an order of magnitude at low charge densities. As the charge density increases, this difference narrows. The TMS results offer strong evidence reinforcing the hypothesis that increased background charge density in the MSCs annealed at higher temperature increases the electronic transport rate. A higher effective mobility implies a higher effec-

tive diffusion constant by the Einstein relation—although the multiple trapping framework requires modifying the simple Einstein relation, the new expression retains the proportionality between effective mobility and diffusion coefficient.[31] Thus, transport in the DSSC, widely conjectured to be exclusively diffusive, will indeed occur faster if the effective mobility is higher.[32] The narrowing of the difference in effective mobility with increasing photoinjected charge density is evidence of a fixed background charge density, the significance of which diminishes with increasing light intensity.

Finally, to expose the mechanism behind the electronic doping that previous measurements have supported, we aimed to isolate oxygen as a variable by testing the conductivity of MSC films under full sun intensity in vacuum and in air. Since the solar spectrum includes ultraviolet light with energy higher than the bandgap of TiO_2, we included MSC films with and without adsorbed dye to differentiate between electrons generated in the MSC and those injected from the dye. The conductivities are displayed in Figure 6.12, and the ratios of 850°C : 500°C conductivities are tabulated in the table below.

Both neat and dye-laden MSC films exhibit higher conductivity in vacuum than in air, and the samples annealed at higher temperatures are more conductive than the samples at lower temperature in vacuum and in air. However, the Table in Figure 6.12 quantifies how the conductivity enhancement in vacuum is exaggerated for the higher anneal temperature samples. Taken together, these observations are consistent with the theory that higher annealing temperatures create more oxygen vacancies which, in the absence of atmospheric oxygen to passivate those defects at the surface, enable a long-lived conduction band electron population under UV radiation.

Leijtens et al describe this mechanism in detail elsewhere,[33] but the schematic in Figure 6.13 (adapted with permission) outlines it.

Thus atmospheric oxygen suppresses the creation of conduction band electrons by passivating surface oxygen vacancies. In vacuum, the charge density for MSC films annealed at higher temperature is enhanced more than for lower temperature counterparts because of the larger number of vacancies in the former; this is evident from the tripling of the ratio of conductivities of neat 850°C : 500°C MSCs in vacuum compared to air. Dye-laden films display this effect to a lesser

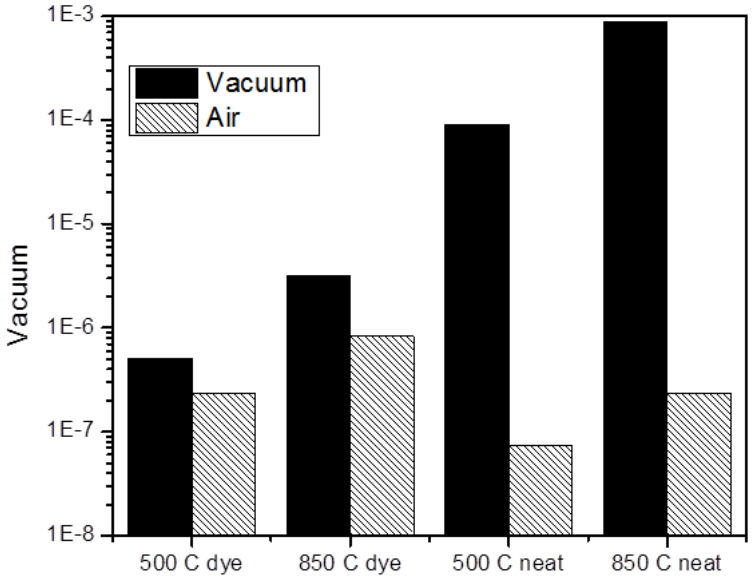

	Dye-laden	Neat
Air	3.57	3.15
Vacuum	6.21	9.64

Figure 6.12: Conductivities (S/cm) in light and vacuum for MSC films with and without dye and annealed at different temperatures. Table below graph lists ratio of conductivities between samples annealed at 850C and at 500C.

extent because both dye and TiO_2 compete for UV absorption.

The results from comparing conductivities in vacuum and air offer a plausible explanation for the preceding results, which together suggest that higher anneal temperature leads to higher background charge density. By monitoring the enhanced response to UV radiation of higher anneal temperature MSCs in vacuum, we can postulate that more surface oxygen vacancies are created at higher anneal temperatures. We then appeal to literature cited earlier which links such defects to n-doping to conclude that oxygen vacancy defects account for the enhanced transport rates and conductivity observed in annealed MSC films and devices.

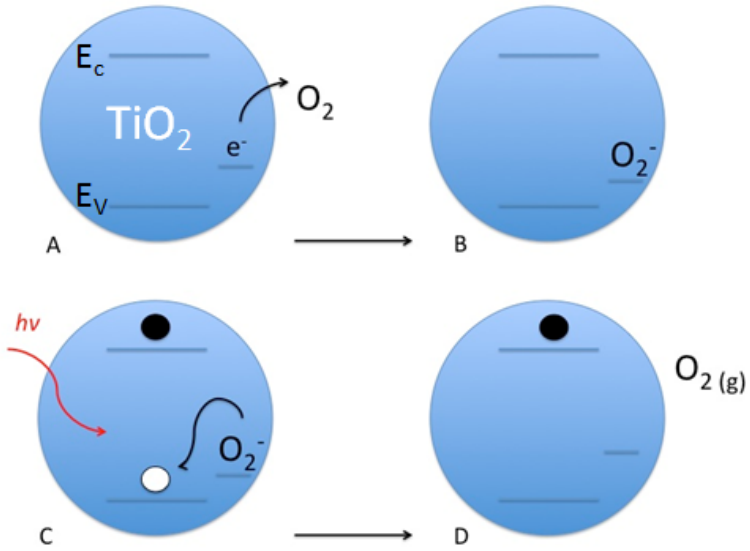

Figure 6.13: Schematic of oxygen vacancy creation via annealing and subsequent effect of UV radiation: (a) TiO_2 annealing causes oxygen vacancy defects, leaving an electron behind; (b) in the presence of molecular oxygen, the electrons at surface vacancies are scavenged by adsorbing O_2, preventing them from contributing to conduction; (c) UV radiation creates electron-hole pairs in TiO_2, and the holes can migrate to combine with O_2-, causing desorption of O_2; (d) in the absence of atmospheric O_2, the conduction band electron is long-lived.

6.3.3 Summary

We have employed a novel mesostructure of TiO_2, the mesoporous single crystal (MSC), to probe the effect of annealing between temperatures of 500°C and 850°C. We deduce that the primary effect is an n-doping of the TiO_2, and we attribute the doping to increased creation of oxygen vacancy defects which result in increased background charge density.

While MSC films annealed at different temperatures performed similarly in solid-state dye sensitized solar cells, they exhibited strikingly different transport rate constants, measured through transient photocurrent and photovoltage decay. We rationalized this through comparison of the dependence of open circuit voltage on light intensity which suggested that samples annealed at higher temperatures possess higher densities of background charge not injected from the dye. We more directly probed electronic properties by measuring the conductivity of

isolated MSCs and confirming that in the dark, the conductivity was higher for samples annealed at higher temperatures. Subsequent measurements using Transient Mobility Spectroscopy (TMS) revealed a higher effective mobility for samples annealed at higher temperature, confirming the hypothesis that increased background charge density results from higher anneal temperatures and increases the effective electron diffusion constant. Finally, we isolated oxygen vacancies as a likely explanatory variable for the increase in background charge density as the anneal temperature increases by measuring conductivities in vacuum and in air under full sun illumination, including UV radiation. We discovered that all samples exhibited higher conductivity in vacuum, explained by a model where oxygen desorption from surface oxygen vacancies enables UV radiation to create a long-lived mobile electron population. Moreover, this effect was enhanced in samples annealed at higher temperatures, implying that more oxygen vacancy defects are created at higher temperature annealing; the effect of such defects in the bulk is to n-dope TiO_2.

6.4 Concluding Remarks

In this Chapter, we explored the potential for incorporating an exciting new material into the SDSC—the Mesoporous Single Crystal (MSC). The combination of extended crystallinity and high surface area, achieved through hydrothermal growth in a pre-seeded template, will deliver dramatic future improvements in charge transport over the conventional architecture.

We first demonstrated the viability of these materials in SDSCs; given the large crystal size, the material was not easily incorporated into the existing process flow. However, by increasing the thickness of the Spiro capping layer and by adding a "glue" layer to enhance inter-crystal connectivity, we effectively improved cell performance to rival standard devices. Future optimization work will certainly be occupied with making the MSC film as smooth as possible to enable lowering the concentration of the hole transporter in the spin coating solution and thus reducing the thickness of the resistive capping layer.

The last section investigated an effect of temperatures between 500°C and 850°C on TiO_2 MSCs. The advantage of using this particular structure is that we

can effectively control other variables that change in conventional nanoparticle-based films, such as particle geometry and crystal phase. By identifying the existence and source of background doping in TiO_2, we improve the explanatory toolkit for charge transport, emphasizing that doping, or increased background charge density, can explain increased effective mobility and faster transport rates. Furthermore, we shed light on an important process that occurs as a byproduct of thermal annealing of TiO_2, with implications for further research to identify the same effect at lower anneal temperatures. Finally, we demonstrate the ability to process MSC films at higher temperatures than are possible for nanocrystalline counterparts and foreshadow the use of this tunable material to enhance device performance.

6.5 References

[1] Edward JW Crossland, Nakita Noel, Varun Sivaram, Tomas Leijtens, Jack A Alexander-Webber, and Henry J Snaith. Mesoporous TiO2 single crystals delivering enhanced mobility and optoelectronic device performance. *Nature*, 495(7440):215–219, 2013. 138, 140

[2] Hua Gui Yang, Cheng Hua Sun, Shi Zhang Qiao, Jin Zou, Gang Liu, Sean Campbell Smith, Hui Ming Cheng, and Gao Qing Lu. Anatase TiO2 single crystals with a large percentage of reactive facets. *Nature*, 453(7195):638–641, May 2008. 138

[3] Alexander S. Finnemore, Maik R. J. Scherer, Richard Langford, Sumeet Mahajan, Sabine Ludwigs, Fiona C. Meldrum, and Ullrich Steiner. Nanostructured calcite single crystals with gyroid morphologies. *Advanced Materials*, 21(38-39):3928–3932, 2009. 139

[4] A.-H. Lu and F. Schuth. Nanocasting: A versatile strategy for creating nanostructured porous materials. *Adv. Mater.*, 18(14):1793–1805, 2006. 139

[5] Ferdi Schuth. Endo- and exotemplating to create high-surface-area inorganic materials. *Angewandte Chemie International Edition*, 42(31):3604–3622, 2003. 139

[6] I-Kang Ding, Jia Zhu, Wenshan Cai, Soo-Jin Moon, Ning Cai, Peng Wang, Shaik M Zakeeruddin, Michael Gratzel, Mark L. Brongersma, Yi Cui, and Michael D. McGehee. Plasmonic dye-sensitized solar cells. *Advanced Energy Materials*, 1(1):52–57, 2011. 141

[7] Pablo Docampo, Andrew Hey, Stefan Guldin, Robert Gunning, Ullrich Steiner, and Henry J. Snaith. Pore filling of Spiro-OMeTAD in solid-state dye-sensitized solar cells determined via optical reflectometry. *Advanced Functional Materials*, 2012. 144

[8] Brian O'Regan and Michael Gratzel. A low-cost, high-efficiency solar cell based on dye-sensitized colloidal TiO2 films. *Nature*, 353(6346):737–740, October 1991. 147

[9] Shingo Kambe, Shogo Nakade, Yuji Wada, Takayuki Kitamura, and Shozo Yanagida. Effects of crystal structure, size, shape and surface structural differences on photo-induced electron transport in TiO2 mesoporous electrodes. *J. Mater. Chem.*, 12(3):723–728, 2002. 147

[10] Kan Takeshita, Yutaka Sasaki, Masahiro Kobashi, Yuki Tanaka, Shuichi Maeda, Akira Yamakata, Taka-aki Ishibashi, and Hiroshi Onishi. Effect of annealing temperature on back electron transfer and distribution of deep trap sites in dye-sensitized TiO2, studied by time-resolved infrared spectroscopy. *J. Phys. Chem. B*, 108(9):2963–2969, February 2004. 147

[11] N.-G. Park, G. Schlichthrl, J. van de Lagemaat, H. M. Cheong, A. Mascarenhas, and A. J. Frank. Dye-sensitized TiO2 solar cells: Structural and photoelectrochemical characterization of nanocrystalline electrodes formed from the hydrolysis of ticl4. *J. Phys. Chem. B*, 103(17):3308–3314, April 1999. 147

[12] S. Nakade, Y. Saito, W. Kubo, T. Kitamura, Y. Wada, and S. Yanagida. Influence of TiO2 nanoparticle size on electron diffusion and recombination in dye-sensitized TiO2 solar cells. *J. Phys. Chem. B*, 107(33):8607–8611, July 2003. 147

[13] Suresh Gubbala, Vidhya Chakrapani, Vivekanand Kumar, and Mahendra K. Sunkara. Band-edge engineered hybrid structures for dye-sensitized solar cells based on SnO2 nanowires. *Adv. Funct. Mater.*, 18(16):2411–2418, 2008. 148

[14] Matt Law, Lori E. Greene, Justin C. Johnson, Richard Saykally, and Peidong Yang. Nanowire dye-sensitized solar cells. *Nat Mater*, 4(6):455–459, June 2005. 148

[15] Bin Liu and Eray S. Aydil. Growth of oriented single-crystalline rutile TiO2 nanorods on transparent conducting substrates for dye-sensitized solar cells. *J. Am. Chem. Soc.*, 131(11):3985–3990, February 2009. 148

[16] Francisco Fabregat-Santiago, Jorge Garcia-Canadas, Emilio Palomares, John N. Clifford, Saif A. Haque, James R. Durrant, Germa Garcia-Belmonte, and Juan Bisquert. The origin of slow electron recombination processes in dye-sensitized solar cells with alumina barrier coatings. *Journal of Applied Physics*, 96(11):6903–6907, 2004. 148

[17] Henry J Snaith, Robin Humphry-Baker, Peter Chen, Ilkay Cesar, Shaik M Zakeeruddin, and Michael Gratzel. Charge collection and pore filling in solid-state dye-sensitized solar cells. *Nanotechnology*, 19(42):424003–, 2008. 148

[18] Juan Bisquert and Vyacheslav S. Vikhrenko. Interpretation of the time constants measured by kinetic techniques in nanostructured semiconductor electrodes and dye-sensitized solar cells. *The Journal of Physical Chemistry B*, 108(7):2313–2322, 2004. 148

[19] Laurence Peter. Sticky transport and interfacial transfer of electrons in the dye-sensitized solar cell. *Acc. Chem. Res.*, 42(11):1839–1847, July 2009. 148

[20] G. Lu, A. Linsebigler, and J. T. Yates. Ti3+ defect sites on TiO2(110): Production and chemical detection of active sites. *J. Phys. Chem.*, 98(45):11733–11738, November 1994. 148

[21] A. Janotti, J. B. Varley, P. Rinke, N. Umezawa, G. Kresse, and C. G. Van de Walle. Hybrid functional studies of the oxygen vacancy in TiO2. *Phys. Rev. B*, 81(8):085212–, February 2010. 148

[22] P. Knauth and H. L. Tuller. Electrical and defect thermodynamic properties of nanocrystalline titanium dioxide. *J. Appl. Phys.*, 85(2):897–902, January 1999. 148

[23] Aravind Kumar Chandiran, Frederic Sauvage, Montse Casas-Cabanas, Pascal Comte, S. M. Zakeeruddin, and Michael Graetzel. Doping a TiO2 photoanode with Nb5+ to enhance transparency and charge collection efficiency in dye-sensitized solar cells. *J. Phys. Chem. C*, 114(37):15849–15856, August 2010. 148

[24] S. Nakade, M. Matsuda, S. Kambe, Y. Saito, T. Kitamura, T. Sakata, Y. Wada, H. Mori, and S. Yanagida. Dependence of TiO2 nanoparticle preparation methods and annealing temperature on the efficiency of dye-sensitized solar cells. *J. Phys. Chem. B*, 106(39):10004–10010, September 2002. 149

[25] Stefan Guldin, Pablo Docampo, Morgan Stefik, Gen Kamita, Ulrich Wiesner, Henry J. Snaith, and Ullrich Steiner. Layer-by-layer formation of block-copolymer-derived TiO2 for solid-state dye-sensitized solar cells. *Small*, 8(3):432–440, 2012. 149

[26] I.O. Mazali, A.G. Filho, B.C. Viana, J. Filho, and O.L. Alves. Size-controllable synthesis of nanosized-TiO2 anatase using porous vycor glass as template. *Journal of Nanoparticle Research*, 8(1):141–148, 2006-02-01. 149

[27] Mou Pal, J. Garca Serrano, P. Santiago, and U. Pal. Size-controlled synthesis of spherical TiO2 nanoparticles: Morphology, crystallization, and phase transition. *J. Phys. Chem. C*, 111(1):96–102, December 2006. 149

[28] Xujie Lu, Xinliang Mou, Jianjun Wu, Dingwen Zhang, Linlin Zhang, Fuqiang Huang, Fangfang Xu, and Sumei Huang. Improved-performance

dye-sensitized solar cells using Nb-Doped TiO2 electrodes: Efficient electron injection and transfer. *Advanced Functional Materials*, 20(3):509–515, 2010. 153

[29] H.J. Snaith and L. Schmidt-Mende. Advances in liquid-electrolyte and solid-state dye-sensitized solar cells. *Advanced Materials*, 19(20):3187–3200, 2007. 153

[30] Tomas Leijtens, Jongchul Lim, Jol Teuscher, Taiho Park, and Henry J. Snaith. Charge density dependent mobility of organic hole-transporters and mesoporous TiO2 determined by transient mobility spectroscopy: Implications to dye-sensitized and organic solar cells. *Advanced Materials*, 25(23):3227–3233, 2013. 154

[31] H. J. Snaith and M. Grätzel. Enhanced charge mobility in a molecular hole transporter via addition of redox inactive ionic dopant: Implication to dye-sensitized solar cells. *Applied Physics Letters*, 89(26):262114, December 2006. 156

[32] Michael Gratzel. Solar energy conversion by dye-sensitized photovoltaic cells. *Inorganic Chemistry*, 44(20):6841–6851, 2005. PMID: 16180840. 156

[33] Tomas Leijtens and Henry Snaith. Oxygen vacancy induced doping of TiO2. Submitted, 2013. 156

Chapter 7

Conclusion

Recall the three aims we originally enumerated as the goals of this thesis:

1. Generalize existing computational models of charge transport to allow straightforward correlation of empirical data with simulation and account for non-diffusive processes

2. Critically assess and improve the accuracy of measurements of the collection efficiency, the bottom line metric for investigations of charge transport.

3. Synthesize and characterize novel mesostructures for enhanced charge transport in the SDSC

We stress that these aims were not invented as a post hoc summary of the work presented here. Rather, they represent an ambitious set of goals which require a variety of approaches, from computation to synthesis. Therefore, this thesis does not purport to have fully accomplished all three objectives, and we now assess our progress and make recommendations for future work.

7.1 Aim 1: Model Generalization

We made progress toward this aim by nondimensionalizing existing models to enable simple fitting of real device parameters; furthermore, we introduced a novel three-dimensional model of a nanowire that incorporated drift and diffusion.

In Chapter 3, we introduced the prevailing contemporary dye sensitized solar cell (DSSC) modelling literature, moving past early approximations like linear recombination and a constant diffusion length. We proceeded to nondimensionalize this updated governing equation, yielding an expression based on intrinsically important properties to the solar cell like the (intensity dependent) diffusion length. We proceeded to derive useful analytical expressions to describe the solar cell at steady state despite using and then discarding simplistic assumptions.

We turned next in Chapter 4 to transient decays and applied the nondimensional framework and the methodology of using simplifications to derive analytical expressions which, upon eliminating the assumptions, still held explanatory power. Our analytical treatment of small perturbation transient photocurrent and photovoltage decay rates allowed fitting of nondimensional device parameters from these measurements, like the recombination exponent and the relationship between trapped and free charge. Indeed, while our nondimensional governing equation could not reconstruct the unit-dependent JV curve of a solar cell, we could simulate the shape of the charge density profile and calculate the unitless collection efficiency of real devices. Importantly, this fitting protocol did not require extensive knowledge of device material parameters, so it offered a quick way to iteratively investigate real devices through nondimensional simulation.

Later, in Chapter 5, we introduced a brand new model of a nanowire based DSSC to simulate the flexible SnO_2 solid-state DSSCs (SDSCs) fabricated in that Chapter. The inspiration behind the three-dimensional, finite element model was that the nanowires exhibited rapid transport and an energetic density of states that resembled that of a single crystal rather than the defective exponential shape observed in nanocrystalline TiO_2. Therefore, we could relax the complicated multiple trapping modelling requirements (nonlinear recombination, dynamic equilibrium between trapped and free charge) and replace that complexity with terms accounting for electric fields and drift in the solar cell. This model reproduced rectifying behavior and, with reasonable choice of material parameters, neatly reproduced the behavior of the physical devices we fabricated. We went further, conducting a theoretical study of whether to illuminate such devices from the top or bottom and using simulation results to determine that the former was advantageous for device performance.

Thus, our efforts to generalize existing models of the DSSC took off in two different directions—one branch aimed for experimental usefulness and the other at increased precision by including previously neglected phenomena. Our unitless one-dimensional model enabled rapid correlation with experimental results; our three-dimensional nanowire model incorporated drift dependence often ignored in the literature, which, we argue, is not necessarily valid for hole transporting materials in SDSCs that do not effectively screen charge. However, it fell outside the scope of this thesis to unify the two approaches. The drift-dependent model relied on the simplified charge transport environment of the nanowire and did not exhibit the nondimensional simplicity and practical usefulness of our unitless one-dimensional model. This is clearly an area where progress can be and needs to be made. A path toward such a unification is much more readily apparent if SDSC development begins to rely on highly crystalline materials, like the ones we examine in Chapters 5 and 6; in that contingency, charge transport might be sufficiently simplified that a single, drift-dependent model could also be designed in a way that makes experimental iteration straightforward.

7.2 Aim 2: Critique of η_c

We dealt with this aim exclusively in Chapter 4, utilizing the modeling advances described above to identify serious inaccuracies in conventional measurement of the charge collection efficiency (η_c) of devices with low diffusion lengths.

The widespread use of convenient calculation of η_c from transient decay rates at short circuit led us to question whether this protocol was in fact an oversimplification. First, we introduced a method for simulating transient decay rates—either under the assumption of sufficiently small perturbation size or in general. This allowed us to first identify practical inaccuracies in the conventional measurement because the photovoltage decay rate varies dramatically with all but the smallest perturbation sizes. Then, taking care to minimize the perturbation size, we uncovered inherent problems with the simple collection efficiency calculation, demonstrating that transient equilibration between free and trapped charge biased the measurement of a steady-state property. We concluded that the conventional calculation is only accurate for values of η_c >90%. By employing the

device fitting protocol described in the last section, we used our novel nondimensional simulation framework to quantify the inaccuracies in measuring the collection efficiency of various real devices which had particular shell treatments, additive concentrations, and capping layer thicknesses.

While we succeeded in criticizing the conventional measurement of the collection efficiency, we made less progress toward solving the second problem—how to make it better. We did refine the measurement methodology by pointing researchers to steady state external quantum efficiency measurements of the collection efficiency under conditions when transient decays would yield an inaccurate measurement. Additionally, we claim that by using our simulation methodology and parameter fitting, one can still use transient decays and eliminate the equilibration bias effect. However, we were unsuccessful in identifying a single correction factor for transient perturbation measurements because the relationship between free and trapped charge is different for every cell architecture and choice of materials. Therefore, the outlook for a measurement of collection efficiency as convenient as the one previously used is not bright because of the inaccuracies we have demonstrated.

7.3 Aim 3: Novel Mesostructures

In Chapters 5 and 6, our most visually stimulating Chapters, we synthesized and characterized a variety of mesostructures which promised higher mobility. We arrived at several promising results which can lead to tremendous progress in future work.

We concerned ourselves with different, higher mobility replacement materials for the TiO_2 electron conductor and Spiro-OMeTAD hole conductor in Chapter 5. While we succeeded in fabricating the first viable SnO_2/P3HT SDSC, the nanocrystalline SnO_2 remained hostage to the multiple trapping framework, negating any potential mobility gains. Therefore, we fabricated the highest efficiency vertically aligned SnO_2 nanowire solar cell (which also happened to be flexible), taking advantage of a single crystal nanostructure to enhance electron mobility. However, we noted that these devices appeared limited by the hole transporting capabilities of Spiro-OMeTAD. Subsequently, we tested this

hypothesis by fabricating nanowire devices using ZnO as the metal oxide, and we observed the same apparent hole transport limitation. We solidified this hypothesis through comparison of transport rates through a compact layer of ZnO, and we finally broke through the barrier by fabricating ZnO nanowire SDSCs with P3HT as the high mobility hole conductor. Unfortunately, those devices exhibited very low efficiencies, despite a tantalizingly fast transport rate that stretched our instrumentation to the limit.

Noting the tremendous optimization challenges from replacing TiO_2, despite the positive transport signs observed, we turned instead to reëngineering the TiO_2 structure in Chapter 6. The mesoporous single crystal (MSC) of anatase TiO_2, borne from seeded templating, combined high surface area with extended crystallinity, promising to solve the low dye adsorption and anemic currents that plagued the nanowire cells. Indeed, after some optimization, these cells achieved respectable efficiencies, and we turned our attention to their charge transport properties. It emerged that we could sinter MSCs prior to film deposition, allowing sintering temperatures up to 850°C without a phase change. These annealed crystals exhibited faster transport through higher background charge density, and we uncovered a likely mechanism in thermally activated oxygen vacancy doping.

Just like our pursuit of the first aim, our efforts toward the third aim shot off in two directions. Our use of higher mobility replacement materials demonstrated faster transport rates, but we did not succeed in the exhaustive optimization necessary to catch up with twenty years of TiO_2 DSSC development. The other branch, use of MSCs as the photoanode, led to exciting discoveries of tunability and the prospect of low temperature processability since the MSCs can be sintered in-template. Both branches are promising routes to faster charge transport and thus thicker, better-absorbing SDSCs, but will require further optimization to approach conventional device efficiency. Indeed, the future of the SDSC depends on surmounting the thickness limitation, because rival technologies, both inorganic and organic, threaten to appropriate all of the advantages once considered unique to the SDSC. We hope that the multi-pronged approach introduced in this thesis, keeping fundamental scientific and well as commercial processability concerns in mind, will contribute to keeping the SDSC at the forefront of emerging solar technologies.

Appendix A: List of Publications

Varun Sivaram, James Kirkpatrick, and Henry Snaith. Critique of Charge Collection Efficiencies Calculated Through Small Perturbation Measurements of Dye Sensitized Solar Cells. *Journal of Applied Physics*. 113(6):0637090637096, 2013.

Golnaz Sadoughi, **Varun Sivaram**, Robbert Gunning, Pablo Docampo, Ingmar Bruder, Neil Pschirer, Azam Irajizad, and Henry J. Snaith. Enhanced Electronic Contacts in SNO_2-dye-P3HT based Solid State Dye Sensitized Solar Cells. *Phys. Chem. Chem. Phys.*. 15:20752080, 2013.

Edward JW Crossland, Nakita Noel, **Varun Sivaram**, Tomas Leijtens, Jack Alexander-Webber, and Henry J Snaith. Mesoporous TiO_2 Single Cystals Delivering Enhanced Mobility and Optoelectronic Device Performance. *Nature*. 495(7440):215219, 2013.

Varun Sivaram, Edward J.W. Crossland, Nakita Noel, Tomas Leijtens, Jack Alexander-Webber, Pablo Docampo, and Henry J. Snaith. Investigating the Source of Doping in Annealed TiO2 Mesoporous Single Crystals for Use in Solid State Dye Sensitized Solar Cells. 2013. *Journal of Physical Chemistry C*, 2013. Accepted.

Pablo Docampo, Aruna Ivaturi, Robert Gunning, Sandra Diefenbach, James Kirkpatrick, Claudia M Palumbiny, **Varun Sivaram**, Hugh Geaney, Lukas Schmidt-Mende, Mark E Welland, and Henry J. Snaith. The influence of 1D, Meso-and

Crystal Structures on Charge Transport and Recombination in Solid-State Dye-Sensitized Solar Cells. *Journal of Materials Chemistry A*. 1(39):12088-12095, 2013.

Mayor Antonio R. Villaraigosa, **Varun Sivaram**, and Ron Nichols. Powering Los Angeles with Renewable Energy. *Nature Climate Change*. 3(9):771-775, 2013.

Appendix B: Derivation of Eigenfunctions for Linearized Small Perturbation Transient Decays

Equation 4.4 (reprinted below) expressed a linear partial differential equation for the additional charge density, $\bar{n}_1$, caused by a small perturbation to a DSSC under steady state bias illumination with constant charge density profile $\bar{n}_0$ (recall that we have made the simplifying assumption to only consider the average background charge density $\langle \bar{n}_0 \rangle$).

$$\frac{\partial \bar{n}_1}{\partial \bar{t}} \approx -b\bar{n}_0^{b-m\beta}\bar{n}_1 + \lambda^2 \bar{n}_0^{1-m\beta}\frac{\partial^2 \bar{n}_1}{\partial \bar{x}^2} \tag{4.4}$$

with boundary conditions:

$$\bar{n}_1|_{\bar{t}=0} = \bar{n}_{1,initial} \tag{7.1a}$$

$$\frac{\partial \bar{n}_1}{\partial \bar{x}}|_{\bar{x}=1} = 0 \tag{7.1b}$$

$$\frac{\partial \bar{n}_1}{\partial \bar{x}}|_{\bar{x}=0} = 0 \quad \text{OR} \tag{7.1c}$$

$$\bar{n}_1|_{\bar{x}=0} = 0 \tag{7.1d}$$

Equations 4.6 and 4.7 set out the ith eigenfunction for the solution to Equation 4.4 in the case of a current decay (corresponding to the boundary condition setting the charge density zero at the LHS). We proceed to derive this photocurrent decay solution below. First, we define some new constants for convenience:

$$A \equiv b\bar{n}_0^{b-m\beta} \tag{7.2}$$

$$B \equiv \lambda^2 \bar{n}_0^{1-m\beta} \tag{7.3}$$

This allows us to express Equation 4.4 as:

$$\frac{\partial \bar{n}_1}{\partial \bar{t}} = -A\bar{n}_1 + B\frac{\partial^2 \bar{n}_1}{\partial \bar{x}^2} \tag{7.4}$$

Separation of Variables

We first posit that the marginal charge density can be decomposed as the product of a space-varying and a time-varying function.

$$\bar{n}_1(x,t) = X(\bar{x})T(\bar{t}) \tag{7.5}$$

So, using primes to denote derivatives, we can express 4.4 as:

$$XT' = -AXT + BX''T \tag{7.6}$$

or,

$$\frac{1}{B}\frac{T'}{T} + \frac{A}{B} = \frac{X''}{X} = -\sigma \tag{7.7}$$

The rightmost equality above follows from the fact that a function of $\bar{x}$ is equal to a function of $\bar{t}$, which means both must be equal to the same constant, which we choose to be $-\sigma$.

We now find the solutions to both the space-dependent and time-dependent components of $\bar{n}_1$. Beginning with $X(\bar{x})$, we have $X'' + \sigma X = 0$, so we can write:

$$X(\bar{x}) = a_1 sin(\sqrt{\sigma}\bar{x}) + a_2 cos(\sqrt{\sigma}\bar{x}) \tag{7.8}$$

Applying the boundary condition that stipulates zero charge density at $\bar{x} = 0$, we can see that a_2 is 0. Then, by applying the boundary condition on the right boundary that $\frac{\partial \bar{n}_1}{\partial \bar{x}} = 0$, we can deduce that:

$$\sqrt{\sigma} = \frac{(2i+1)\pi}{2} \tag{7.9}$$

for integers i ascending from 0. Therefore, we find for the space dependent function:

$$X(\bar{x}) = a_1 sin\left(\frac{(2i+1)\pi}{2}\bar{x}\right) \tag{7.10}$$

We now proceed to investigate the form of the time-dependent function. We have:

$$\frac{1}{B}\frac{T'}{T} + \frac{A}{B} = -\sigma \tag{7.11}$$

So we can deduce that:

$$T(\bar{t}) = a_3 exp(-(A + B\sigma)\bar{t}) \tag{7.12}$$

Fourier Series

Now that we have successfully found a decomposition of $\bar{n}_1(x,t)$ that satisfies Equation 4.4 in the form of a weighted sine function, we can exploit the orthogonality of trigonometric functions and apply Fourier series analysis to construct a weighted sum of orthogonal eigenfunctions that sum to $\bar{n}_1$. Note that we no longer rely upon the initial assumption that $\bar{n}_1 = X(\bar{x})T(\bar{t})$.

Combining the constants a_1 and a_3 into a single constant upon forming the product XT, we can now write:

$$\bar{n}_1 = \sum_{i=0}^{\infty} c_i sin\left(\frac{(2i+1)\pi}{2}\bar{x}\right) exp(-\kappa_J^i \bar{t}) \tag{7.13}$$

where:

$$\bar{\kappa^J}_i = \langle \bar{n}_0 \rangle^{1-m\beta} \left(\lambda^2 (2i+1)^2 \frac{\pi^2}{4} + b \langle \bar{n}_0 \rangle^{b-1}\right) \tag{7.14}$$

and

$$c_i = \frac{\int_0^1 sin\left(\frac{(2i+1)\pi}{2}\bar{x}\right)\bar{n}_{1,initial}\mathrm{d}\bar{x}}{\int_0^1 \left[sin\left(\frac{(2i+1)\pi}{2}\bar{x}\right)\right]^2\mathrm{d}\bar{x}} \tag{7.15}$$

This last step is like projecting $\bar{n}_{1,initial}$ onto each orthogonal eigenfunction and then dividing by the norm.